PHYSICALLY-BASED MODELING OF RAINFALL-TRIGGERED
LANDSLIDES IN KAPTANPASA, RIZE

A THESIS SUBMITTED TO
THE GRADUATE SCHOOL OF NATURAL AND APPLIED SCIENCES
OF
MIDDLE EAST TECHNICAL UNIVERSITY

BY

MUHAMMET DURMAZ

IN PARTIAL FULFILLMENT OF THE REQUIREMENTS
FOR
THE DEGREE OF MASTER OF SCIENCE
IN
CIVIL ENGINEERING

FEBRUARY 2022

Approval of the thesis:

PHYSICALLY-BASED MODELING OF RAINFALL-TRIGGERED LANDSLIDES IN KAPTANPASA, RIZE

submitted by **MUHAMMET DURMAZ** in partial fulfillment of the requirements for the degree of **Master of Science** in **Civil Engineering, Middle East Technical University** by,

Prof. Dr. Halil Kalıpçılar

Dean, Graduate School of **Natural and Applied Sciences**

_____

Prof. Dr. Erdem Canbay

Head of the Department, **Civil Engineering**

_____

Assoc. Prof. Dr. Nejan Huvaj Sarıhan

Supervisor, **Civil Engineering, METU**

_____

Assoc. Prof. Dr. Marcel Hürlimann Ziegler

Co-Supervisor, **Civil and Environmental Engineering, UPC**

_____

Examining Committee Members:

Prof. Dr.Bahadır Sadık Bakır

Civil Engineering, METU

_____

Assoc. Prof. Dr. Nejan Huvaj Sarıhan

Civil Engineering, METU

_____

Assoc. Prof. Dr. Nabi Kartal Toker

Civil Engineering, METU

_____

Assoc. Prof. Dr. Tolga Görüm

Eurasia Institute of Earth Sciences, ITU

_____

Dr. Resul Çömert

Geomatic Engineering, Gumushane University

_____

Date: 28.02.2022

I hereby declare that all information in this document has been obtained and presented in accordance with academic rules and ethical conduct. I also declare that, as required by these rules and conduct, I have fully cited and referenced all material and results that are not original to this work.

Name Last name : Muhammet Durmaz

Signature :

ABSTRACT

PHYSICALLY-BASED MODELING OF RAINFALL-TRIGGERED LANDSLIDES IN KAPTANPASA, RIZE

Durmaz, Muhammet
Master of Science, Civil Engineering
Supervisor : Assoc. Prof. Nejan Huvaj Sarıhan
Co-Supervisor: Assoc. Prof. Marcel Hurlimann Ziegler

February 2022, 112 pages

Physically-based models are reliable tools for landslide susceptibility assessment. However, they are, based on various simplifications, affected by different factors, and applicable for particular landslides. Therefore, landslide inventories are recommended to be subdivided into subsets reflecting different controlling factors and failure mechanisms, and the analysis should reflect these differences. Many physically-based models are based on infinite slope assumptions. The applicability of this assumption is associated with having large and long dimensions compared to their depth. This study investigates morphometric features of more than 1000 individual landslides triggered by a rainfall event on Sept 27- Oct 4 in 2017 in Kaptanpaşa, Rize (Northern Turkey). The failures were classified according to their morphology, slope types, and whether the infinite slope assumption is valid or not. 45% of failures on hillslopes and 24.1% of failures in other slopes confirm the infinite slope assumption. Depth of landslide can be represented by Weibull distribution with a mean depth of 1.05 m. Two different hydrological (FSLAM, TRIGRS) and stability (infinite-slope, 3D slope stability via SCOOPS3D) methods are tested for physically-based modeling of these failures. Stability parameters (ϕ', c', z) and antecedent conditions were calibrated semi-automatically via a

MATLAB code. Then hydraulic parameters were calibrated iteratively. In the calibration, only failures confirming the models' assumptions were employed. The performance of FSLAM was evaluated as highest in terms of area under curve (AUC), indicating that the final pore pressure condition is close to saturation. SCOOPS3D estimated unstable areas less than infinite slope solution with higher ratio of True Positive Rate (TPR) / False Positive Rate (FPR) , confirming the other studies in the literature. Moreover, the performance of the stability assumption is shown to be dependent on the morphology of failures.

Keywords: Lanslide morphology, landslide susceptibility, TRIGRS, FSLAM, SCOOPS3D

ÖZ

RİZE KAPTANPAŞA'DA YAĞMURLA TETİKLENEN HEYELANLARIN FİZİKSEL BAZLI MODELLENMESİ

Durmaz, Muhammet
Yüksek Lisans, İnşaat Mühendisliği
Tez Yöneticisi: Doc. Dr. Nejan Huvaj Sarıhan
Ortak Tez Yöneticisi: Doç. Dr. Marcel Hürlimann Ziegler

Şubat 2022, 112 Sayfa

Fiziksel tabanlı modeller, heyelan duyarlılık değerlendirmesi için güvenilir araçlardır. Ancak, çeşitli basitleştirmelere dayanırlar, çeşitli faktörlerden etkilenirler ve belirli heyelanlar için geçerlidirler. Bu nedenle, heyelan envanterlerinin çeşitli kontrol faktörlerini ve yenilme mekanizmalarını yansıtan alt gruplara ayrılması tavsiye edilir ve analiz bu farklılıkları yansıtmalıdır. Birçok fiziksel tabanlı model, sonsuz şev varsayımına dayanmaktadır. Bu varsayımın uygulanabilirliği, derinliklerine kıyasla büyük ve uzun boyutlara sahip olmaları ile ilişkilidir. Bu çalışmada, 27 Eylül-4 Ekim 2017 tarihlerinde Rize, Kaptanpaşa'da (Kuzey Türkiye) yağışların tetiklediği 1000'den fazla heyelanın morfometrik özellikleri araştırılmıştır. Yenilmeler morfolojilerine, şev tiplerine ve sonsuz şev varsayımının uyup uymadığına göre sınıflandırılmıştır. Yamaçlardaki yenilmelerin %45'i ve diğer şevlerdeki yenilmelerin %24.1'i sonsuz şev varsayımına uygundur. Heyelanların derinliği, ortalama 1,05 m derinliğe sahip Weibull dağılımı ile temsil edilebilir. Bu heyelanların fiziksel tabanlı modellemesi için iki farklı hidrolojik (FSLAM, TRIGRS) ve stabilite varsayımı (sonsuz şev, SCOOPS3D ile 3-boyutlu kayma) test edilmiştir. Stabilite parametreleri ve öncül hidrolik koşullar, bir MATLAB kodu

aracılığıyla yarı otomatik olarak kalibre edilmiştir. Daha sonra hidrolik parametreler iteratif olarak kalibre edilmiştir. Kalibrasyonda sadece modellerin varsayımlarına uygun heyelanlar kullanılmıştır. FSLAM'ın performansı, son boşluk basıncı koşulunun doygunluğa yakın olduğunu göstererek, eğri altındaki alan (AUC) açısından en yüksek olarak değerlendirilmiştir. SCOOPS3D, literatürdeki diğer çalışmaları doğrulayarak, daha yüksek Doğru Tahmin Oranı (TPR) / Yanlış Tahmin Oranı (FPR) değeri ile sonsuz eğim çözümünden daha az duraysız alan tahmin etmiştir. Ayrıca, stabilite varsayımının performansının, yenilmelerin morfolojisine bağlı olduğu gösterilmiştir.

Anahtar Kelimeler: Heyelan morfolojisi, heyelan duyarlılık analizi, FSLAM, SCOOPS3D, TRIGRS.

ACKNOWLEDGMENTS

I appreciate Olgu Orakçı and Anıl Ekici for their sincere friendship during our joint works and later. Furthermore, I would like to thank all my other friends from METU geotechnical department, especially Elife Çakır, Satuk Buğrahan Sarı, Berkan Söylemez, Emre Duman, Yunus Emre Sarıçiçek, Mehmet Türkezer, and Melih Kenanoğlu.

I would like to thank my sisters and brothers Safigül, Lale, Hatice, Suat and my parents who have always supported me.

Special thanks to Gizem Kars for being with me so far. She is the first person I consulted when I was in doubt, and I shared when I was happy.

I want to thank Burtay Ekinci, Ekinsu Özmen, Cem Kaya, Aybüke Gülkaya, Koray Beyaz, Batuhan Çavuş, Gamze Ağaçayak, Tankut Serttaş, Hadi Iskit, Arda Araz, Ilknur Özcan, and all my other friends.

TABLE OF CONTENTS

LIST OF TABLES

TABLES

LIST OF FIGURES

FIGURES

LIST OF SYMBOLS

H_s **(m)** Scarp height of landslide

W (m) Landslide width

L_s **(m)** Horizontal length of landslides' scarp

t (m) Slope normal thicknes of landslide

θ (degree) Slope angle

L_H **(m)** Horizontal length of landslide

H (m) Slope height

L (m) Slope-parallel length of landslide

Ψ (m) Suction head

α (1/m) Exponent of Gardners (1958) SWRC equation

Θ Volumetric water content

$Θ_r$ Residual volumetric water content

$Θ_s$ Saturated volumetric water content

K_s **(m/s)** Saturated hydraulic conductivity

D_0 **(m/s)** Hydraulic diffusivity in saturated condition

$D_Ψ$ **(m/s)** Hydraulic diffusivity of soil in restpective suction

I_{zlt} Steady-state background infiltration

q_a Antecedent recharge

b Cell size of digital elevation model (DEM)

q_e Infiltrated amount of water during rainfall

n Soil porosity

CN Curve number

$ρ_s$ Bulk density of the soil

Z Depth of soil in vertical direction

$ρ_w$ Density of water

h_a Rise of water table during rainfall

h_e Rise of water table in antecedent condition

c_s	Cohesion of the soil
c_r	Cohesion provided by plant roots
D_{max}	Maximum depth of landslides in vertical direction
D_{mean}	Mean depth of landslides in vertical direction
d_{wi}	Initial depth of water table
$\emptyset'$	Effective internal friction angle
γ_s	Bulk unit weigth of soil
P_e	Total amount of event rainfall

CHAPTER 1

INTRODUCTION

Landslides are one of the most hazardous natural phenomena, causing loss of lives and properties worldwide (Hong et al., 2007). Different studies demonstrate the severe consequences of landslides across the globe and in Turkey (e.g. Filiz et al., 2011; Görüm & Fidan, 2021; Hong et al., 2007). In the USA, landslides cause 2 billion dollars of damage and the death of 25-50 people annually (Hong et al., 2007). A recent study conducted by Görüm and Fidan (2021) reports that 1343 fatal landslides between 1929-2009 caused 389 deaths in Turkey, and 55% of these landslides occurred in the Northern part of the country, known as the Black Sea region.

Rize province is the province most affected by landslides in Tukey, in which landslides occupy 89 % of the disasters that occur in the region (Filiz et al., 2011). Reis et al. (2008) highlighted that rainfall is the triggering factor in 99% of the landslides between 1964 and 2008 in Rize. Rize is the city with the highest average annual rainfall in Turkey (2299 mm based on data from 1928 to 2017, (Uyeturk et al., 2020), which is about 4 times the average annual rainfall in Turkey). Significant rain, mountainous topography, weathered volcanic materials, and land-use alterations over the years from forest to tea-plantation are other predisposing factors in the development of large numbers of landslides in Rize every year.

Physically-based landslides susceptibility models are reliable tools for preventing devastating consequences of landslides providing future estimations (Corominas et al., 2014; Fell et al., 2008). They can be utilized for both land-use planning and early warning system. However, their accuracy depends on detailed soil geotechnical properties, hydrological conditions, and topography. Besides, each physically-based method has different simplifying assumptions. Therefore, it is essential to collect as much data as possible to improve the accuracy assessment of these models.

Furthermore, the back-analysis of multiple models make it possible to determine the most suitable model for a specific area and calibrate the model.

1.1   Problem Statement

Physically-based landslide susceptibility models have different assumptions for hydrological and slope stability calculations. Hydrological assumptions are grouped based on the main triggering mechanisms such as lateral flows (Montgomery & Dietrich, 1994; Pack et al., 1998)), vertical infiltration dealing with saturated (Baum et al., 2002; Iverson, 2000) and unsaturated (Baum, Savage, et al., 2008) conditions or both (Medina et al., 2021; Montrasio and Valentino 2008). Also, these models are differentiated between those that deal with the time variation of stability (An et al., 2016; Baum et al., 2008; Lanni et al., 2012) or those that use simplified approaches (Medina et al., 2021; Montrasio & Valentino, 2008). Stability assumptions are based on failure surface geometry. The infinite slope assumption is the most widely used; 3D stability methods are also adopted (Brien & Reid, 2007; Mergili et al., 2014; Oguz et al., 2021).

The performance of the adopted method depends on the accuracy of several parameters such as geotechnical parameters, soil depth, cell size in which computations are carried out, etc. Due to the multitude of influential factors, calibration of the input parameters is inevitable. Landslide inventories are utilized to calibrate susceptibility models. Therefore, the validity of the assumptions made by the model is essential to accomplish accurate results. Accordingly, detailed exploitation of landslide inventories is crucial. Although the morphometric characteristics of the landslides are indicated as a metric in selecting the suitable stability method (Hutchinson, 1994; Milledge et al., 2012; Tiwari et al., 2014), they are generally ignored in the literature.

Secondly, to decide which model is more favorable for a specific area, two essential factors should be considered, which are (i) accuracy of the prediction capability of the model with available data (ii) computational cost of the model. Comparing

different hydrological and stability models in the back-analysis of events is an efficient way of making this decision.

1.2 Research Objective

From the perspective explained in the previous section, the primary purposes of this study are as follows.

- This study aims to document morphometric characteristics of shallow landslides triggered by a rainfall event (that occurred between September 27-October 4 in 2017) in Kaptanpaşa, Rize. The prominence of these characteristics to improve the performance of physically-based susceptibility models is discussed.
- This study proposes a morphology-based classification of landslides to compromise the stability assumption of the available model.
- Three different susceptibility models (FSLAM, TRIGRS, SCOOPS3D) are compared. These models have different hydrological and stability assumptions with varying computational requirements. Performance discussions of all models are made by considering both accuracy and computational cost.
- The effect of landslide morphology on the performance of physical-based models is shown.
- A new time-saving and straightforward calibration method of physically-based models is introduced for data-scarce environments.

1.3 Thesis Structure

The thesis continues with a literature review in chapter 2. The literature review consists of (i) summarizing landslide classification systems (ii) defining morphometric features of landslides, (iii) summarizing the relation between landslides' morphology and stability assumptions, (iv) explaining the methods for

obtaining morphological features of landslides (v) summarizing available physically-based methods in the literature and discussing influential factors in physically-based models, (vii) and reviewing the other studies related with this study.

Chapter 3 introduces the study area, a summary of available data, methods used for obtaining morphometric features, and physically-based back analysis.

In chapter 4, results are presented, and relevant discussions are made.

In chapter 5, the primary outcomes of this study are summarized, and recommendations for future studies are given.

CHAPTER 2

LITERATURE REVIEW

2.1   Landslide classification system and morphometric features of landslides

The landslide classification system is mainly followed in the literature based on the proposals of   Varnes (1958, 1978), Hutchinson (1988), and Cruden & Varnes (1996). Recently, Hungr et al. (2014) updated this classification system (Table 2.1). The classification considers the type and rate of the movement, geotechnical and geological properties of the sliding material, state of activity, and water content.

The types of movement of slides are assorted considering the dimensions of landslides. Skempton & Hutchinson (1969) reported that landslides' thickness to length ratio is lower than 0.1 for translational, and between 0.15 to 0.33 for rotational failures. Intermediate values are associated with compound slides. A significant internal disturbance is observed in flow failures (Cruden and Varnes, 1996). However, understanding which type of movement governs the failure (boundary slide or inner distortion) is always challenging (Hungr et al., 2001).

In addition to the classification system proposed by Cruden & Varnes (1996), landslides are categorized as deep-seated and shallow. The reason for making this distinction is that deep-seated and shallow landslides are different in terms of the damages they may cause, the stabilization measures required, their geometry, volume, and frequency (Baum et al., 2008). Shallow landslides are often associated with a triggering event, and their failure planes are generally more affected by seasonal changes and contain non-soil components such as tree roots. On the other hand, deep landslides are often triggered by a combination of multiple factors, there is greater uncertainty about their depth, and they require more geotechnical investigations (Baum al., 2008). Generally, 5 m depth is considered as a boundary between deep-seated and shallow landslides (Burns & Mickelson, 2016).

Table 2.1 Updated version of Varnes landslide classification system (Hungr et al., 2014).

Types of Movement	Rock	Soil
Fall	Rock/ice Fall	Bouldar/debris/silt fall
Topple	Rock block topple Rock Flexural topple	Gravel/sand/silt topple
Slide	Rock rotational slide Rock planar slide Rock wedge slide Rock compound slide Rockk irregular slide	Clay/silt rotational slide Clay/silt planar slide Gravelsand debris slide Claysilt compound slide
Flow	Rock/ice avalanche	Sand/silt/debris dry flow Sand/siltdebris flowslide Sensitive clay flowslide Debris flow Mud flow Debris flood Debris avalanche Earth flow Peat flow
Slope deformation	Mountain slope deformation Rock slope deformation	Soil slope deformation Soil creep Soilfluction

There is a close relationship between stability modeling and the morphology of landslides. Limit equilibrium analyses based on the assumption of the infinite slope are commonly used for shallow landslides. Landslides that are not suitable for modeling in this way should be modeled in 2D or 3D. Although it is generally thought that the infinite slope assumption underestimates the stability, it can give unconservative results because it neglects the interaction between the soil columns (Mergili et al., 2014).

The prerequisite for modeling landslides with infinite slope is that the side boundary effects in the transverse directions to the slip are negligible; that is, they can be modeled in 2D (Gens et al., 1988; Griffiths & Marquez, 2007; Hutchinson, 1994; Wei et al., 2009; Zhang et al., 2011). Lateral boundary effects decrease in landslides that are wider compared to their depths (Figure 2.2). These effects also depend on the soil's cohesion, lateral earth pressure, failure condition (drained, undrained), and pore pressure state (Bellugi et al., 2021; Hutchinson, 1994). Hutchinson (1994) compared 2D and 3D factors of safety of the sliding mass based on rectilinear sliding block analyses and proposed charts for critical depth to width ratio in 2D solutions (so that the error remains under 10 percent) and recommended to use 3D models if the depth to width ratio exceeds the critical value from the chart.
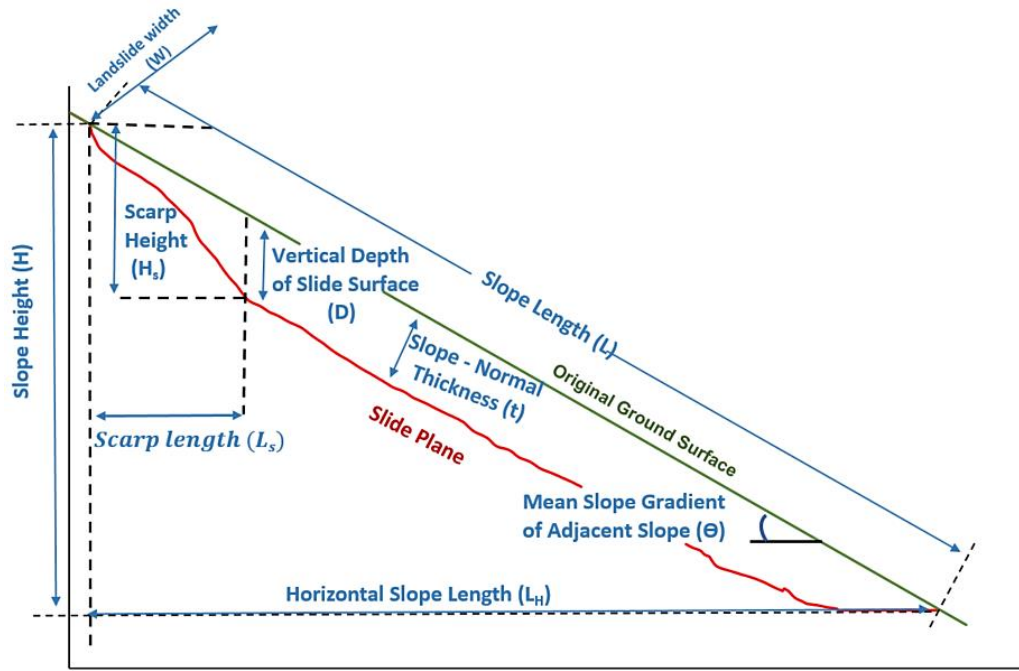
Figure 2.1. Geometric features of landslides adopted in this study.

Validity of infinite slope assumption needs high "length to depth ratio". Several attempts have been made to determine a critical value. Griffiths et al. (2011) compared finite element and limit equilibrium solutions for an infinite slope, concluding that both solutions of the infinite slope's stability are in good agreement. They reported that the L_H/D ratio of landslides should be higher than 16 to use the infinite slope assumption, where L_H presents horizontal length and D is depth of sliding surface (Figure 2.1). Using the finite element method, Milledge et al. (2012) highlighted that the soil's cohesion affects the error resulting from the infinite-slope assumption. A higher L_H/D ratio is required to minimize the error with increasing cohesion. After a threshold L_H/D ratio of 25, the error is expected to be less than 5 percent regardless of the cohesion. Tiwari et al. (2014) reported 20 as the critical "length to depth ratio" using the spectral element method.

2.2   Mechanisms of rainfall-triggered shallow landslides

Different proposals and observations exist in the literature to explain the triggering of landslides by rainfall. These proposals mainly focus on two different movements of the water in the soil: lateral and vertical (Lu & Godt, 2011). During rainfall's vertical infiltration, the soil suction decreases with advancing wetting front. Depending on the shear strength of the soil and the slope geometry, failure may occur in the negative pore pressure stage (Chae et al., 2015; Lu & Godt, 2011). When the wetting front encounters a less permeable layer, positive pore pressure is generated (Lu & Godt, 2011; Simoni et al., 2008). These failures are observed in steep slopes with small internal friction angles and cohesion. The less permeable layers might be bedrock or a more consolidated layer (Corominas et al., 2014; Lu & Godt, 2011).

The advancement of the wetting front depends on the soil's pore pressure distribution, rainfall pattern, and hydraulic conductivity (Lu & Godt, 2011). If the pore pressure distribution is uniform and rainfall intensity is high, the wetting front advancement from top to bottom is observed. On the other hand, if the soil's permeability is high compared with the rainfall intensity, positive pore pressure rise takes place at the bottom of more permeable layers (Montrasio & Valentino, 2008). Macro pores and preferential flow paths originating from the seasonal volumetric changes of the soil and plant roots can accelerate the soil's response to rain (Shao et al., 2015). Bordoni et al. (2021) observed that pore pressure response of soil is "rising water table from bottom of the top layer", not "advancing wetting front from top to bottom", due to macropores and stress cracks in the natural slope that they followed for seven years (Bordoni et al., 2021). Springman et al. (2013) reported that these behaviors could vary with the season.

When the accumulated water on the less permeable layer in the soil becomes connected, they form the perched water table and start to flow laterally (Lanni et al., 2012). If the macro-pores in the soil are connected, this lateral flow might be rapid during the rainfall, which is called stormflow (Lu & Godt, 2011). This case causes a rapid rise of the perched water table at the topographic convergence points

(Montgomery & Dietrich, 1994). It is expected that the landslides triggered in this way will be more at the topographic convergence points (close to the streams).

Figure 2.1 shows the stratification of natural slopes and possible movements of water during rainfall. The layer at the very top is very loose, consists of organic materials and debris and its depth varies according to climate and vegetation (Dennis et al., 2011). Layer A consists of a mixture of decayed organic and inorganic materials (Dennis et al., 2011). In the B layer, on the other hand, it is expected that the percentage of inorganic matter will be higher, but it does not show the characteristics of the parent rock that it is originated from (Lu & Godt, 2011). This layer can vary from a few centimeters to several meters and contains cracks and hollows with dramatically different hydraulic conductivity to the soil matrix (Lu & Godt, 2011).

On the other hand, the C layer shows the characteristics of the bedrock depending on the weathering level (Lu & Godt, 2011). The perched water table may form on the bedrock surface or between different layers during heavy rainfall (Lu & Godt, 2011). It is also possible to see a capillary barrier effect if the underlying layer has coarser particle size distribution (Lu & Godt, 2011).

When the landslides in Rize are observed, the hydraulic conductivity difference between the layers seems to cause these failures. When the organic and mineral contents of the samples collected from the failure surfaces are examined, it is thought that these landslides occurred in the B horizon (Uyetürk, 2019).

In which layer the landslide will occur may vary depending on the hydraulic properties of these layers and the rainfall pattern (Tsai & Chiang, 2013). For this reason, the most accurate modeling is modeling layered systems by determining the hydraulic and strength properties of these layers (Li et al., 2021; Lizárraga et al., 2017; Lizárraga & Buscarnera, 2019; Tsai & Chiang, 2013). However, the average hydraulic conductivity is also employed as a simplified approach, taking into account the layer where the landslide is located (Sorbino et al., 2010).

Horizon	$K_{s\text{-}matrix}$	$K_{s\text{-}fracture}$	$U_{w\text{-}entry}$
Organic	$1(10^{-3}$ m/s)	10	1 (kPa)
A	0.1	0.1	5
B	0.05	0.1	10
C	0.01	0.1	50
Bedrock	0.001	0.1	100

Depth (cm): 0, 5, 15, 50, 100
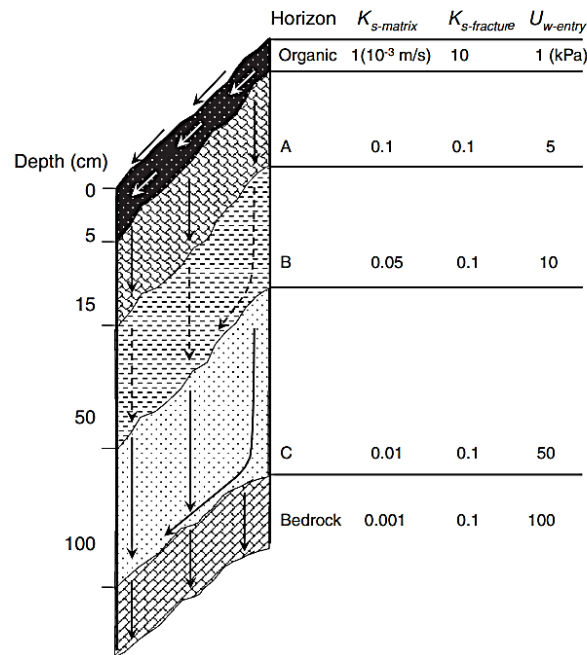
Figure 2.2. Stratification of natural hillslopes and possible movement of water during rainfall (Lu & Godt, 2011).

If the water moving laterally between layers with different permeability, or in cracks in the bedrock face, encounters an obstacle, it moves upwards, called bedrock exfiltration (Lu & Godt, 2011). In this case, the resulting pore water pressure is higher than the hydrostatic pressure and may trigger a landslide (Sitarenios et al., 2021). In general, such failures are local and need to be modeled in a site-specific manner (Cascini et al., 2011; Sitarenios et al., 2021).

In general, flow failures are associated with positive pore water pressure in the soil. The volumetric change of the soil can also cause this positive pore water pressure during rainfall, which can be formed by the aforementioned mechanisms (Song et al., 2020).

All of the above mechanisms can be seen in one area during a rainfall event. In addition to these mechanisms, sudden changes in the topography and anthropogenic factors also cause the emergence of different failure mechanisms (Cascini et al., 2008). Therefore, it is challenging to successfully model all failure types in the area with a single model (Sorbino et al., 2010).

2.3   Landslide Inventories

Landslide inventories show the location, classification, activity status, volume, date of occurrence, and other characteristic features of landslides (Fell et al., 2008). Landslide inventories are a crucial part of landslide studies because the primary assumption of susceptibility studies is that conditions that caused landslides in the inventory will also trigger landslides in the same region in the future (Corominas et al., 2014).

Inventories are used in physically-based landslide susceptibility studies to compare model results and previous landslides. In this way, the model's performance can be evaluated, and model parameters can be calibrated (Corominas et al., 2014; Medina et al., 2021). In addition, information on the size and depth of landslides provides important information in the calibration of models (Lizárraga & Buscarnera, 2019; Mergili et al., 2014).

Conventional landslide inventory compiling methods include collecting historical information, mapping landslides by field survey, and visual interpretation of aerial images. Furthermore, high spatial resolution satellites, synthetic aperture radar (SAR), light detection and ranging (LIDAR), and unmanned aerial vehicles (UAV) are recently adopted as data-providing platforms for landslide mapping (Gorum, 2019; Guzzetti et al., 2012).

High-resolution digital elevation models (DEM) can be employed to get morphometric properties of failures. By comparing DEMs from before and after a landslide episode, the 3D geometry of the failure zone can be acquired. Although this method is reasonably practical, it suffers from the low temporal frequency of available data (Zieher et al., 2016). Due to the time interval between successive data collections, linking all failures to a single rainfall event is not possible (Zieher et al., 2016). Furthermore, owing to climatic and human influences, distinguishable characteristics of tiny landslides may change or vanish over time, and transported debris (or plants) may cover landslide scars (Zieher et al., 2016).

A single DEM acquired after the landslides can also be used as an alternative. This approach is free of time-related mistakes, although it necessitates procedures for precisely evaluating landslide geometric characteristics. There are protocols to follow in the literature for this aim (Burns and Madin 2009; Slaughter et al. 2017).

2.4   Physically-based susceptibility models for rainfall-induced landslides

Different physically-based models have been proposed considering the failure mechanisms described in Chapter 2. Since it is impossible to solve all failure mechanisms in a single model, each model has its simplifications and hydrological assumptions. The proposed models differ in terms of the triggering movement of water in the soil (lateral, vertical) and calculation methods, the method of coping with geotechnical uncertainties, the stability calculation method they use, and whether they take into account the volume change.

The lateral flow of water is considered in two states: transient and steady-state (Lanni et al., 2012; Montgomery & Dietrich, 1994). The steady-state approach is a simplification of a time-dependent process. This approach represents storm flow during rain or the antecedent hydrological state of the ground before precipitation that triggers a landslide. The proposed models for vertical flow (infiltration) differ in that they solve transient infiltration (Richards equation) or use simplified methods.

As for the soil's shear strength, some models consider the contribution of soil suction to stability in the unsaturated stage.

Additionally, models that consider the ground's uncertainty and make deterministic analyses are also distinguished from each other.

Table 2.2 Physically-based models in literature and their assumptions.

	Infiltration	Lateral Flow	Unsaturated Shear Strength	Stability Assumption	Material Uncertainity	Reference
TRIGRS	Saturated-Unsaturated / Transient		Included	Infinite Slope	Available inTRIGRS-P	(Baum, et al., 2008)
SINMAP		Setady-state	Not included	Infinite Slope	Available	(Pack et al., 1998)
SHALSTAB		Setady-state	Not included	Infinite Slope		(Montgomery & Dietrich, 1994)
GeoTop-FS	Saturated-Unsaturated / Transient	Transient	Included	Infinite slope	Available	(Simoni et al., 2008)
Clinus	Saturated-Unsaturated / Transient		Included	Infinite slope		(Song et al., 2021)
SLIP	Unsaturated / Transient	Transient	Included	Infinite slope		(Montrasio & Valentino, 2008)
TiVass	Saturated-Unsaturated / Transient	Transient	Included	Infinite Slope		(An et al., 2016)
HIRESS	Saturated-Unsaturated / Transient	Transient	Included	Infinite Slope	Available	(Rossi et al., 2013)
SHIA_Landslide		Transient	Not included	Infinite Slope		(Aristizábal et al., 2016)
STEP-TRAMM	Unsaturated-Saturated Transient	Transient	Included	Hexagonal bundle soil columns		(Lehmann & Or, 2012)
CI-SLAM		Transient	Included	Infinite slope		(Lanni et al., 2012)
FSLAM	Asymtotic	Steady-state	Not included	Infinite slope	Available	(Medina et al., 2021)
R.ROTSTAB			Included	Elipsoidal		(M. Mergili et al., 2014)
SCOOPS 3D			Included	Spherical		(Reid et al., 2015)

The selected models are shown in Table 2.2. Only the main assumptions are indicated in the table. The models differ from each other, with some features not mentioned in the table. For example, the cLinus is distinguished by analyzing stratified slopes and volume change during rainfall. Detailed information about the models can be obtained from the references given.

14

In Rize province, landslide susceptibility studies are mostly performed by data-driven methods (Nefeslioglu et al., 2011; Yalcin & Bulut, 2007). Recently, SINMAP is adopted by Keles & Nefeslioglu (2021) to investigate landslide susceptible areas in the Güneysu catchment area.

In this study, TRIGRS, FSLAM, and SCOOPS3D are selected to compare performance of different hydrological and stability assumption considering available data and time.

2.4.1   Inputs and Effective Parameters

In the following sections, the common input parameters that are needed in a physically-based landslide susceptibility study will be discussed. The factors considered are rainfall, geotechnical parameters, soil thickness, vegetation and digital elevation model.

2.4.1.1   Rainfall

In the landslide literature, rainfalls are discussed in two aspects: the event rainfall that triggers the landslide and the antecedent rainfall that affects the pore water pressure before the event rainfall. Generally, landslides are triggered by heavy rainfall (Lu & Godt, 2011; Rahardjo et al., 2001; Reis et al., 2008). Therefore, event rainfall represents the rain in the time interval when the precipitation is intense. Antecedent rainfall determines the ground response during rainfall by influencing the groundwater table and affecting the vertical pore pressure distribution in the soil (Baum et al., 2010; Iverson, 2000; Medina et al., 2021; Napolitano et al., 2016). While the effect of the vertical movement of the rainwater occurs in a shorter time, the impact of the lateral movement emerges in a long time (Baum et al., 2008). Therefore, according to the selected hydrological model, the time interval to be chosen for the event precipitation and the antecedent precipitation should be compatible with the model's assumption. For example, in models that perform analysis based on 1D infiltration, the event precipitation should include short periods

in which lateral movement will not be dominant (Baum et al., 2008). Iverson (2000) mathematically explained which type of movement would be significant in which time interval for nearly saturated soil. The lateral flow will be dominant within the time interval that is longer than the contributing area (drainage basin of the slope) over diffusivity ($t > A/D_0$). In a shorter time than D^2/D_0, (where D is depth of slide surface) the transient effect of vertical infiltration governs the pore pressure response. However, there is no agreed period for the antecedent period. Generally, two weeks to one month mean precipitation is applied for antecedent rainfall (Baum et al., 2010; Marin & Mattos, 2020; Medina et al., 2021). Since the period is long and rainfall intensity is low, evapotranspiration is also essential, while it is neglected in event rainfall (Simoni et al., 2008). Steady-state hydrological models do not necessitate antecedent rainfall.

2.4.1.2   Geotechnical parameters

Depending on the complexity of the model, different geotechnical parameters are required for physically-based models such as internal friction angle ($\emptyset'$), effective cohesion (c'), hydraulic conductivity (k_s), unit weight (γ), soil-water retention curve (SWRC) parameters, hydraulic conductivity function (HCF) etc. Determining these parameters as representative of the whole study area is essential to accurate susceptibility zonation. However, obtaining these parameters may not always be possible. In the lack of adequate site investigation, suggestions from the literature can be adopted considering different textural and lithological classes and might be calibrated (Hürlimann et al., 2022).

The models considering material uncertainty are more accurate than the deterministic model (Medina et al., 2021; Raia et al., 2014). At the same time, spatial variation of these parameters also affects the model performances (Oguz et al., 2021).

2.4.1.3   Soil thickness

Soil thickness is one of the main components of sensitivity modeling, which refers to the depth from the surface to the more consolidated layer (Corominas et al., 2014). Many studies have shown that model performances increase when the variability of soil thickness throughout the study area is considered (Catani et al., 2010; Dietrich et al., 2007; Lanni et al., 2012). For this reason, different strategies have been proposed to model the soil depth continuously in the field. These strategies include; using different soil thicknesses at various locations throughout the study area (Baum et al., 2005), spatial interpolation (Kim et al., 2013), associating soil thickness with simple topographical parameters (Salciarini et al., 2006; Saulnier et al., 1997), process-based soil production model (Dietrich et al., 2007) and building multivariate statistical models (Segoni et al., 2012; Tesfa et al., 2009). In addition to these models (Vieira et al., 2010, 2018) considered different depth scenarios for the study area considering possible movable layers.

2.4.1.4   Vegetation

Vegetation affects the slopes both hydrologically and mechanically. From a hydrological point of view, the vegetation shows the feature of decreasing surface runoff and increasing infiltration. At the same time, leaves store water during rain and delay the meeting of rainwater with the soil (Kim et al., 2013; Oorthuis et al., 2021). At the same time, plant roots reduce the moisture content of the soil before the precipitation due to transpiration (Oorthuis et al., 2021). The mechanical contribution of the plant roots is to increase their stability by anchoring the soil. This effect is included in the analysis as root cohesion which varies according to the type of vegetation (Guo et al., 2022; Hürlimann et al., 2022). Vegetation density also affects the overall contribution of roots to soil stability (Moos et al., 2016). Furthermore, the surcharge effect can also be considered as a reducing factor for the slope stability (Kim et al., 2013; Wu & Sidle, 1995).

2.4.1.5   Digital Elevation Models

Digital elevation models provide a base map to perform stability analysis for susceptibility modeling. The accuracy of the DEM is crucial for evaluating predisposing factors to landslides (Godt et al., 2008). Also, the resolution of DEM influences the model performance by affecting the derived slope and contribution area (Claessens et al., 2005; Fuchs et al., 2014; Tarolli & Tarboton, 2006).

2.4.2   Performance evaluation

Quantitative performance analysis is crucial for making a reliable prediction about future events (Corominas et al., 2014). Therefore, several methods for performance assessment have been proposed in the literature. These proposals are success rate curves (Zinck et al., 2001), receiver operating characteristic, ROC, curves (Baum et al., 2005; Zizioli et al., 2013), Succes index (SI) and error-index (EI) (Sorbino et al., 2010), scar concentration, and landslide potential (Vieira et al., 2010) probability of detection-false alarm ratio and critical success index (Liao et al., 2011), D index (Liu & Wu, 2008) ,and landslide ratio (LR ratio) for each predicted FS class (Park et al., 2013). Frattini et al. (2010) incorporated the cost curve into the ROC curves to quantify the cost arising from false classification.

This section describes the ROC curve which is adopted in this study because it is the most widely used accuracy statistic in the literature with multiple performance indices (Medina et al., 2021; Oguz et al., 2021; Salciarini et al., 2008; Schilirò et al., 2016). Many of the performance indices mentioned above are very similar to the different metrics in ROC analysis.

ROC curves are a method produced for the correct classification of radio signals and are used in many different areas apart from landslide studies today such as medicine (Obuchowski & Bullen, 2018). The creation of the curve is based on binary classification (positives and negatives). Thanks to the ROC curves, different functions that perform binary classification can be compared. In addition, the critical

value (cut-off) of the selected function can be determined to make the optimum classification.

Binary classification is made by using a threshold value of the test function (this function may be the safety factor or the probability of failure). Then a contingency table is created by comparing the classification and the observation (Table 2.3). The indexes shown in Table 2.4 are calculated with the values obtained from this table.

Table 2.3 Contingency table for ROC analysis.

Model Prediction	Observation	
	Positive (Landslide)	**Negative (Stable)**
Positive (P)	True Positive (TP)	False Positive (FP)
Negative (N)	False Negative (FN)	True Negative (TN)

Table 2.4 Accuracy statistics used in this study.

True Positive Rate, TPR (Sensitivity)	$\dfrac{TP}{TP + FN}$
False Positive Rate, FPR (1-Spesificity)	$\dfrac{FP}{FP + TN}$
Accuracy (ACC)	$\dfrac{TPR + (1 - FPR)}{2}$
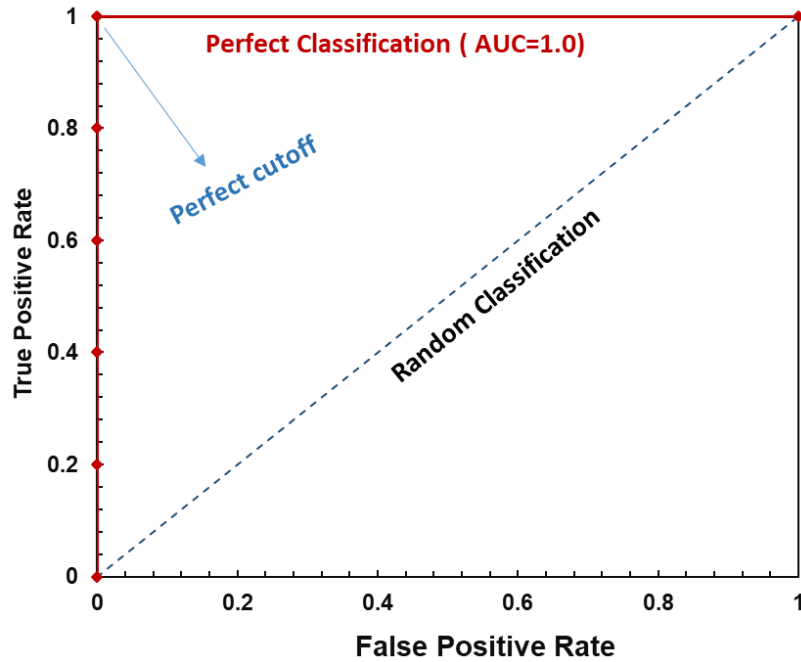
Figure 2.3. ROC curve plane and perfect classification.

Binary classification is made with multiple thresholds, and the ROC curve is drawn on the TPR-FPR plane. Area under ROC curve (AUC) is 1.0 for a perfect classification, and the ideal cutoff value is the left upper corner (Figure 2.3). For a deterministic physically-based model natural cutoff value is FS equal to 1.0. However, different cutoff values can also be employed because the errors come from DEM resolution, stability model selected, and material uncertainty (Zieher et al., 2017).

Although ROC curves are valuable tools for accuracy assessment, they lack spatial information of the error, which is their drawback (Corominas et al., 2014).

2.5   Theoretical Background of TRIGRS, FSLAM, and SCOOPS3D

2.5.1   TRIGRS

The Transient Rainfall Infiltration and Grid-Based Regional Slope-Stability Model (TRIGRS) computes time-dependent pore pressure and respective change of the

factor of safety due to rainfall (Baum, Savage, et al., 2008). It can calculate pore pressure change based on saturated (Baum et al., 2002) and unsaturated (Baum, Savage, et al., 2008) initial conditions. The saturated version infiltration method is based on the method proposed by Iverson (2000), and the unsaturated infiltration model uses the analytical solution of the Richards equation given by Srivastava and Yeh (1991). In this study, only the unsaturated model of TRIGRS is adopted, which is explained below.

The unsaturated model of TRIGRS considers soil as a two-layered (saturated and unsaturated) system (Baum et al., 2010). The unsaturated layer stores the infiltrated water and transmits the rest to the saturated part. The constitutive relation between soil suction and hydraulic conductivity and volumetric water content is defined by Gardner (1958) as follows.

$$K(\Psi) = K_s \exp(\alpha \Psi^*) \tag{2.1}$$

$$\Theta = \Theta_r + (\Theta_s - \Theta_r)\exp(\alpha \Psi^*) \tag{2.2}$$

Where, K_s is saturated hydraulic conductivity, Ψ is suction head, $\Psi^* = \Psi - \Psi_0$, where Ψ_0 is equal to 0 or -1/α depending on whether capillary rise exists (Baum, Savage, et al., 2008). $\Theta, \Theta_s, \Theta_r$ are volumetric water content relevant to pressure head, saturated and residual water content, respectively, and α is inverse of the capillary rise.

Initial hydraulic conductivity of unsaturated layer is calculated employing steady-state background flow;

$$K(Z, 0) = I_{zlt} - [I_{zlt} - K_s \exp(\alpha_1 \Psi_0) \exp(\text{-}\alpha_1(d_u - Z)] \tag{2.3}$$

And hydraulic conductivity change with time and depth is given as;

$$K(Z,t) = I_{nz} - [I_{nz} - K_s \exp(\alpha_1 \Psi_0) \exp(-\alpha_1(d_u - Z)]$$

$$-4(I_{nz} - I_{zlt}) \exp(\frac{\alpha_1 Z}{2}) \exp(-D_\Psi \frac{t}{4})$$

$$\cdot \sum_{m=1}^{\infty} \frac{\sin[\Lambda_m - \alpha_1(d_u - Z)]\sin[\Lambda_m \alpha_1 d_u]}{1 + \frac{\alpha_1 d_u}{2} + 2\Lambda_m^2 \alpha_1 d_u} \exp(-\Lambda_m^2 D_\Psi t) \tag{2.4}$$

Where Λ_m is the positive roots of Eqn. 2.5.

$$tan(\Lambda \alpha_1 d_u) + 2\Lambda = 0 \tag{2.5}$$

Time-dependent change of vertical pressure head distribution is

$$\Psi(Z,t) = \frac{\cos(\theta)}{\alpha_1} \ln\left[\frac{K(Z,t)}{Ks}\right] + \Psi_0 \tag{2.6}$$

In Eqn 2.4, I_{zlt} is steady-state background flow I_{nZ} is the rainfall infiltration in the corresponding time interval, α_1 is equal to $\alpha \cos^2(\delta)$ (Figure 2.4), and D_Ψ is soil water diffusivity which is;

$$D_\Psi = \frac{\alpha_1 K_s}{(\theta_s - \theta_r)} \tag{2.7}$$

The infiltration in each time interval is limited by saturated hydraulic conductivity. The excess rainfall is computed as surface runoff and transferred to adjacent grids according to the flow direction of DEM simultaneously in the same time interval.

Figure 2.4. Illustration of TRIGRS model.

Basal flux at the bottom of the unsaturated soil is calculated at the end of each time step (Eqn 2.8). Then, excess flux calculated from the difference between unsaturated basal flux and bedrock drainage (Eqn 2.9 and Eqn 2.10) is used to calculate water table rise.

$$q(d_u, t) = I_{nZ} - 4(I_{nZ} - I_{zlt}) \exp\left(\frac{\alpha_1 d_u}{2}\right) \exp\left(-D_\Psi \frac{t}{4}\right)$$

$$\cdot \sum_{m=1}^{\infty} \frac{\Lambda_m \sin[\Lambda_m - \alpha_1 \sin[\Lambda_m \alpha_1 d_u]}{1 + \frac{\alpha_1 d_u}{2} + 2\Lambda_m^2 \alpha_1 d_u} \exp(-\Lambda_m^2 D_\Psi t)$$

(2.8)

$$q_{zmax} = K_s(\beta - 1)$$

(2.9)

In Eqn 2.9, $\beta = \cos^2(\theta) - I_{Zlt}/K_s$.

$$q_{zex} = 0 \ if \ q(d_u, t) \le c_d(q_{zmax} - I_{Zlt})$$

$$or \ q_{zex} = q(d_u, t) - c_d(q_{zmax} - I_{Zlt})$$

(2.10)

23

In Eqn 2.10, the c_d is a constant equal to 0.1 for an impervious boundary.

The factor of safety calculation can be conducted in TRIGRS in different depths based on the infinite slope equation;

$$FS(Z,t) = \frac{\tan(\emptyset')}{\tan(\theta)} + \frac{C - \Psi(Z,t)\gamma_w\tan(\emptyset')}{\gamma_s Z sin(\theta)cos(\theta)} \qquad (2.11)$$

Where, Ψ(Z, t) is pore pressure head and where the soil is unsaturated Ψ(Z, t) is multiplied by effective saturation which is $\chi = (\Theta - \Theta_r) / (\Theta_s - \Theta_r)$.

In this section, only basic equations of TRIGRS defined by Baum et al. (2008, 2010) are provided above to show essential parameters to compute pore pressure change. A detailed description of the models can be found in the original references.

In this study, TRIGRS v.2.1 (M. Alvioli & Baum, 2016) is utilized to compute pore pressures during rainfall.

2.5.1   FSLAM

In FSLAM, water table height at the bottom of a particular soil column is calculated employing contributing area (a) of the cell in which soil column is located and antecedent recharge (q_a) following the methodology proposed by Montgomery and Dietrich (1994).

$$h_a = \frac{a}{b}\frac{q_a}{KZcos\theta sin\theta} \qquad (2.12)$$

Where K is horizontal hydraulic conductivity, b is the cell size of the raster, and a is the contributing area of the cell.
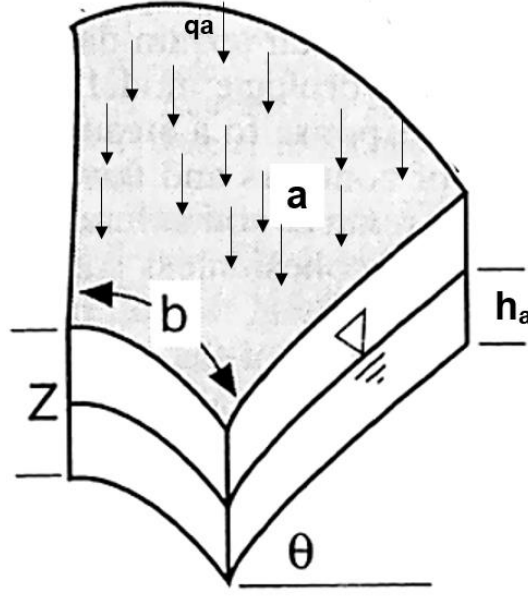
Figure 2.5 Calculation of height of water table before the event rainfall (modified from Montgomery & Dietrich, (1994).

Water table rise due to event rainfall is calculated by Eqn. 2.13

$$h_e = \frac{q_e}{n^*} \tag{2.13}$$

In Eqn. 2.13 q_e is total event infiltration which is computed by curve number (CN) (Eqn 2.14) used in surface hydrology (USDA, 1986). The n^* is considered as a calibration term in this study instead of using soil porosity proposed by Medina et al. (2021) , which is discussed in section 3.3.2

$$q_e = P_e - \frac{(P_e - (\frac{5080}{CN} - 51))^2}{P_e + 4(\frac{5080}{CN} - 51)} \tag{2.14}$$

Where, Pe is the cumulative event rainfall.

Following the Eqn. 2.12-14 factor of safety is calculated at the bottom of the soil column with infinite slope assumption (Eqn 3.18)

$$FS = \frac{\tan(\phi')}{\tan(\theta)}(1 - (\frac{h_a + h_e}{Z})(\frac{\rho_w}{\rho_s})) + \frac{C}{\rho_s Z g sin(\theta)cos(\theta)} \tag{2.15}$$

The cohesion term in Eqn 2.11 and 2.15 should be considered as the total of cohesion provided by soil (c'_s) and plant roots (c_r).

Additionally, FSLAM is able to compute the probabilistic distribution of Factor of Safety considering cohesion and friction angle as normally distributed parameters. The analytical solution of the distribution of FS can be found in (Medina et al., 2021).

2.5.1   SCOOPS3D

SCOOPS3D applies the 3D method of column approach to calculate the factor of safety (Reid et al., 2000, 2015). A three-dimensional search lattice is generated for trying spherical failure surfaces. Each point on the search lattice is determined as the center of the trial surface. While varying the radius, SCOOPS3D calculates stability of spherical failure surface by employing DEM data, 3D material properties, and ground water conditions (Reid et al., 2015). The illustration of the search is shown in Figure 2.6.

Firstly, columns involved in the failure surface are determined for each potential failure surface. The planar failure surface is assumed considering the location of points that slip surface enter and exit the soil column. Then the volume of the column above the failure surface is calculated. Failure surface may include either full or partial columns (Figure 2.7), which increases the accuracy of stability calculation and reduces the number of columns needed for satisfactory approximation (Reid et al., 2015). The weight of the column is calculated by Eqn 2.16.

$$W_c = \int V_c \gamma(z) dz \qquad (2.16)$$

Where V_c is the volume of the column, $\gamma(z)$ is the unit weight of the soil.
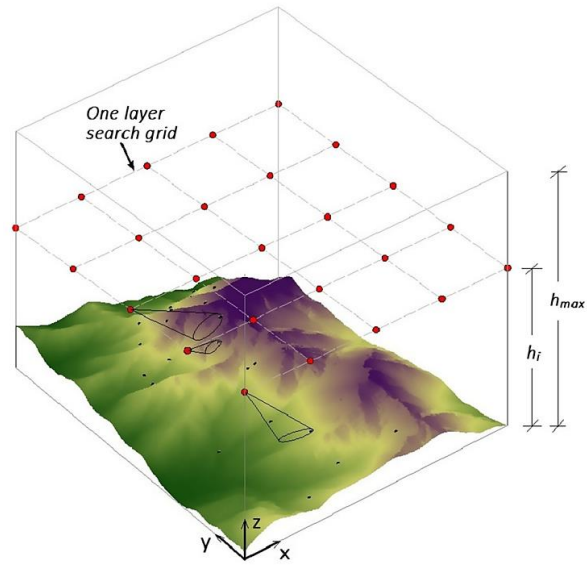
Figure 2.6. Illustration of search lattice (Tran et al., 2018).
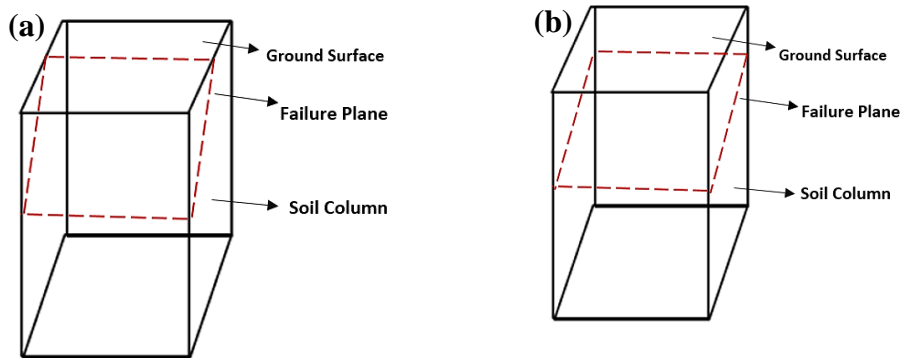
Figure 2.7. (a) Partial column (b) full column

The shear strength of the soil on the trial surface is calculated by the Coulomb-Terzaghi rule (Reid et al., 2000).

$$\tau = c' + (\sigma_n - u)\tan(\emptyset') \tag{2.17}$$

Where, σ_n is total stress normal to failure surface, u is pore pressure. When pore pressure is negative, SCOOPS3D can calculate the contribution of suction to shear strength, but in this study, suction is ignored in the SCOOPS3D for simplification. The factor of safety of the entire failure surface can be modeled by a 3D extension of the Ordinary Fellenious method or Bishop's simplified method in SCOOOPS3D. The difference between the two models is that whereas the Ordinary method neglects the intercolumn forces, Bishop's method assumes their direction to be horizontal. On the other hand, both methods satisfy both force and moment equilibrium in contrast to the method proposed by Hovland (1977). In this study, Bishop's simplified method (Eqn 2.18) is adopted to calculate FS, since it is more accurate especially where positive pore pressure exists (Reid et al., 2015).

$$F_{s3D} = \frac{\sum R_{i,j}[c_{i,j}A_{h_{i,j}} + (W_{i,j} - u_{i,j}A_{h_{i,j}})tan\emptyset_{i,j}]/m_{\alpha_{i,j}}}{\sum W_{i,j}(R_{i,j}sin\alpha_{i,j} + k_{eq}e_{i,j})} \qquad (2.18)$$

In Eqn. 2.18 $R_{i,j}$ the radius of failure surface, $A_{h_{i,j}}$ is the horizontal area of the soil column, $u_{i,j}$ is pore pressure at failure surface, $\alpha_{i,j}$ is apparent dip angle (Figure 2.8) of failure surface on column base, k_{eq} is horizontal pseudo-acceleration, $e_{i,j}$ is moment arm of horizontal force, $m_{\alpha_{i,j}} = cos\varepsilon_{i,j} + (sin\alpha_{i,j}tan\emptyset_{i,j})/F_{s3D}$, where $\varepsilon_{i,j}$ is true dip of trial surface (Figure 2.8).
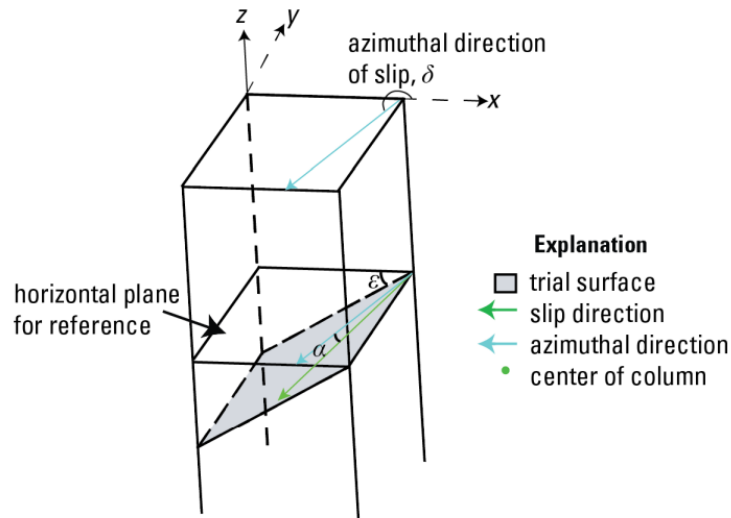
Figure 2.8 Dip angles of failure surface at the base of soil column (Reid et al., 2015).

In a particular column, many failure surfaces pass through. SCOOPS3D reports the minimum factor of safety for each column.

Regarding pore pressure, different options exist in SCOOPS3D, defining 3D pore pressure distribution, piezometric level, or pore pressure ratio.

2.6   Literature Review on TRIGRS, FSLAM, SCOOPS3D

2.6.1   TRIGRS

This section will summarize studies using TRIGRS, FSLAM, and SCOOPS3D. Compared to FSLAM and SCOOPS3D, TRIGRS has been implemented in many places. For this reason, only some of the studies using TRIGRS will be described. While selecting the studies, the place in the literature and the use of TRIGRS for different purposes, and the evolution of the software were taken into consideration.

Thanks to TRIGRS transient pore pressure capability, it is used in susceptibility assessment and assessment of rainfall threshold and hazard analysis. For this purpose, Salciarini et al.(2008) adopted TRIGRS to calculate the recurrence period

of rainfall triggered landslides occurring on the slopes of Seattle, using different rainfall intensity-duration-frequency, IDF curves.

Baum et al. (2010) introduced the unsaturated module of TRIGRS and applied it to landslides in Seattle. At the end of the application, the unsaturated module correctly predicted less landslide area instability than the saturated module and the static saturation situation (m=hw/z=1), whereas overestimated unstable areas also were much less than others (Baum et al., 2010).

Sorbino et al. (2010) applied TRIGRS to landslide types with different failure mechanisms that they detected in Campania region (northern Italy). It has been emphasized that although the performance of TRIGRS is better compared to SHALSTAB, the model accuracy varies according to different landslide types, and some types of landslides cannot be modeled with TRIGRS. The study also highlighted that although SHALSTAB had low accuracy in landslide detection, it can be employed to distribute pore water pressure measurements in the field for use as initial conditions for TRIGRS.

Liao et al. (2011) introduced the Matlab version of TRIGRS (MaTRIGRS) and used it to predict landslides triggered by hurricanes in Macon County (North Carolina). In the same study, they proposed Probability of Detection (POD) and False Alarm Ratio (FOS) in an early warning system.

Park et al. (2013) employed TRIGRS to detect the initiation points of the debris flow in the Woomyeon Mountain area in Seoul (South Korea). Then utilizing a flow routing scheme, debris flow susceptibility zones were established.

Kim et al. (2013) incorporated tree surcharge and root cohesion into the TRIGRS model and showed the mechanical contribution of trees to slope stability during rainfall in Bonghiwa, Korea.

Raia et al. (2014) created the probabilistic version of TRIGRS, which handles hydraulic and mechanical parameters' uncertainties. The model includes both normal distribution and uniform distribution options of input parameters. While the latter is proposed for areas that are poorly investigated, normal distribution is

suggested when sufficient geotechnical exploration is available. They showed that the probabilistic model has better performance to estimate landslides in Seattle comparing with deterministic model.

Uncertainty in the initial water table depth dramatically affects the performance of TRIGRS analyses. To overcome this difficulty, Grelle et al. (2014) proposed an exponential slope-dependent function for the initial water table of TRIGRS and optimized the function to minimize initially unstable areas. Their strategy ended up with high performance in terms of the ratio of correctly predicted landslide areas to overestimated unstable areas (SI/EI).

Alvioli et al.(2014)employed TRIGRS to estimate the landslide size distribution and determine the required I-D threshold value for landslide triggering in Upper Tiber River Basin (Central Italy). Their findings pointed out that TRIGRS can reproduce two scaling properties of landslides (Alvioli et al. 2014). Then Alvioli et al. (2018) investigated the impact of climate change on hazard assessment considering change of the previous study's findings.

Viet et al. (2017) examined the impact of DEM decisions on TRIGRS performance. Their results showed that the ideal grid size differs in finding the landslide location and predicting the failure time. Furthermore, Sarma et al. (2020) reported that DEMs from diverse sources resulted in different performances.

There are few studies which focused on parameter uncertainty in the literature. Zieher et al. (2017) tested ten thousand different combinations of input parameters to calibrate the input parameters deterministically. Depina et al. (2020) proposed a Bayesian framework to take spatial variability of soil parameters into account to improve the performance of TRIGRS.

2.6.2   FSLAM

UnlikeTRIGRS, since FSLAM is a new model, it has been employed only in a few places in the literature. FSLAM is introduced by (Medina et al., 2021) with

theoretical background, assumptions, and sensitivity analysis. Cohesion was determined as the most critical parameter in the sensitivity analysis. The model is successfully applied in Andorra in an area larger than 100 km^2, in very short computational time. Furthermore, the probabilistic and deterministic approaches were compared, and the probabilistic model is assessed to be more accurate than the deterministic model (Medina et al., 2021).

In Hürlimann et al. (2022), FSLAM was used in the Val d'Aran region (Pyrenees, Spain) to determine landslide-prone areas in the future, under changes in climate and land use and land cover, LULC. A landslides episode in 2013 is employed for model calibration. They concluded that although average daily rainfall will increase in the future, landslide-prone areas will reduce because of the growth of forest areas.

QGIS plugin of FSLAM is published recently (Guo et al., 2022). That paper explains how to use plugins via QGIS. In addition, landslide episodes in 1982 in Berguedá (NE Spain) were replicated using FSLAM.

2.6.3   SCOOPS3D

Although SCOOPS3D is applied for hazard assessment on a slope and regional scale, few studies employed SCOOPS3D for rainfall-induced landslides (Baum et al., 2002, 2005; Brien & Reid, 2007; Ma, 2018).

Tran et al. (2018) combined TRIGRS and SCOOPS3D for the first time to assess time-dependent stability. The infiltration analysis of the landslides in 2011 on the Umyeon mountain in South Korea was conducted by TRIGRS and the infinite slope assumption and SCOOPS3D are adopted for the stability analysis. They report that SCOOPS3D resulted in less unstable area than that estimated by TRIGRS. Although the correctly estimated landslides were more in TRIGRS, SCOOPS3D had slightly better performance in terms of the LR class index.

He et al.(2021) applied SCOOPS3D and TRIGRS combinations to determine the rainfall threshold in the Niangniangba river basin in China. They compared the

ability of TRIGRS and SCOOPS3D to replicate landslide episodes in 2013. Confirming the result reported by Tran et al. (2018), SCOOPS3D ended up with a higher LR class ratio. Moreover, the correctly predicted landslide area is also larger in their studies.

Palazzolo et al. (2021) applied a genetic algorithm to improve the search performance of SCOOPS3D. In their model, SCOOPS3D gave more unstable areas than TRIGRS both in landslide areas and in other units of terrain. The LR class index of SCOOPS3D was higher than that of the infinite slope solution, similar to other studies.

CHAPTER 3

MATERIALS AND METHODS

3.1 Study Area

3.1.1 Location of the study area

The study areas, Yesiltepe, Kaptanpasa, Gurpınar, and Cukurluhoca villages, are situated in Cayeli County of Rize. Rize province is one of the most prone areas to rainfall-triggered landslides in Turkey, because of its mountainous topography, steep slopes, high annual average rainfall (Uyeturk et al., 2020), and frequent high-intensity short-duration rainfall events (recurrence period of 100 mm/day, which is very-high-intensity short-duration rainfall event, in Rize is 1.8 years (Çiçek, 2015))), high relative humidity throughout the year (annual average relative humidity is 80%) ((Polat & Sunkar, 2017))), city with the highest number of rainy days per year (178.5 days (Çicek, 2015)), recent land-use alteration, and deforestation due to the high demand for tea plantations.

The areas of interest cover an area of 14 km^2 which are located between 40°55'54" − 40°58'30" N latitude and 40°45'17" − 45°49'10" E longitude. The location of the site is shown in Figure 3.1. The elevation and slope are derived from the 1/25000 scale contour map provided by the General Directorate of Mapping, Turkey. According to the 10 m resolution Digital Elevation Model (DEM), the elevation of the study area changes between 370 to 1207 m. The maximum slope is calculated as 67.5 degrees. Elevation and slope maps are shown in Figure 3.1b and Figure 3.1c, respectively.
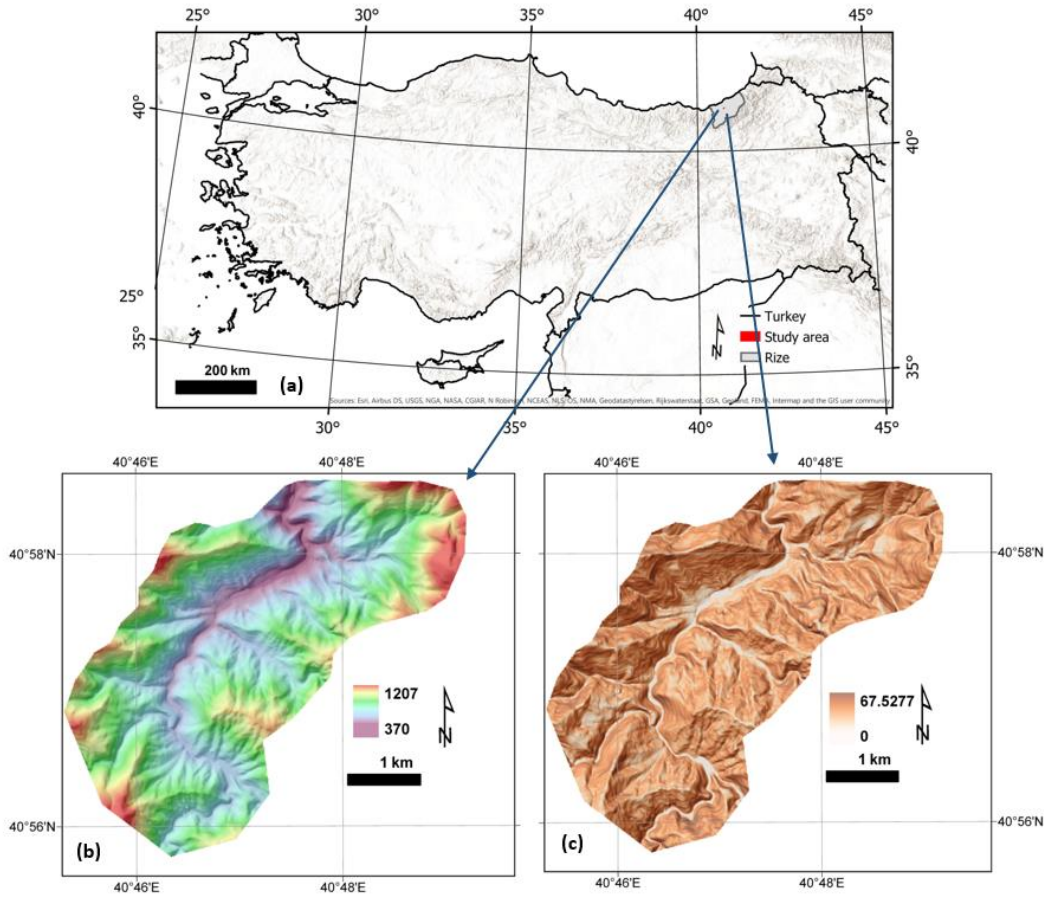
Figure 3.1. (a) Location of the study area. (b) Digital elevation model (c) slope map.

3.1.2   Regional geology

The regional geology of Rize province is studied by Alan et al. (2019), Gedik et al. (1992), and Tuysuz et al. (2008). Latest study performed by Alan et al. (2019) reports that the geology of the area of interest consists of Çatak formation, Kızılkaya formation and Kaçkar granitoid 1. The Çatak formation consists of sandstone, siltstone, marl, shale, limestone, basalt, andesitic lava, and pyroclastics. Kızılkaya formation is composed of rhyolitic, clayey limestone, and dacitic lavas, in which alteration is widely observed. Kaçkar granitoid composed of granite, granodiorite, diorite, tonalite and monzonite (Alan et al. 2019). Landslides are observed on the residual soil that lies on these geological units. Geology map of the area is illustrated in Figure 3.2.
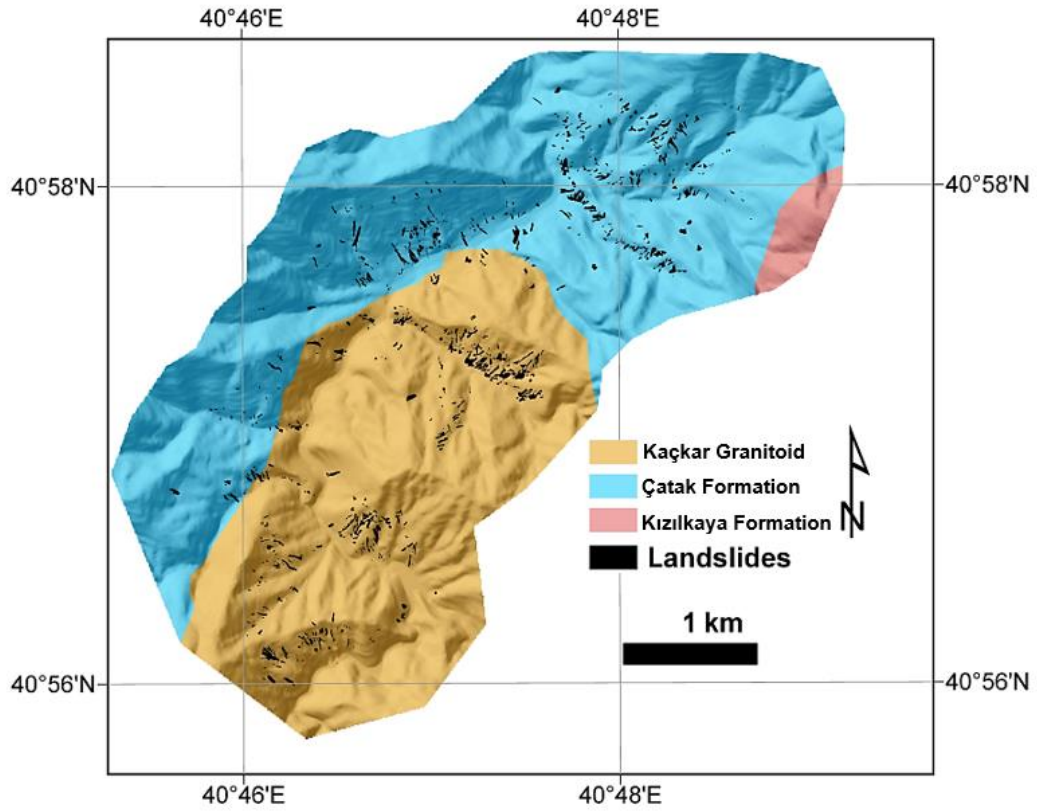
Figure 3.2. Geology of the study area with landslides.

3.1.3 Rainfall

Intense rainfall between September 27 to October 4, 2017, triggered many landslides. There is one rainfall station in the study area. Rainfall data obtained by this station is shown in Figure 3.3. Cumulative rainfall recorded by the station is 175 mm, and daily rain is measured as 61 mm and 56 mm on September 27 and on October 1. Based on the data from 1928 to 2020, the average monthly rainfall in Rize changes between 96 mm to 292.3 mm (TSMS, 2021). The rainiest months are October (292.3 mm), November (255.2), and September (254.8 mm) (TSMS, 2021).

Although many of these landslides were reported between September 27-29, inventory data was obtained by Comert et al. (2019) after October 4. Reported landslides by Comert et al. (2019) can be seen in Figure 3.2. Therefore, landslides triggered after September 29 can be involved in inventory data. Landslides that

occurred between September 27-29 caused one casualty and evacuation of one hundred houses.
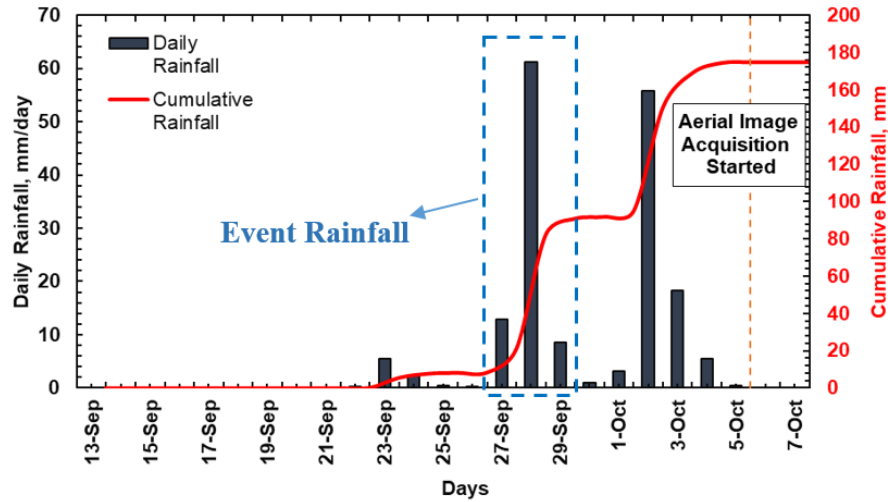
Figure 3.3. The rainfall data obtained by the nearest rainfall station.

3.1.1 Land use and land cover

The majority of the study area is covered by forest and tea plantations (Figure 3.4). Tea planted areas are located near the houses of local people. These areas were observed to have more landslides. Although it is challenging to identify landslides under forest cover, data obtained by Comert et al. (2019) are believed to capture most of the failures under trees as landslides are fresh at the time of data acquisition.
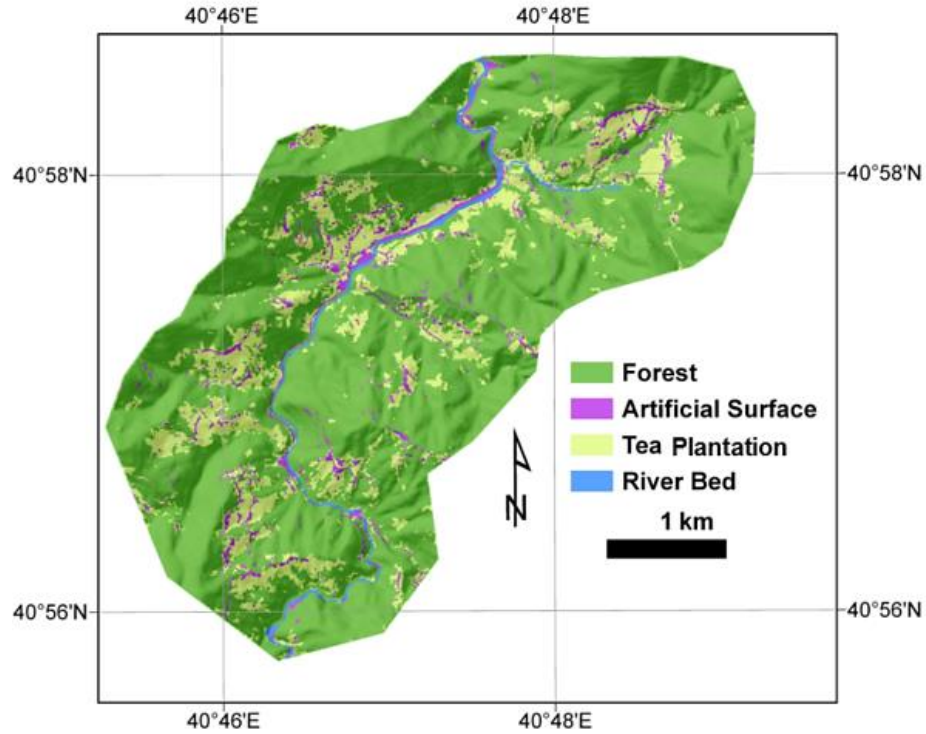
Figure 3.4. Land cover and land use map (Comert, 2022 (personal communication)).

3.2 Landslide Inventory

Landslide inventory data and the 10 cm resolution digital surface model (DSM) provided by Comert et al. (2019) are employed to obtain morphometric features of failure source areas.

3.2.1 3D visualization: RRIM images

First of all, discrimination of landslides' source areas is needed. For this purpose, red relief images (RRIM) are derived (Chiba et al., 2008) as can be seen in Figure 3.5. RRIM images are a way of 3D visualization of a surface model produced by superposing I-value map and slope map. The advantage of these images is to be independent of azimuthal direction (Chiba et al., 2008). Detailed description of production and use of these images for landslide mapping can be found in Gorum (2019). In this study, to derive required data SAGA GIS, 7.8.2 is used. An example

of a landslide and corresponding RRIM is shown in Figure 3.5a and Figure 3.5b. After deriving RRIM images, source areas of landslides are identified. Contour lines are also utilized to accurately determine the borders of source areas.

3.2.2   Determination of morphometric characteristics of landslides

Landslides' length (L), horizontal length (L_H), the vertical depth of slide surface (D), thickness normal to the surface (t), slope height (H), area, width (w) slope of landslides (θ) are considered geometric features in this study. These morphometric features are illustrated in Figure 3.5c. The protocol suggested by Slaughter et al. (2017) is followed. Adjacent stable slope is used as suggested by Slaughter et al. (2017) to calculate the mean slope angle of failures. However, two different methods are adopted to calculate the depth of the failure surface. Slaughter et al. (2017) proposed to measure landslides' depth at the scarp of landslides. Scarp height is recommended to be considered as the depth of the failure surface. Nevertheless, this procedure is unsuitable since it overestimates the depth of failures in which the scarp profile is not vertical. Therefore, this procedure is modified as in Eqn. 3.1. Additionally, the depth of landslides is measured by taking cross-section through flow direction. The original approach proposed by Slaughter et al. (2017) is named as Original Washington Protocol (OWP), the modified version in this study is named as Modified Washington Protocol (MWP), and taking cross-section is named as X-section method. OWP method is used for comparison purposes, whereas other two approaches are needed because measuring the scarp length or obtaining a reliable cross-section is not possible for some situations. These are;

(i)   If an obstacle (such as houses, trees, retaining structures) hindering ground features (Figure 3.6a-b-d) is located at scarp, MWP can not be used. If these obstacles are located at the side of the failure X-section method is not applicable.

(ii)   Cases that topography unevenly changes (Figure 3.6b): In these cases, the X-section method results in either overestimation or underestimation of failure depth.

(iii)   Adjoint landslides (Figure 3.6c): In this case, the relevant method can not be used where adjoint landslides exist.

$$D = H_s - L_s \cdot \tan \theta \qquad\qquad (3.1)$$

Scarp height is measured at different locations, as Burns & Madin (2009) recommended. Multiple cross-sections are taken along the flow direction. The maximum depth measurement is assigned as the maximum depth of landslides. The mean of the depth measurements is considered as the mean depth of landslides.

The area of landslides' sources is calculated automatically by ArcGIS 10.7. The width of landslides is calculated by dividing landslide area by landslides' length (A/L_H). The thickness of landslides is calculated by the following equation.

$$t = D \cdot \cos (\theta) \qquad\qquad (3.2)$$
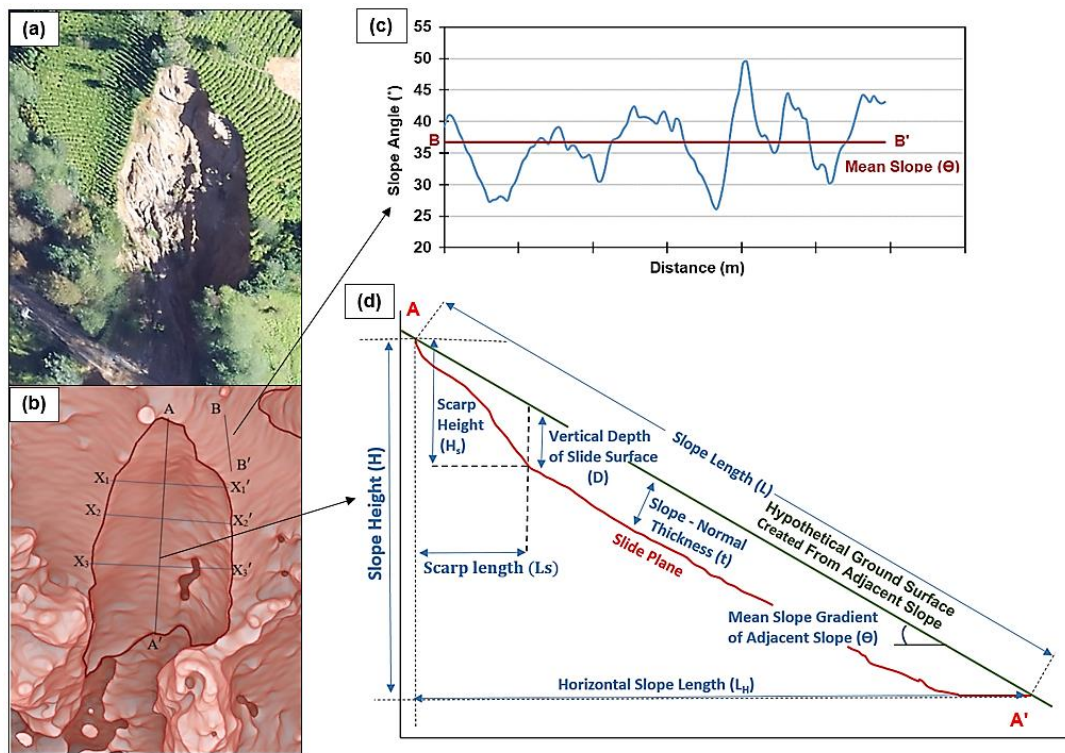
Figure 3.5. (a) Orthophoto of a landslide (b) RRIM images (c) mean slope calculation (d)illustration of morphometric fetures.

Figure 3.6. The cases reducing reliability of depth calculation methods. (a) an obstacle on scarp (b) unevenly changing topography (c) adjoint landslides (d) dense tree cover.

3.2.3   Volume calculation

The volumes of the failures are calculated by two methods (i) half ellipsoid (Cruden and Varnes 1996), (ii) multiplying area, and mean depth derived by X-section method (prism method). The failure shape assumptions of these two methods are shown in Figure 3.7. Firstly, equivalent width is calculated, assuming the failure area is an ellipse, to use the half ellipsoid method. The following equation is used:

$$\text{V} = \frac{1}{6} * \pi * D_{max} * W_{eq} * L \qquad\qquad (3.3)$$
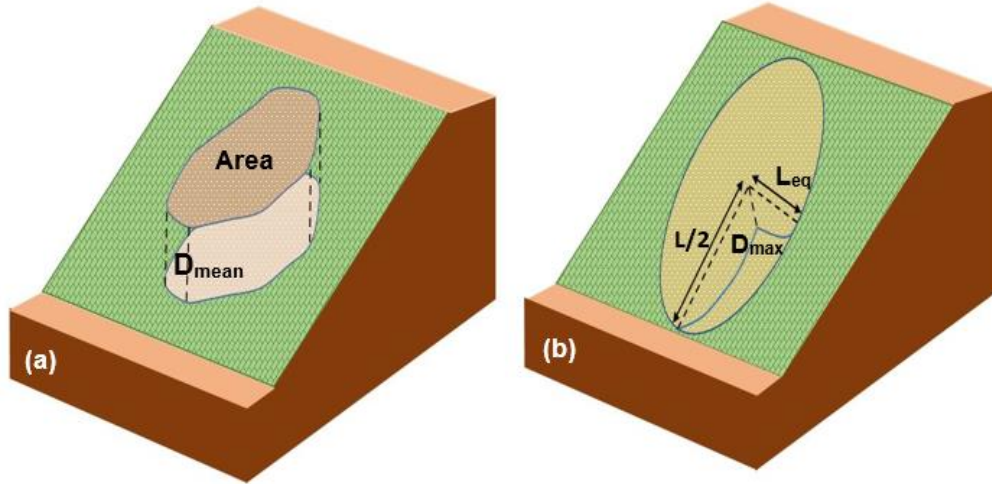
Figure 3.7. Volume calculation methods (a) prism method (b) ellipsoid method.

3.3   Physically-based modeling

To perform a back-analysis of the failures that took place during the event, FSLAM and TRIGRS are selected as hydrological models. As stated previously, FSLAM involves both vertical and lateral low, whereas TRIGRS considers only vertical infiltration. Furthermore, TRIGRS computes time-dependent change of pore

pressures (transient analysis). On the other hand, FSLAM considers the asymptotic situation, in which all infiltrated rainfall accumulates at the bottom of the soil column. Therefore, their computational times are also different from each other (Medina et al., 2021). Accordingly, the purpose of using these models is to compare different hydrological assumptions with varying levels of complexity. To compare alternating stability assumptions, SCOOPS3D is adopted as an alternative to the infinite slope assumption of TRIGRS and FSLAM.

The water table depth computed by FSLAM and equivalent piezometric level to pore pressure at failure surface in TRIGRS is defined for SCOOPS3D analysis.

In addition to stability and pore pressure assumptions, search parameters are also relevant for the accurate determination of safety factors in SCOOPS3D. These parameters are maximum and minimum area or volume of landslides, the vertical and horizontal resolution of search lattice, the maximum and minimum height of search lattice, resolution of the DEM file.

Since optimum parameters may change through the terrain, an iterative approach is adopted in this study. Search parameters are set firstly by considering the suggestion of Reid et al. (2015) (Table 3.1). Then, these parameters are extended to check if the results are affected by the limits. Furthermore, SCOOPS3D has two search options: simple search and coarse to fine search. In the preliminary sensitivity analysis coarse to fine search was observed to be inaccurate though it is more computationally efficient (Reid et al., 2015). This could be due to the complex topography of the study area. Therefore, a simple search option is employed in all analyses.

Table 3.1 Initial Search parameters in SCOOPS3D.

Search Parameter	Initial Selection
Maximum Area (Amin), m^2	2000
Minimum area (Amax), m^2	100
Maximum elevation of Search Lattice (Zmax), m	The maximum elevation of search area + 2 times topographic relief
The maximum elevation of Search Lattice (Zmin), m	Minimum elevation of search area + half of topographic relief
Vertical Resolution, m	Equal to DEM resolution
Radius Increment, m	Half of DEM resolution
The horizontal extent of search lattice	Equal to DEM file
Horizontal multiplier	5

3.3.1   Available data and sensitivity analysis

Uyeturk et al. (2020) and Uyeturk and Huvaj (2021) conducted a geotechnical characterization of residual soils of landslide-prone areas of Rize province. The sampling sites of these studies do not cover the current study area. However, they provide a reliable range for estimating relevant material properties in similar soils in Rize. Therefore, calibration of these material properties is needed. Since calibration of all parameters is not possible, sensitivity analysis is performed to determine the most relevant inputs.

Sensitivity analysis is conducted for (i) understanding the importance of each parameter (ii) selecting the parameter set to be calibrated (iii) determining the impact of each important parameter on the factor of safety in the available data set (iv) comparing the influence of similar parameters in different models (Gioia et al., 2016; He et al., 2021; Medina et al., 2021). During the sensitivity analysis, the value of each parameter is changed when other parameters are kept constant in their default

value. This is a simple and commonly adopted way of sensitivity analysis (Zieher et al., 2017). Larger ranges of values than parameter datasets are used for sensitivity analysis to show the response of factor of safety to parameters' variation. Using a larger data range than a dataset in sensitivity analysis is important to understand possible limiting conditions to parameter sensitivity. For example, greater hydraulic conductivity leads to more infiltration rate in TRIGRS, but the rainfall intensity limits it.

Required input parameters, their respective ranges and default values, and available data are listed in Table 3.1. In the material properties (Ks, $c', \emptyset', \gamma, \eta$) are reported by (Uyeturk et al., 2020). Gardner's (1958) SWCC parameters are determined by fitting the data provided by Uyeturk (2019) up to suction head of 50 kPa (Figure 3.8 and Table 3.3). The range of soil depth is determined considering the depth of landslide data (90 % of failures are shallower than 2 m). The default value is selected as the mean value of failure depths. In the literature, hydraulic diffusivity is used as 5 to 500 times of hydraulic conductivity (Baum et al., 2005; Liu & Wu, 2008; Park et al., 2013). The default value of these parameters is taken as 100Ks, which is the most widely assumed value (Luo et al., 2021; Salciarini et al., 2008; Tran et al., 2018). Curve number is determined based on the land cover in the area (USDA, 1986).

The steady-state infiltration rate and antecedent recharge are used to compute pore pressure conditions at the onset of the event rainfall. However, their missions differ, and they rely on different hydrological assumptions. While the former is employed for determining vertical pore pressure change, the latter is adopted to find out water table depth in slope-parallel flow regime. However, both parameters depend on antecedent rainfall conditions, evapotranspiration, and the hydraulic properties of soil. Mean precipitation two weeks and three days before the event rainfall is measured as 0.36 and 2.09 mm/day, respectively.

Table 3.2: Required input parameters, available data, and the data range considered in the sensitivity analysis (S.A: Sensitivity Analysis, * indicates for which software the parameter is required).

	FSLAM	TRIGRS	SCOOPS 3D	Range in Sensitivity Analysis	Range in Available data	Default Value in S.A
Soil Depth z (m)	*	*	*	0.5/1/2/3/5	0.5-2	1
Intial depth of water table, d_{wi} (m)		*		0.25z/0.5z/0.75z/1z	No Data	1
Steady state infiltration, Izlt		*		0/0.1Ks	No Data	0
Antecedent recharge, Pa (mm/day)	*			0.2	No Data	0.2
Soil Cohesion, c_s' (kPa)	*	*	*	Considered in total cohesion	3.4-7.6	0
Total Cohesion, $c_s' + c_r'$ (kPa)	*	*	*	0/3/10/20/30/50	No data	0
Friction angle, $ø'$ (degree)	*	*	*	20/25/30/35/40	31.1-38.0	35
Saturated hydraulic conductivity, Ks (m/s)	*	*		$10^{-10}/10^{-8}/10^{-6}/10^{-4}$	$1.1*10^{-6}/1.5*10^{-7}$	10^{-6}
Saturated hydraulic diffusivity, D_0 (Ks)		*		5/25/100/250/500	No Data	100 Ks
Saturated volumetric water content, $Θ_s$		*		0.4/0.6/0.8	0.608-0.485	0.519
Residual volumetric water content, $Θ_r$		*		0.1/0.2/0.4/	0.318-0.236	0.294
Water storage capacity, $Θ_s - Θ_r$		*		0.1/0.2/0.3	0.298-0.195	0.225
Gardner's SWRC exponent, $α$ (1/m)		*		0.6/1.13/1.5/2.5/3.5/4.5	3.76-0.66	1.13

Unit weight of soil γ_{soil} (kN/m³)	*	*	*	17.66/19.62/21.58	15.4-18.83	17
Fillable Porosity, n*	*			0.1/0.2/0.225/0.25 /0.3/0.35/0.4	0.38-0.66	0.225
Slope Angle				20/25/30/35/40	20-50	25
Curve number, CN	*			30/50/70/100	96-58	70
Total event rainfall, Pe (mm)	*	*		82.6	82.6	82.6
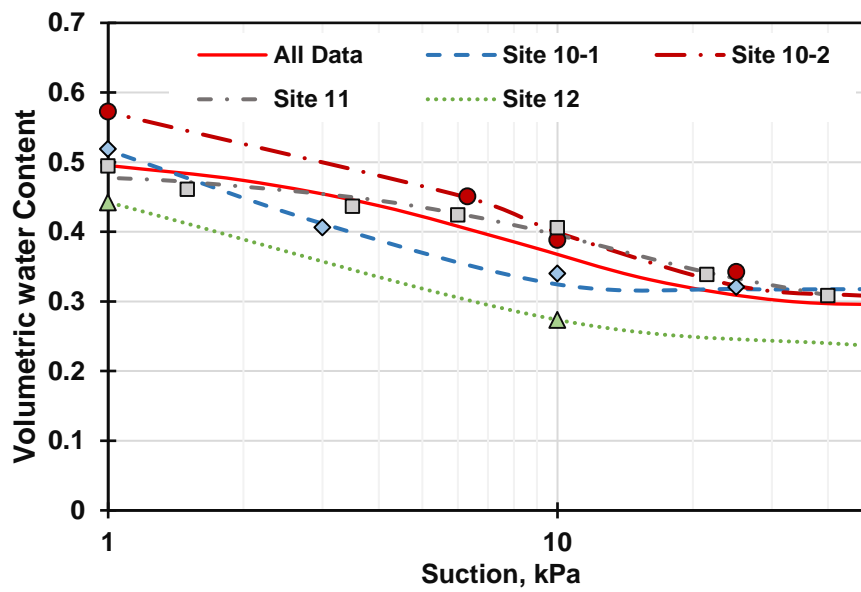
Figure 3.8. Gardner's (1958) SWRC curves of available data (site numbers correspond to landslides reported in Uyeturk et al. (2020)).

Table 3.3 Gardner's (1958) SWRC parameters of available data.

Site Number	θ_s	θ_r	α (1/m)
10-1	0.608	0.318	3.76
10-2	0.605	0.307	1.17
11	0.490	0.295	0.66
12	0.485	0.236	1.89
All data	0.519	0.295	1.13

48

3.3.1.1 Digital elevation model (DEM)

The digital elevation model should belong to the date before the landslide episode. Due to the high-resolution DEM source scarcity 1/25000 scale, the 10 m interval contour line map provided by the General Directorate of Mapping of Turkey is used for DEM production. Since the higher resolution is not compatible with these maps, 10 m resolution was selected for FSLAM and TRIGRS. One advantage of this resolution is its high length to depth ratio, which is compatible with the infinite slope assumption (Hutchinson, 1994; Milledge et al., 2012). On the other hand, as discussed in section 4.1.3, most of the landslides are smaller than the resolution of DEM. The drawback of this resolution is also taken into account in performance analysis. The second disadvantage of this resolution is being insufficient for adequate computation of factor of safety in SCOOPS3D. Therefore, SCOOPS3D analysis was performed on 1 m resolution DEM produced from the same contour map. To be consistent in the comparison of TRIGRS, FSLAM, and SCOOPS3D same DEM elevation model is used in a small area (SCOOPS3D is applied only in a small portion of the study area).

3.3.1.2 Input rainfall

As indicated in Figure 3.1, the precipitation amount is very low until September 23, and low precipitation is measured between Sept. 23-27. After Sept. 27, intense rainfall was observed until Sept. 29. The majority of landslides are reported in this period. Therefore, the precipitation in this period is considered as triggering event. The cumulative amount of rainfall is sufficient as an input parameter for FSLAM, but TRIGRS needs hourly-based input. The input rainfall used in TRIGRS computation is shown in Figure 3.9. The Red dashed line shows the most expected value of Ks, which is a limit for infiltration rate (Baum et al., 2010).
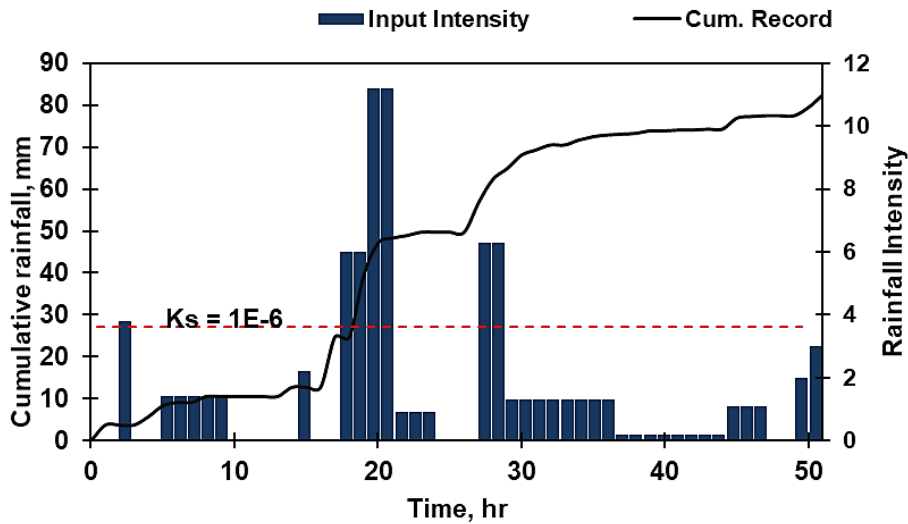
Figure 3.9. Input rainfall for TRIGRS analysis.

3.3.2 Comparison of FSLAM and TRIGRS hydrological model

An initial sensitivity analysis is conducted to assess the consequence of these different assumptions of the hydrological model of FSLAM and TRIGRS. The water table rise due to event rainfall in two models is compared with the parameters' default values in Table 3.2.

In the FSLAM models, the calibration term, n^{*} is taken equal to water storage capacity $(\Theta_s - \Theta_r)$.

Although total infiltrated water computed by FSLAM is more than TRIGRS, water table rise of FSLAM model is less than water table rise computation of TRIGRS at the time when rainfall ceased (Table 3.4).

Table 3.4 Comparison of total infiltration and water table rise computations of TRIGRS and FSLAM

	TRIGRS	FSLAM
Total Infiltration (mm), q_e	57.0	62.24
Total Basal Flux (mm), q_u	33.5	
Total excess Flux (mm), q_u-q_z	33.5	
Water table Rise (m), h	0.666	0.276

The reason for this difference is illustrated in Figure 3.10. Since TRIGRS can model variable water content with depth, fillable pore volume decreases as the water table approaches.

Accordingly, a higher water table rise is observed. Furthermore, water table rise in TRIGRS depends on both unsaturated layer thickness and soil types. If TRIGRS analysis continues after rainfall ceases water table continues to rise. If TRIGRS analysis continues until all infiltrated water reaches the saturated layer, the asymptotic value of the water table rise is obtained. This asymptotic value is independent of unsaturated layer thickness (Figure 3.10). The asymptotic value of TRIGRS and FSLAM converges when alpha increases. Because the desaturation rate of the soil increases as alpha increases, that means presence of a higher fillable volume at the beginning of the analysis. This condition represents the behavior of granular soils.

Comparison between FSLAM and TRIGRS infiltration models implies that the "porosity" term used to calculate water table (Medina et al., 2021) rise during event rainfall in FSLAM can be considered a calibration term. The closest physical meaning of this term is;

$$n^* \geq n \times (1 - Sr) \tag{3.4}$$

Where n is porosity and Sr is the average degree of saturation through the depth before the event rainfall. Sr depends on both soil type and antecedent rainfall condition. The same approach is also used in the SLIP model (Montrasio & Valentino, 2008). Although asymptotic water table rise computation of TRIGRS is more conservative and stability of a slope may decrease after rainfall ceases, the 1D infiltration assumption of TRIGRS is not valid until the asymptotic case is reached. The lateral flow becomes more significant in time (Baum, Savage, et al., 2008). With the same perspective, n^* should be greater than the right side of the Eqn. 3.4. If the

soil is coarse-grained or has macro-pores, the difference will be more negligible (Schilirò et al., 2016).
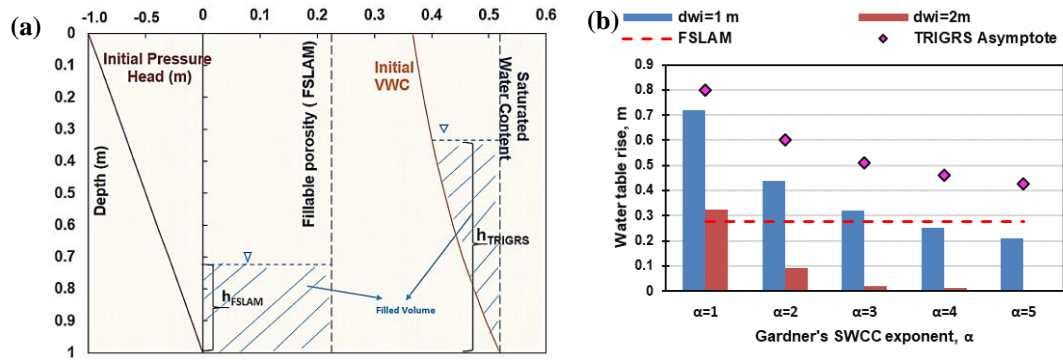
Figure 3.10. Comparison of infiltration model of FSLAM and TRIGRS. (a) Conceptual illustration of water table rise. (b) Water table rise computation of TRIGRS and FSLAM in different initial water table depth and different alpha conditions.

CHAPTER 4

RESULTS AND DISCUSSIONS

4.1 Landslide inventory

In this study, the source area of 1025 landslides was determined. Although Cömert et al. (2019) reported 1057 landslides, some reported landslides were found to be very shallow surface erosion. In addition, it was understood that some landslides that were thought to be separate landslides were, in fact, parts of a single landslide which was not clearly visible due to the leaves/shades of the trees. However, some new landslides have also been detected. The number of source areas mapped and the methods used for depth calculation are given in Table 4.1.

Table 4.1 Summary of the number of landslides and their depth calculation methods.

Depth could not be measured	Shallower than 0.4 m	Deeper than 0.4 m		
		771		
199	55	X-section method	MWP method	Both methods
		467	84	220

Table 4.2 summarizes the statistics of the morphometric properties of the source areas. The depth in Table 4.2 was calculated by the X-section method and volume by half ellipsoid method. Three landslides are classified as deep-seated. Because their thicknesses are measured as 5 m, 4.98 m, and 4.87 m, except for these three landslides, the thickness of all other 826 landslides is less than 3.6 m. The average landslide depth, length, and width are determined as 1.05 m, 14.3 m, and 8.5 m,

53

respectively (Table 4.2). The average slope angle is 35.9 degrees, and the elevation of these landslides varies between 463 and 985.5 m.

Table 4.2 Summary of the statistical properties of morphometric features of landslides

	Mean	Max.	Min.	Standard deviation
Depth, D (m)	1.05	6.6	0.1	0.63
Thickness, t (m)	0.89	5.5	0.03	0.64
Length, L (m)	14.3	79.7	1	12.2
Width, w (m)	8.5	49.1	1.6	5.08
L_H / D	17.0	290.0	1.5	19.5
w / D	10.6	99.3	1.7	9.6
Area (m^2)	146.6	1775.5	2.3	200.0
Volume (m^3)	165.7	5366.8	0.4	421
Elevation (m)	666.4	985.5	463	
Slope Height (m)	10.9	316.5	0.7	13.0
Slope Angle (deg.)	35.9	67	15.6	7.7

4.1.1 Slope types

The failures are observed in three different slope types; hillslopes, cut slopes, and riverbanks. Their possible different failure mechanisms entail this separation. Failures in cut slopes and river banks might be initiated by toe weakening, whereas hillslope failures are related to pore pressure change of the entire pitch (Zieher et al., 2017). While shallow hillslope failures are expected to be translational (Haneberg,

2004), cut slopes are not. Consequently, slope types of the failures should be taken into account during susceptibility assessment. For example, cut slope and riverbank failures are steeper than hillslopes (Figure 4.1(b)). More than 85% of the landslides in the inventory are hillslope type (Figure 4.1(a)).
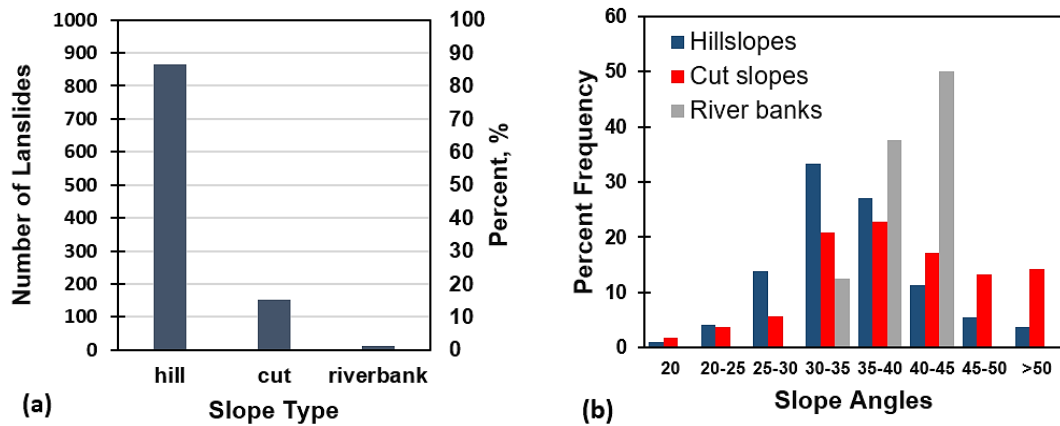
Figure 4.1. (a) Types of slopes (b) Slope angle of failures in in different slope types.

4.1.2 Depth of Landslides

4.1.2.1 Comparison of different depth calculation methods

The typical tea plantation height is assumed as 0.4 meters. Since depths are calculated using DSM, 0.4 meters is deducted from measured failure depth in tea planted areas. Accordingly, landslides shallower than 0.4 meters are considered as superficial damages of tea plants, which might also result from surface runoff (Table 4.1). Consequently, landslides' minimum depth and thickness are calculated as 0.1 m and 0.03 m (Table 4.2). These values might be lower than the precision of the applied model, but presenting results without elimination is preferred.

As stated in the methodology section, MWP, OWP, and X-section methods are employed to calculate failure depth. The maximum and average depth of failures was calculated by the X-section method. On 220 landslides, all three methods are used

and compared (Figure 4.2a). The respective mean depths calculated by OWP, MWP, and X-section methods is 2.08, 0.99, and 1.00 m. This comparison shows overestimation of landslide depth by OWP method as compared to other two methods. Furthermore, the mean error between the mean depth calculated by the X-section method and MWP is small; on the other hand, their correlation is low (Figure 4.2b).
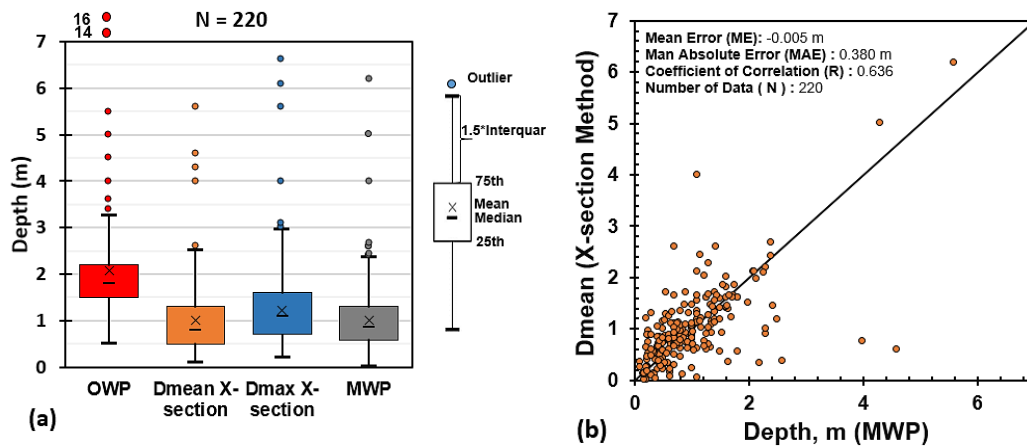
Figure 4.2. Depth of landslides, (a) comparison of 3 methods, (b) comparison of MWP and X-section methods.

4.1.2.2 Statistical distribution of depth of landslides

Only the X-section method (Dmax) is used to derive the failure's statistical distribution. Since 98% of failures are shallower than 3 meters, greater values are excluded. Consequently, landslide depth's mean and standard deviation are calculated as 1.05 m and 0.63 m, respectively.
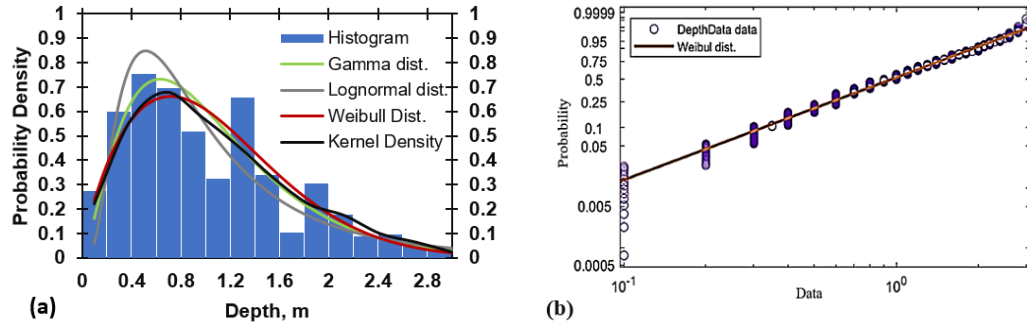
Figure 4.3. a) Probability density plot of landslide depth, (b) Probability plot of Weibull distribution.

Gamma, lognormal and Weibull distributions are tested because of the asymmetrical distribution of failure depths. The fitness of the distributions is compared with probability plots (Figure 4.3b). Two parameters of Weibull distribution ended up with the best performance (a=1.1871, b= 1.7278 in Eq. 4.1). The probability density plots of tested distributions are shown in Figure 4.3a. The same distribution represents a spatial variation of soil depth by Burton et al. (1998) in their study area.

$$P(x \backslash a, b) = \frac{b}{a} \left(\frac{x}{a}\right)^{b-1} e^{-\left(\frac{a}{b}\right)^b} \qquad \text{(Eq. 4.1)}$$

4.1.2.3   Spatial distribution of depth of landslides

When soil thickness (which is one of the input parameters in common physically-based susceptibility models) obtained by direct measurements in the field is not available the depth of landslides can be utilized for this purpose (Frattini et al., 2004; Zieher et al., 2017). The simple soil thickness prediction methods are examined for the study area. Some of the correlations to estimate soil thickness utilize linear slope gradient (Saulnier et al., 1997), exponential slope angle (Salciarini et al., 2006), linear elevation (Saulnier et al. 1997), topographic wetness index (TWI) (Lee & Ho, 2009), and topographical position-elevation-slope combined models (Zizioli et al., 2013). Additionally, the kriging spatial interpolation technique was also tested. 70% of data is used for training and others are used for testing (a total of 687 landslides).

When a mean square error (MSE) between prediction and test data is compared, MSE is observed to be greater than the variance of test data, meaning that the performance of the models is less than the average of the data (Lanni et al., 2012). Consequently, landslide depths do not give plausible results with these simple models to estimate soil thickness. The cumulative distribution of all models and landslide depths are shown in Figure 4.4.
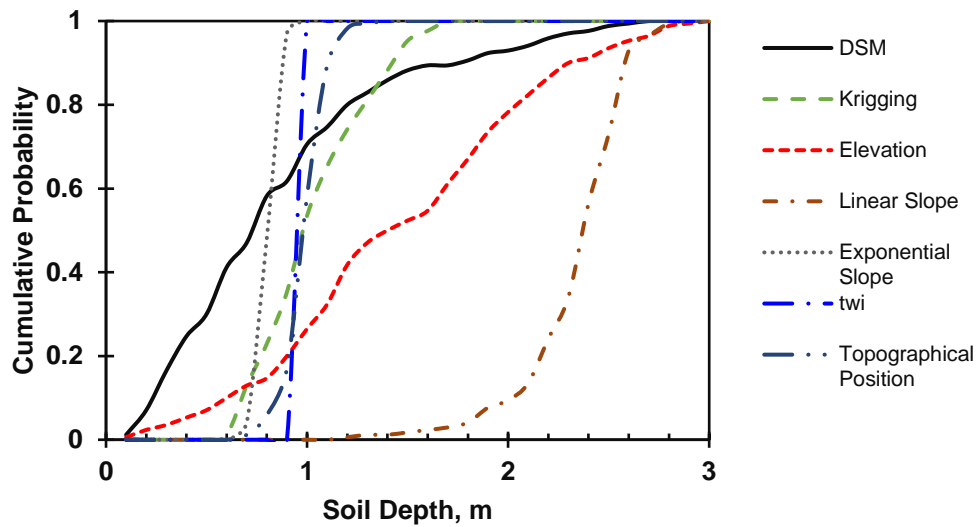
Figure 4.4. Comparison of soil thickness models and landslide depths from DSM

4.1.3   Other dimensions of landslides

The cumulative distribution of length and width of landslides indicates that these failures are very small (Figure 4.5). Length of 48.3 percent of flows and width of 70.3 percent of them are smaller than 10 m, which is the resolution of the DEM used in susceptibility analysis (Fig. 4.5). Figure 4.5 highlights the importance of the resolution of DEM and its compatibility with the dimensions of the landslides in the inventory. When a cell size of 10 m is used in susceptibility analyses, some percent of landslides in the inventory will not be captured by the analyses, since they are smaller than 10 m.
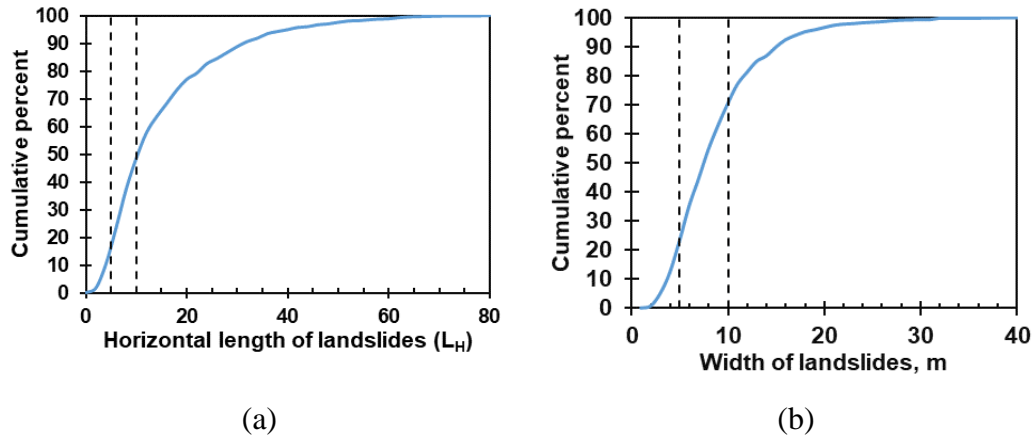
Figure 4.5. Comparison of the compatibility of 5 m and 10 m resolution DEM to (a) Cumulative distribution of length of landslides (b) Cumulative distribution of width of landslides.

4.1.4   Classification of failures for modeling approaches

In this section, the earth flows are categorized according to dimension ratio thresholds reported by both Skempton & Hutchinson (1969) and Milledge et al. (2012). In Table 4.3 L/t ratio thresholds for translational, compound, and rotational failures are adopted as 10, 6.67, and 3, respectively. As for the validity of the infinite slope assumption, L_H/D ratios of 18 and 25 are thresholds respective to 10%, and 5% error, independent of the cohesion of the soil. L_H/D ratio equal to 10 is considered as an acceptable threshold for this area, considering low cohesion values of similar soils in Rize (Uyeturk et al., 2020). L_H/D ratio larger than 10, means that the slope can be modeled with infinite-slope approach. The cumulative distribution of hillslope failures according to both criteria is shown in Figure 4.6a, indicating that some percent of landslides in the inventory cannot be classified as infinite-slope type.

Table 4.3 Percent of landslides according to thresholds for "translational landslides" and "infinite-slope" assumptions.

	Translational Landslide Criteria				Infinite-Slope Criteria		
	L/t≤ 10	6.67<L/t<10	3≤L/t≤6.67	L/t < 3	L_H/D>10	L_H/D >18	L_H/D >25
Hill Slope, %	82.4	10.6	6.2	0.8	63.7	34.4	23.9
Others, %	63.3	17.5	17.5	1.7	33.1	14.5	5.6
Total, %	79.4	11.7	8.0	0.9	58.8	31.2	21.0

As widely accepted in the literature (Haneberg 2004), shallow landslides on natural hillslopes have a high L/t ratio. On the other hand, failures in cut slopes and river banks are shorter compared with their depth.

The chart provided by (Hutchinson, 1994) was adopted to decide whether lateral boundaries affect stability, i.e. whether 2-dimensional or 3-dimensional analyses should be done. D/W ratio of 0.13 is selected as a threshold for this purpose considering fully saturated and normally consolidated conditions. Accordingly, 55.8 % of hillslopes and 43.5 % of cut slope-riverbank failures are above this threshold (Figure 4.6b).

(a)   **(b)**
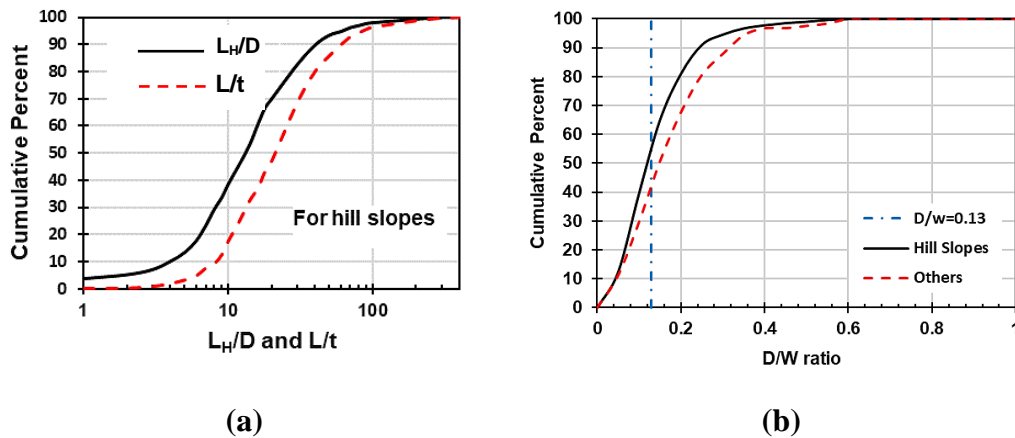
Figure 4.6. (a) Cumulative distribution of natural hillslope failures according to both translational failure and infinite slope criteria. (b) Cumulative distribution of depth/width ratio.

Figure 4.7. Landslides in the study area with appropriate modeling approaches

From the combination of proposals made by Miledge et al. (2012) and Hutchinson (1994), 294 out of 652 (45%) of failures on hillslopes and 30 of 119 (24.2%) of failures on other slopes are concluded to be suitable for infinite slope assumption (Figure 4.7). This conclusion highlights different morphology of failures on hillslopes and cut slopes- river banks.

The locations of failures with suitable stability assumptions are shown in Figure 4.8.
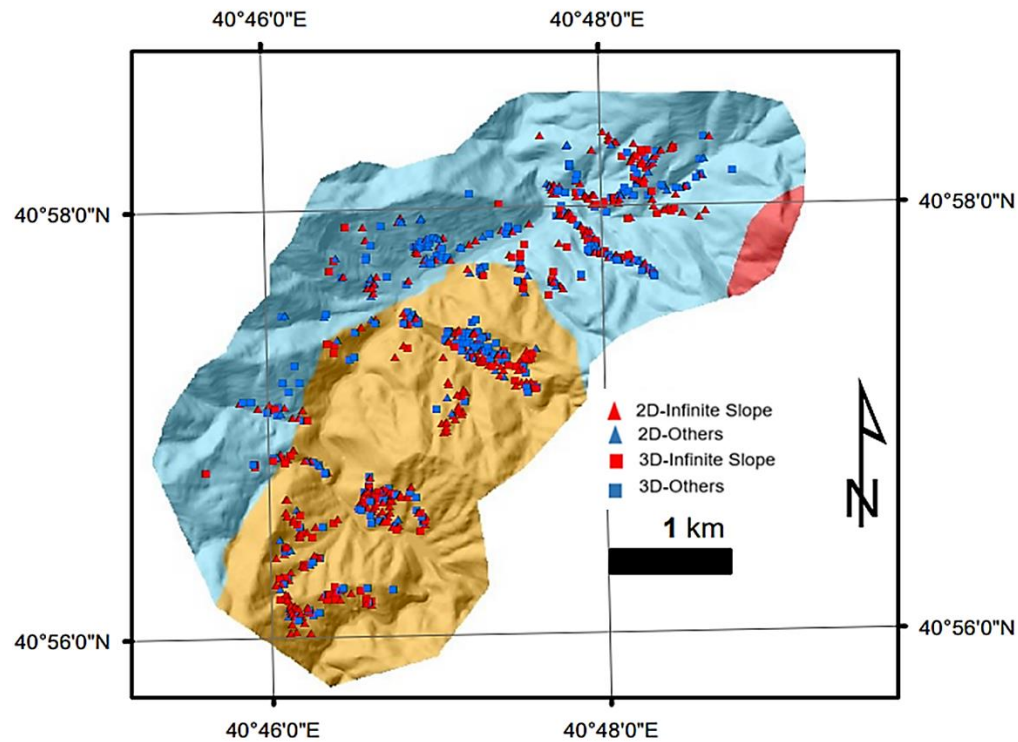
Figure 4.8. The location of failures according to their suitable assumptions.

4.1.5   Failure types

Considering the available DEM resolution (10 m), slope types, and morphology of landslides, all failures are grouped into four types explained below (Figure 3.1).

(i) **Type 1:** The hillslope failures conforming infinite slope assumptions and having greater dimensions than 10 m are grouped under this type. These failures are the most compatible type with the assumptions of models based on infinite slope..

(ii) **Type 2:** The hillslope failures with dimensions greater than 10 m and unsuitable for infinite slope assumptions.

(iii) **Type 3:** The cut slope and riverbank failures with dimensions greater than 10 m.

62

(iv)Types 4: All failures with dimensions smaller than 10 m.
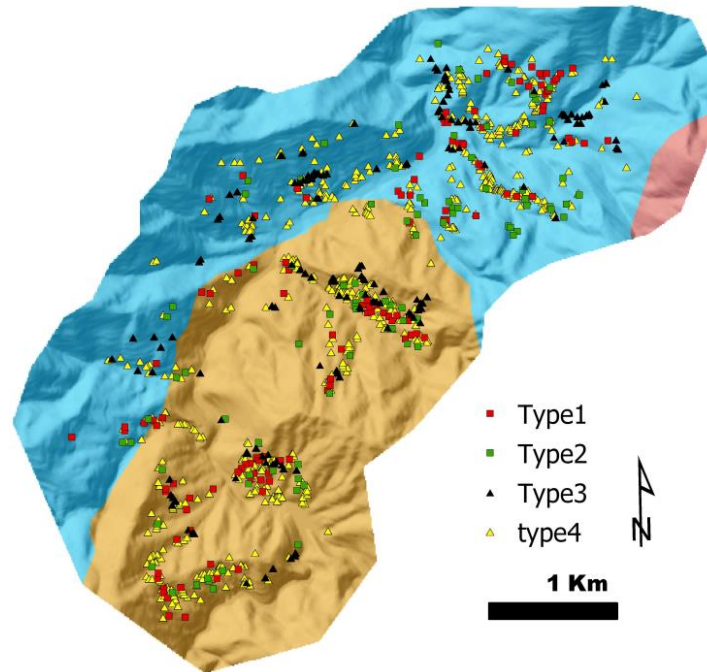
Figure 4.9. Location of different types of failures.

4.1.6   Landslide sizes and scaling properties

Landslide sizes and their distributions are one of the main parameters of hazard assessment. The interrelations of these features assist in estimating one metric from the others. Depth, area, volume are the main metrics used for this purpose (Larsen et al., 2010; Malamud et al., 2004; Stark & Hovius, 2001). Frequency distribution of landslide sizes is used for estimating their probability of occurrence in a particular field (Ardizzone et al., 2002). The probability of occurrence of landslides sizes is reported decreasing after a roll-over point which is the most expected size. Inverse-Gamma distribution is the most widely applied model to describe this relation

(Malamud et al., 2004). Proposed inverse-gamma distribution by Malamud et al. (2004) ;

$$p(A_L; p, a, s) = \frac{1}{a\Gamma(p)} \left[\frac{a}{A_L - s}\right]^{p+1} \exp\left[-\frac{a}{A_L - s}\right] \qquad \text{(Eq 1.2)}$$

Where; A_L is the area of individual landslides, (p+1) power-law exponent, a is the maximum observed area, s is the power exponent of small landslides.

Kernel density distribution of landslide source areas and maximum likelihood estimation of inverse-gamma distribution is shown in Figure 4.10.

Model parameters p, a, and s are calculated as 1.4739, 1.05×10^{-4} $km^{2,}$ and 1.45×10^{-5} km^2. The relation between source areas and the depth of landslides (D_{max}) is shown in figure Figure 4.11. Their relations are in the same trend as soil landslides reported by Larsen et al. (2010).

As stated in section 3.2.3, the volumes of the landslides are calculated by half ellipsoid and prism methods. The estimated volume by prism method overestimates the volume by a factor of 1.23 as compared to the prism method (Figure 4.12a). Considering the shape of the failure surface, the elipsoid assumption seems to be more suitable for volume calculation (Figure 4.13). Overestimation of volume by the prism method was also stated by Guzetti et al. (2009).
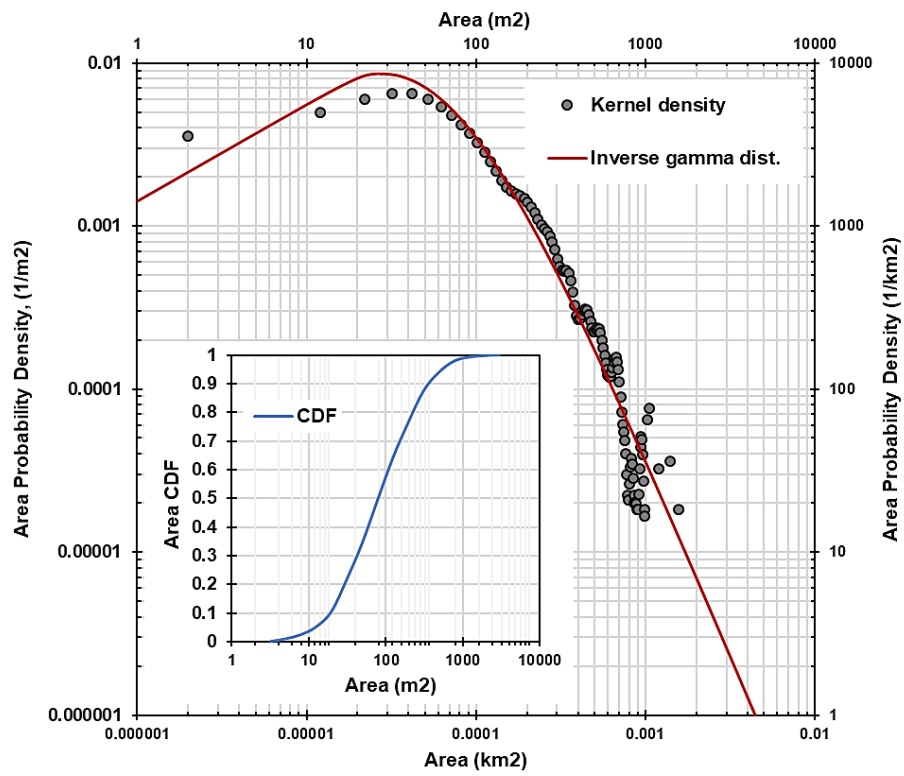
Figure 4.10. Probability density distribution of source areas.
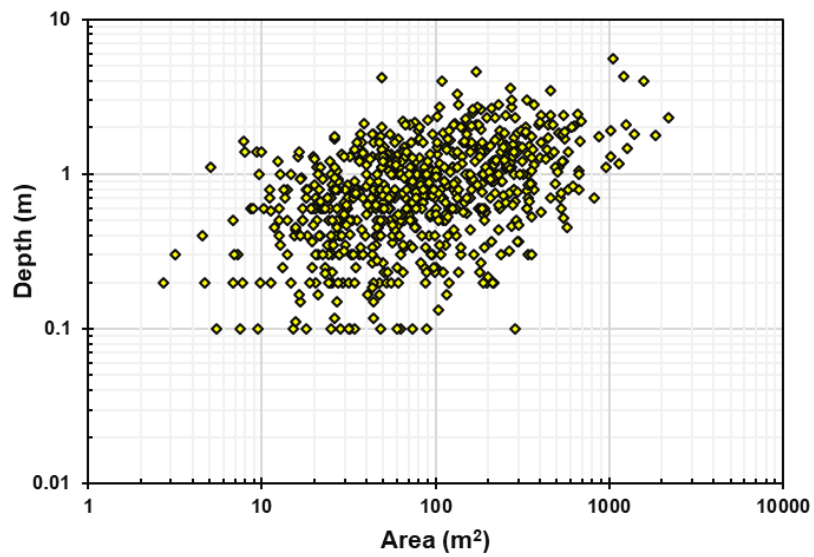
Figure 4.11. Relation between area and depth of landslides' sources.
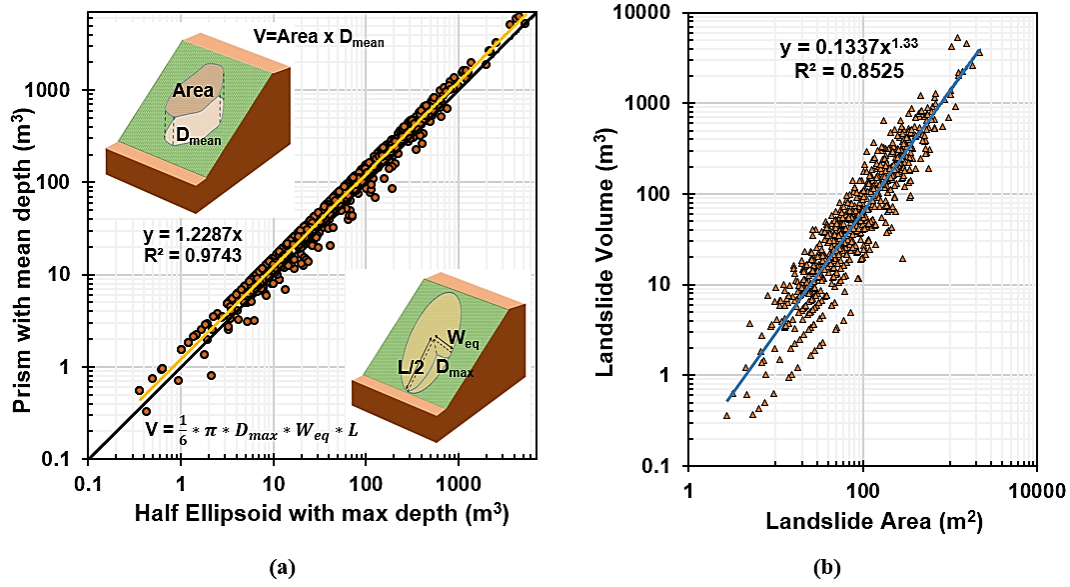
Figure 4.12. (a) Comparison of ellipsoidal and prismatic volume calculation (b) Landslide area vs. landslide volume.

Interrelation between the area and volume of landslides is suggested as $V=\varepsilon A^{\alpha}$. This relation is useful for volume estimation in areas where direct measurement is impossible. Empirical relation is evaluated as $V=0.134A^{1.33}$ (Figure 4.12b) in the study area. Larsen et al. (2010) reported that the scaling exponent of soil landslides is between 1.1-1.3, which agrees with this study's outcome.
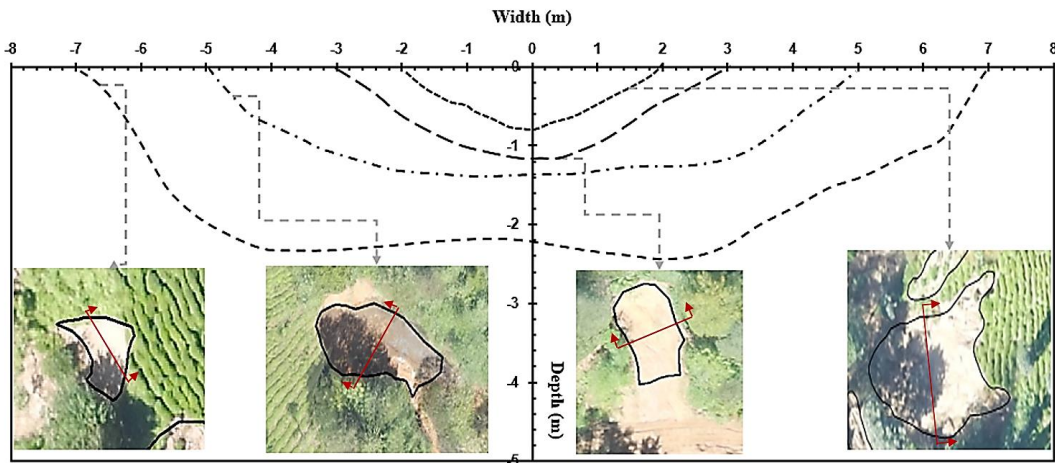
Figure 4.13. Cross-section of randomly selected landslide source areas.

Lastly, the total volume was calculated as 1.13809×10^5 m^3. Considering this is an event inventory and it is expected to be once a year, the mobilization rate is calculated as 7.7 mm/year for a 14.83 km^2 area.

Different metrics are utilized in the literature to decide event magnitude. For this purpose, total number-based (Malamud et al. 2004) and total volume-based (Guzzetti et al., 2009) proposals were adopted. The event magnitude of this episode is calculated as 3 and 5 according to Malamud et al. (2004) and Guzetti et al. (2009) proposals, respectively.

4.1.7 Relation between landslides and conditioning factors

This section examines the conditioning factors of landslides. Generally, these factors are a matter of statistical studies. Regarding statistical studies, many factors can be examined, such as vegetation, distance to roads, distance to streams, geology, topographical factors, and hydrology-related parameters (topographic wetness, stream power, etc.). These influential factors differ, and their contribution differs in different areas. Some of these factors, such as slope gradient, soil thickness, soil strength parameters, and hydraulic parameters, are also the input of physically-based models. On the other hand, some of them (geology, elevation, land cover, etc.) are indirectly included, affecting the input parameters. Knowing the contribution of these factors can be adopted to increase the performance of physically-based models.

Mean slope angle, elevation, land cover, geology, slope curvature, and slope aspect classes are taken into account for this landslide inventory, since these parameters are frequently adopted in statistical susceptibility studies in Rize (Akgun et al., 2008; Dağ et al., 2020; Reis et al., 2008; Yalcin, 2008; Yalcin & Bulut, 2007). The percent frequency of observed landslides is calculated based on the area and the number of landslides. The average elevation, curvature, and slope aspect are computed in the landslide polygon while considering the number of landslides. On the other hand, the area-based classification of elevation and geology, cell counts in ArcGIS are

considered. In contrast, the area of individual landslides in that class is calculated for the curvature, aspect, and land cover. The effect of each conditioning factor is represented by the likelihood ratio (eq 4.3) (Akgun et al., 2008).

$$Likelihood\ Ratio\ = \frac{\%\ Frequency\ of\ landslides}{\%\ Frequency\ of\ study\ area} \qquad (Eq\ 4.3)$$

(a)

(b)

(c)

68
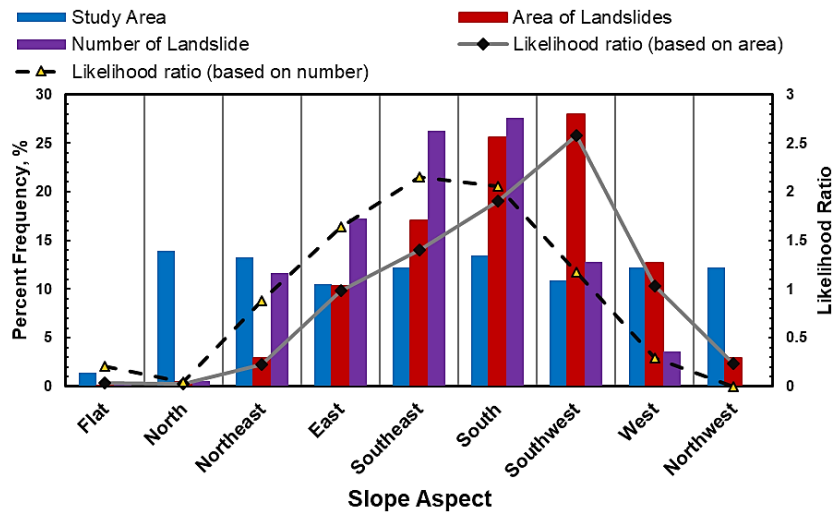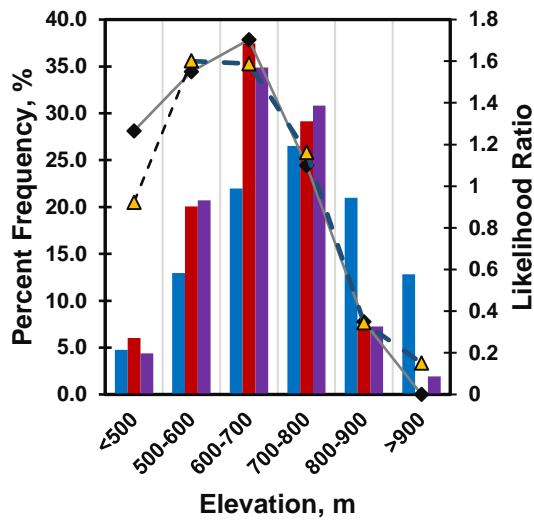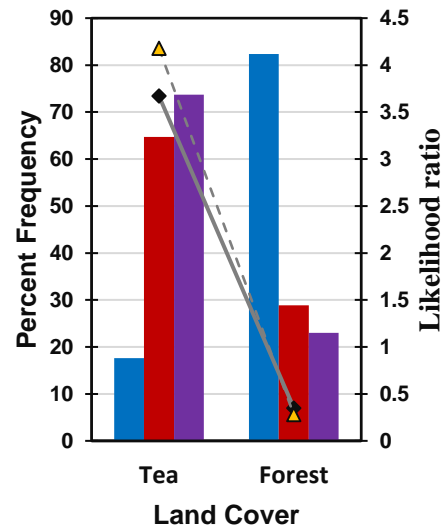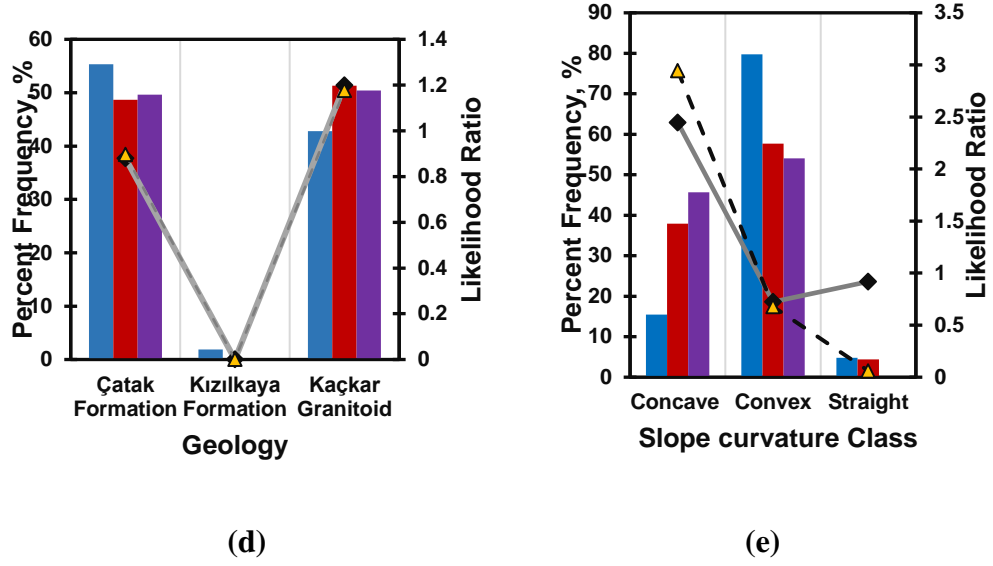
Figure 4.14. Effect of conditioning factors (a) slope aspect, (b) elevation, (c) land cover (d) geology (e) slope curvature class.

Slopes facing south, south-east, and south-west directions seem to be more likely to fail (Figure 4.14a), which is a agrees with with the conclusions of Akgun et al (2008) in other landslide sites in Rize. Nevertheless, different critical aspects were reported by various studies in other parts of Rize province (Yalcin and Bulut 2007; Yalcin 2008). Besides, larger landslides are observed in the southwest direction.

The vegetation seems to be one of the major affecting factors as was also highlighted in other studies in Rize (Yalcin and Bulut 2007; Akgun et al. 2008; Yalcin 2008; Dag and Bulut 2012; Dağ et al. 2020) (Figure 4.14c). The physical influence of the presence of trees contributes to stability by detaining water on canopies and by providing root cohesion. On the other hand, tree surcharge has an inverse impact (Kim et al., 2013). The overall effect of trees increases the stability in the study area.

As for the geologic formations, the likelihood of failures in Kaçkar Granitoid is slightly higher than in the Çatak formation(Figure 4.14d). Kızılkaya formation is not comparable to others since it covers minimal areas.

It is worth noting that the likelihood ratio ignores interrelation between conditioning factors (Akgün et al., 2008). For example, dramatic decay in landslide areas after

800 m elevations might be related to a reduction in chemical weathering or decreased tea-planted areas. Consequently, more effort is needed to use this contribution in statistical models.

4.2   Physically-based modeling

4.2.1   Results of sensitivity analysis

Sensitivity analysis is conducted for (i) understanding the importance of each parameter (ii) selecting the parameter set to calibrate, and (iii) determining the impact of each critical parameter on the factor of safety in the available data set (Gioia et al., 2016; He et al., 2021; Medina et al., 2021). During the sensitivity analysis, the value of each parameter was changed when other parameters were kept constant in their default value. This is a simple and commonly adopted sensitivity analysis (Zieher et al., 2017). Larger values than the parameter dataset were used for sensitivity analysis to show the response of factors of safety to parameters' variation (Table 3.2).

In order to represent sensitivity, two indicators are used. These are percent changes in factor of safety;

$$\nabla FS, \% = \frac{FS_i - FS_{default}}{FS_{default}} * 100 \tag{4.4}$$

and ,

$$\text{Relative change of parameter} = \frac{P_i - P_{default}}{P_{max} - P_{min}} \tag{4.5}$$
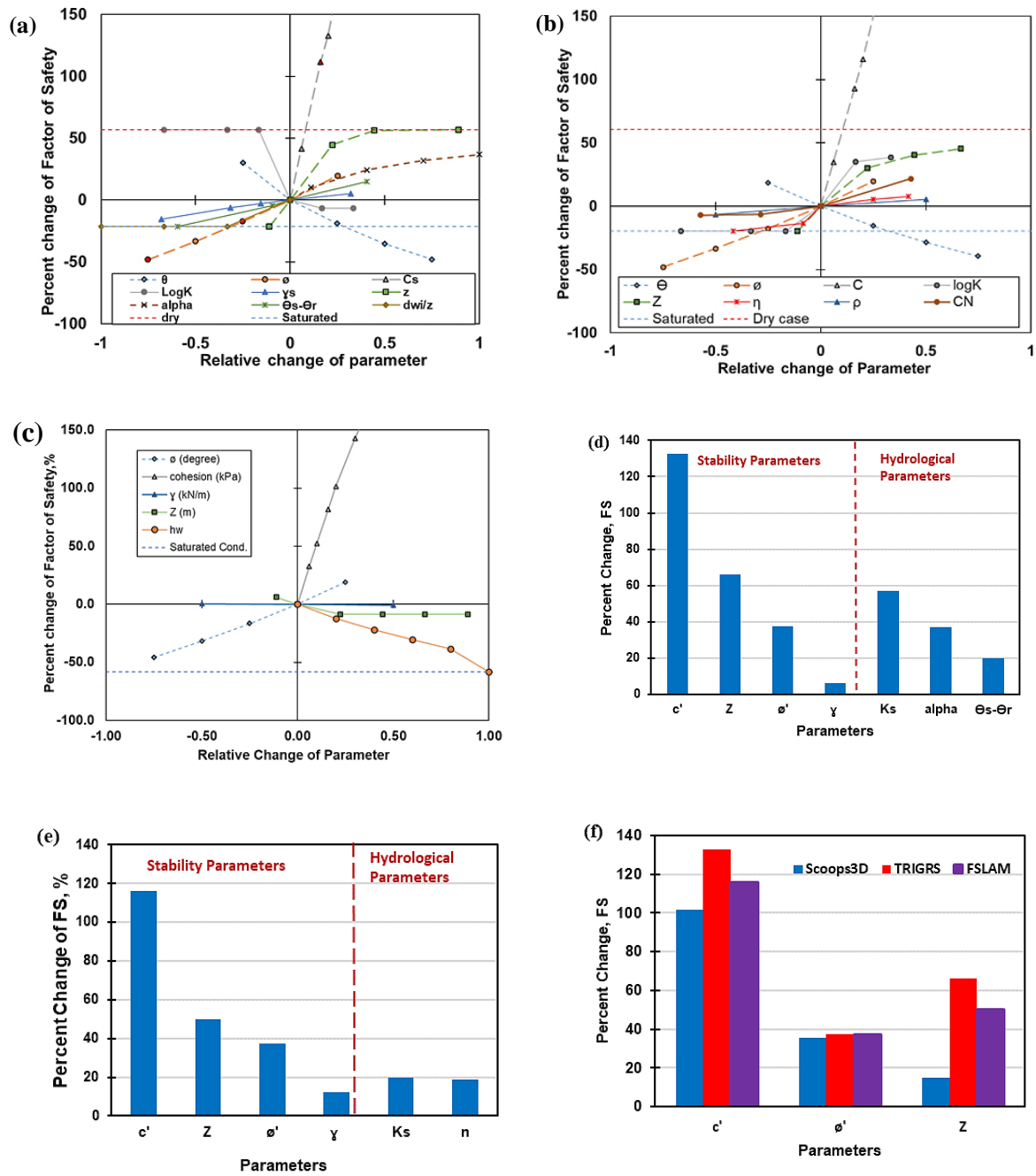
Figure 4.15. Sensitivity of input parameters. (a) TRIGRS (b) FSLAM (c) Scoops3D (d) Effect of variability of TRIGRS's important inputs in available data range (e) Impact of FSLAM's essential inputs variability in the available data range (f) Comparison of the effect of stability parameters in the available data range.

While default rainfall condition is used as specified in Table 3.2 for FSLAM and TRIGRS, the dry state is considered in SCOOPS3D. Then a change of a factor of safety with different water table depths is examined. The same unit weight is used under and above the water table.

Sensitivity plots of TRIGRS, FSLAM, and SCOOPS3D are shown in Figure 4.15a, Figure 4.15b, Figure 4.15c. The sensitivity of steady-state background infiltration and saturated hydraulic diffusivity was also tested in TRIGRS. Since their effects are insignificant compared to others, they are not included in sensitivity plots.

For the TRIGRS and FSLAM cohesion, friction angle, soil depth, and slope angle (in the following part of the thesis, these parameters are called stability parameters) are the most critical parameters. Because these parameters are directly included in the infinite-slope factor of safety calculation, therefore, these three parameters determine the possible minimum (saturated condition) and maximum (dry state for sensitivity analysis) factors of safeties (are shown in figures with dashed lines). Variation in hydraulic parameters changes factors of safety within these two extreme conditions (dry and saturated). Therefore the significance of stability ($c, \theta, \emptyset, z, \gamma$) and hydraulic parameters should be considered separately. Change of FS resulted by variation of inputs in the available dataset is shown in Figure 4.15d and Figure 4.15e for TRIGRS and FSLAM. Among the stability parameters, cohesion is the most significant parameter for all three models. However, it should be noted that the results of sensitivity analysis bias to the default value of the input parameters. For example, stability of the soil column increases with increasing soil thickness in Figure 4.15a-b since the default value of cohesion is zero. Increasing soil thickness decreases the inverse effect of water table rise instability.

On the other hand, if the default value of cohesion were higher, soil depth would have an inverse effect on the factor of safety. Furthermore, the sensitivity of results to soil thickness would be higher. Consequently, default values in sensitivity analysis should be the expected (representative) values in the field.

Soil thickness is less significant in SCOOPS3D (Figure 4.15f) than in other models. This difference is that the depth of bedrock coincides with failure surface in FSLAM and TRIGRS, whereas in SCOOPS3D, the depth of critical surface depends on slope height, cohesion, friction angle, and unit weight of soil (Reid et al., 2015). Soil depth is only a lower limit for failure surface.

Among the TRIGRS' hydraulic parameters, saturated hydraulic conductivity is the most important one as it changes both the amount of infiltration and the response rate of pore pressure to infiltration. The factor of safety is inversely affected by increasing hydraulic conductivity until all rainfall infiltrates. After this point, the change of Ks does not affect the FS. On the other hand, hydraulic conductivity is considered in the lateral direction in the FSLAM model. Therefore, it positively affects the stability of the slope. FS safety decreases as Ks reduces until the soil column becomes saturated. It is worth noting that Ks and antecedent recharge is assumed to be independent in the sensitivity analysis. However, steady-state slope-parallel flow is valid because rainfall duration is long, and rainfall intensity compared with Ks is very small (Iverson, 2000).

4.2.2   Calibration of the model

As indicated in sensitivity analysis, a factor of safety of a soil column is dominated by the stability parameters (c', ø, z, θ). These parameters change spatially in the area, but during rainfall, they are stationary. In other words, if a soil column has a lower safety factor than another soil column before the event rainfall, the same situation is expected to be after rainfall provided that hydraulic parameters of soil columns corresponding to infiltration are not significantly different than each other. For reasonable input parameters, pixels with a lower factor of safeties before the event rainfall should be located in inventory polygons. In other words, when two stability parameter sets are compared, parameters representing the study area better, should result in the higher area under the curve in before-event rainfall conditions. And ROC curve of the parameter set should not change significantly with rainfall. This

hypothesis was tested with different parameter assemblies. When ROC curves are compared before and after TRIGRS analysis, approximately the same ROC curves are observed.

The similarity of ROC curves before and after event rainfall is taken advantage of for calibration of both stability and hydraulic parameters. The calibration of stability parameters is conducted in the before-rainfall condition considering the AUC of the model. Then, hydraulic parameters are calibrated with the rainfall evaluating the accuracy (ACC) of the model. The followed methodology is explained below.

(i)   108 hillslope failures (430 pixels) suitable for infinite slope assumption (Type 1 failures) and 15000 random pixels outside the inventory polygons were selected for the calibration. Since 15000 random pixels are considered stable, these points were sampled from outside of the 10 m buffer zone of landslide polygons.

(ii)   Three different geological units exist in the study area. Two units were considered since one of these geological units covers a tiny space. The parameter range utilized for calibration is shown in Table 4.4. Additional to stability parameters, antecedent recharge was also taken into account to evaluate the water table depth before the event rainfall. In Table 4.4, the root cohesion range was determined based on the related literature (Bathurst et al., 2010; Hürlimann et al., 2022; Wu & Sidle, 1995).

(iii)   A MATLAB code was generated to couple all combinations of parameters and automatically calculate each pixel's safety factor. Moreover, for each parameter, assembly ROC curve is constructed using different FS thresholds. Also, AUC, unstable areas (Initially positive rate), the TPR in the saturated condition, and the TPR of the model corresponding to maximum accuracy points were calculated.

(iv)   Higher AUC indicates that pixels with smaller FS favor inventory polygons. Therefore, a better parameter set is expected to have a higher AUC. Besides, for an adequate parameter group for a physically-based model, ACC should be high when FS=1.0 is selected as a cut-off value. Nevertheless, the pore pressure stage at failure

is unknown. Therefore, it is not possible to calculate accuracy directly in MATLAB. Accordingly, an indirect approach is developed to eliminate unrealistic parameter couples. Maximum TPR considering FS=1 can be achieved when all soils within the area are saturated. As indicated in Figure 4.16, if TPR at saturated condition is lower than TPR of maximum accuracy point (with different FS threshold) of ROC curve, maximum accuracy can not be obtained by calibrating hydraulic parameters. For that reason, parameter sets ending up with these consequences were eliminated. By doing that, parameter groups with unreasonably high stability are sifted.

(v)   The Second criterion was applied by considering initially-unstable areas (unstable areas after MATLAB computation). Initially-unstable areas (initial positive rates, IPR) should be less for suitable parameters. On the other hand, initially unstable areas might be steep rock surface, steep slopes remaining stable with initial suction, or stabilized slopes with retaining structures. Therefore there is no strict threshold for this criterion. Parameter sets with more than 2 percent IPR were eliminated in this study, considering the whole dataset.
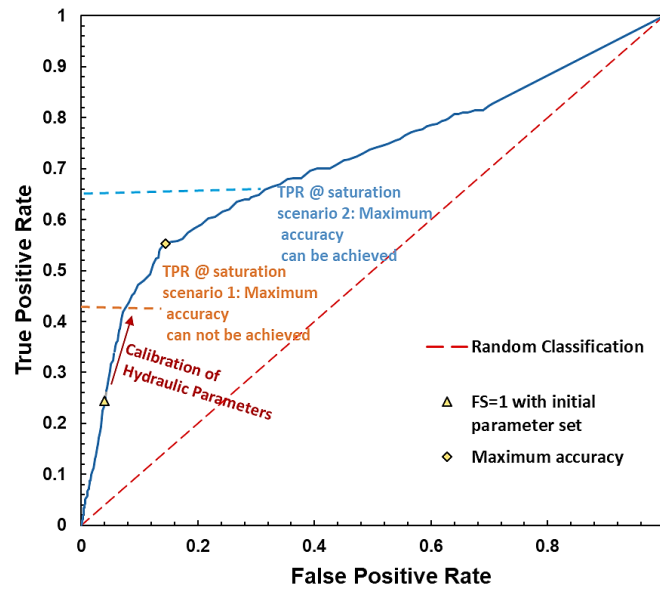
Figure 4.16. Use of ROC curve for calibration of hydraulic parameters.

(vi)   After determining suitable stability parameters (Table 4.5) hydraulic parameters were calibrated iteratively If the maximum accuracy cannot be approached sufficiently by changing the hydraulic parameters, the calibration can be continued with another stability parameter group The calibrated hydraulic parameters are shown in Table 4.6.

The advantage of this calibration procedure is to be time-saving since stability and hydraulic parameters are calibrated separately. For example, a combination of all parameter values listed in Table 4.4 was tested in 3 hours, approximately equal to one TRIGRS run with the same computer. The calibration without separating stability and hydraulic parameters might be more accurate, but it needs high computational power and more time (Zieher et al., 2017).

Table 4.4 Parameter range and increment used in calibration. (minimum:increment:maximum)

	Soil Cohesion, Cs (kPa)	Friction Angle, ø (degree)	Root Cohesion, Cr (kPa)	Antecedent Recharge Coefficient qa/ks	Soil depth, Z (m)
Kackar Granitoid	0:2:8	30:2:38			
Kızılkaya-Çatak Formation	0:2:8	30:2:38		0.00:0.001:0.01 and 0.01:0.01:0.24	1.5:0.1:2.0
Forest	-	-	0:2:10		
Tea Plantation	-	-	0		

Table 4.5 Calibrated stability parameters.

	Soil Cohesion, Cs (kPa)	Friction Angle, ø (degree)	Root Cohesion, Cr (kPa)	Soil depth, Z (m)
Kackar Granitoid (kg)	4	30		1.5
Kızılkaya-Çatak Formation (kk-kç)	4	32		1.5
Forest	*	*	10	1.5
Tea Plantation	*	*	0	1.5
Artificial Surface	*	*	0	1.5

* Respective soil parameters are used.

Table 4.6 Calibrated hydraulic parameters.

	TRIGRS			FSLAM	
Geology	α (1/m)	Ɵs-Ɵr	Ks	n*	CN
kg	0.7	0.2	10^{-6}	0.045	-
kk-kç	0.7	0.2	10^{-6}	0.045	-
Forest	-	-	-	-	73
Tea Plantation	-	-	-	-	76
Articifial Surface					96

4.2.2.1 Effect of lateral flow

It is observed that incorporating antecedent recharge increases the AUC. In the case of stability parameters in table 3 are used the change of AUC, IPR, and TPR with antecedent recharge is shown in Figure 4.17. Although incorporating antecedent recharge into the model improves the performance, initially unstable areas also increase. This trend may be because lateral flow during precipitation also contributes to failures (Montgomery and Dietrich, 1994; Park et al. 1998, Lanni et al., 2012).
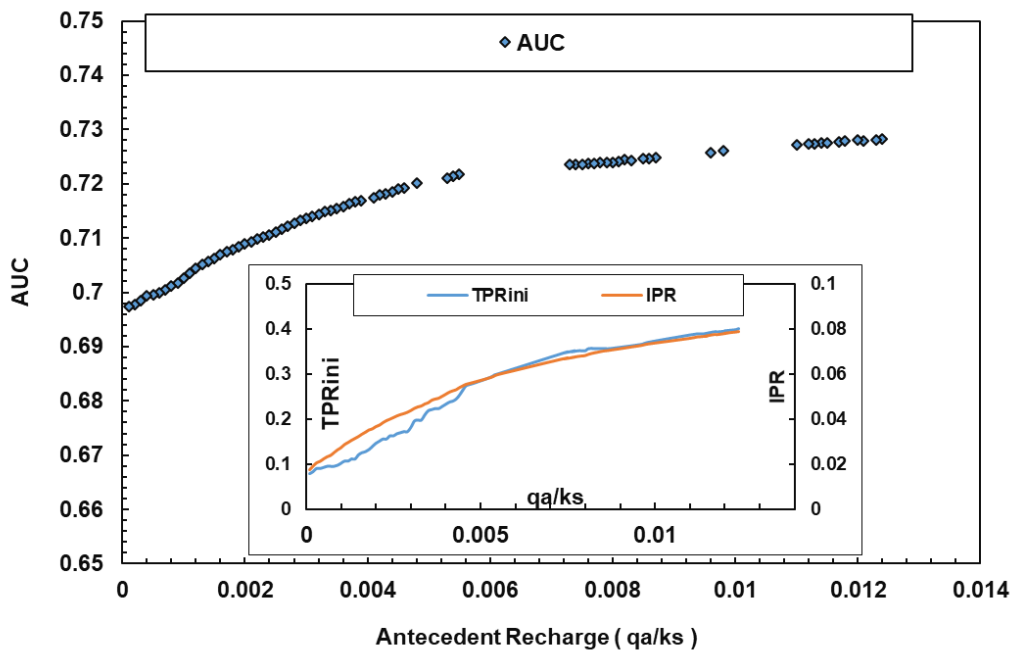
Figure 4.17. Contribution of lateral flow to model performance.

4.3 Comparison of different hydrological models

As default, TRIGRS does not compute the lateral flow effect of antecedent rainfall. Therefore, it needs the water table depth measurement. Different assumptions are adopted in the literature to estimate initial water table depth when it is unknown (Grelle et al., 2014; Salciarini et al., 2007). The most widely employed assumption is the water table coinciding with model boundary (Baum et al., 2010; Marin &

Mattos, 2020; Park et al., 2013). When we apply this assumption to TRIGRS, TPR is calculated as 0.29 (Figure 4.18).

As stated in the previous section, incorporating antecedent recharge into the models enhances the model performance, increasing initially unstable areas. On the other hand, determining steady-state recharge is complicated. It depends on water retention properties of soil, antecedent rainfall, vegetation, evapotranspiration, contributing area of slope (Iverson, 2000; Park et al., 2013). Therefore, antecedent recharge is determined by considering initially unstable areas and the resulting model performance. When steady-state recharge is applied as 0.001Ks to create the initial condition of the TRIGRS with the same approach with FSLAM, TPR rise up to 0.45 (Figure 4.18) whereas initially unstable areas increase from 2% to 3%; therefore, this amount is selected as antecedent recharge in TRIGRS and FSLAM. This amount corresponds to one-fourth of the average rainfall for two weeks before the landslides. The ROC curves and the points that correspond to FS=1.0 points are shown in Figure 4.18. In addition to FSLAM and TRIGRS, saturated conditions are also considered.
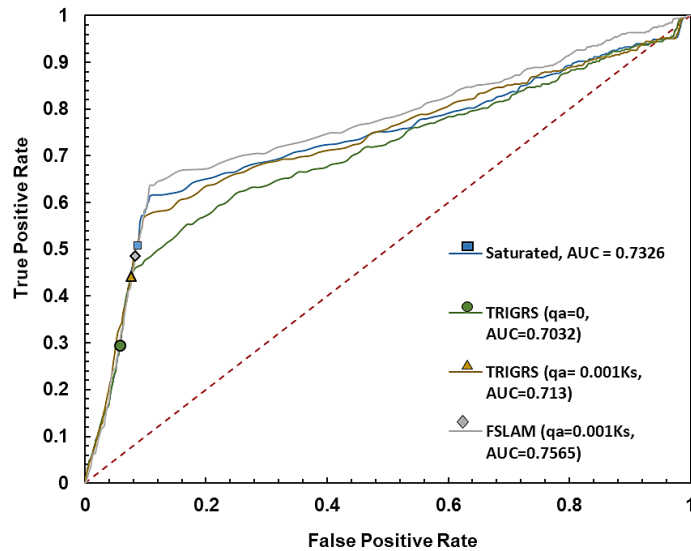
Figure 4.18. ROC plot of TRIGRS and FSLAM and saturated condition after calibration (Only Type 1 failures are considered in ROC analysis). Points represent FS=1.0.

According to the results, the highest AUC is obtained by the FSLAM model. However, the TPR of FSLAM and saturated conditions is very close to (0.49 and 0.51). Unstable areas are underestimated by TRIGRS models comparing the others (Figure 4.19). It is worth noting that the calibration of TRIGRS is based on the physical properties obtained by laboratory tests. The SWRC parameters are kept in the range of available data. Other studies also report underestimation of unstable areas with the TRIGRS-unsaturated model (Schilirò et al., 2016; Zizioli et al., 2013). On the other hand, n^* terms in the FSLAM corresponds to the fillable mean unit volume before the rainfall do not have any physical constraints. The calibrated value of n* of 0.045 indicates two possibilities. The first possibility is that the water content of the soil is high before the rain. The second possibility is that even if the water content of the soil is not high, the rainwater fills less volume through cracks in the grounds, and the pore pressure in the failure plane increases (Bordoni et al., 2015, 2021). The final perched water table conditions are shown in Figure 4.20. The final condition of FSLAM is close to saturation correspondingly cumulative distribution of the factor of safety of the saturated state, and FSLAM is close (Figure 4.22b).

It is worth noting that forest areas are stable in all cases. There are some failures in forest areas, but compared with the tea plantation area, it is significantly less (Figure 4.14). Therefore, root cohesion calculated for forest area is high. The model performance might be improved by figuring out why some forest areas fail while others do not. The difference might result from different species of trees or trunk density or changes in soil thickness etc. These questions are left to future studies because they need additional data.

80
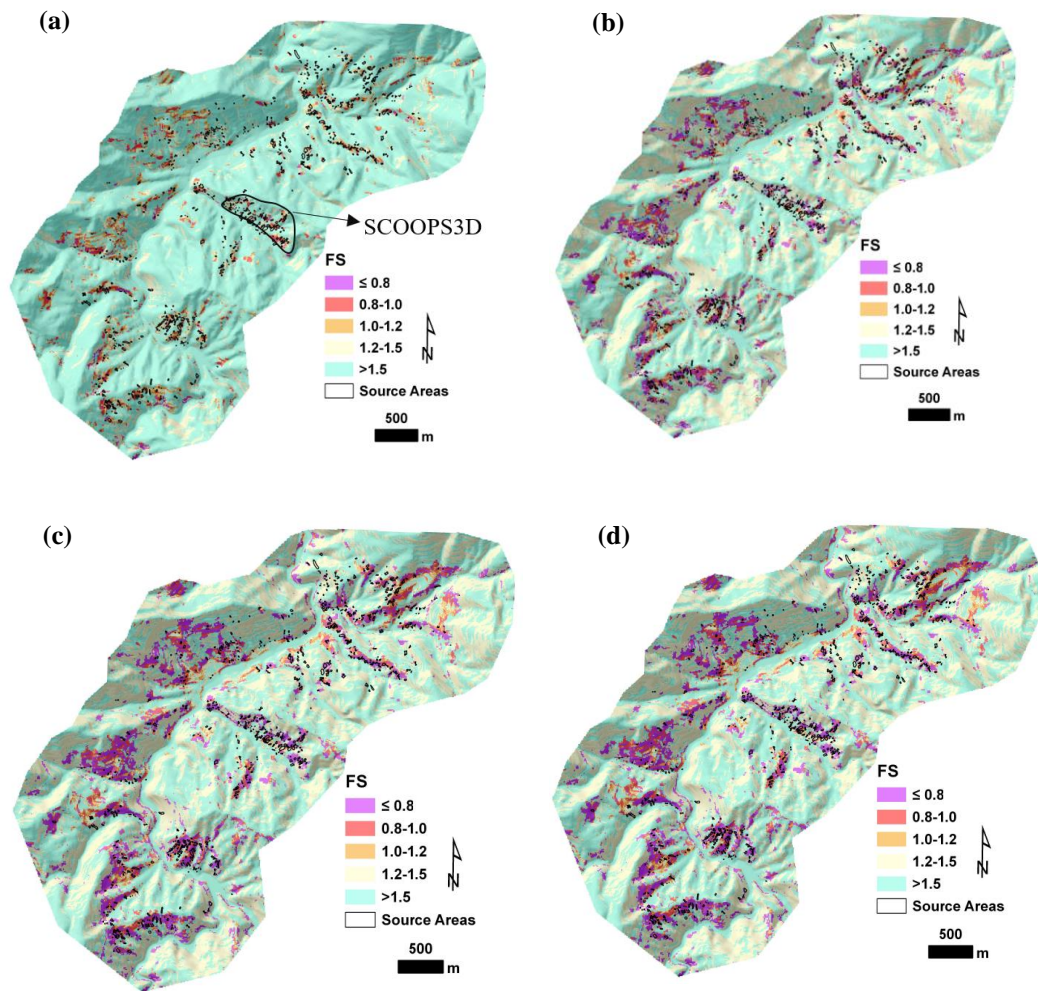
Figure 4.19. Factor of safety map after scenarios (a) Inital Condition, (b) TRIGRS, (c) FSLAM, (d) Saturated condition.
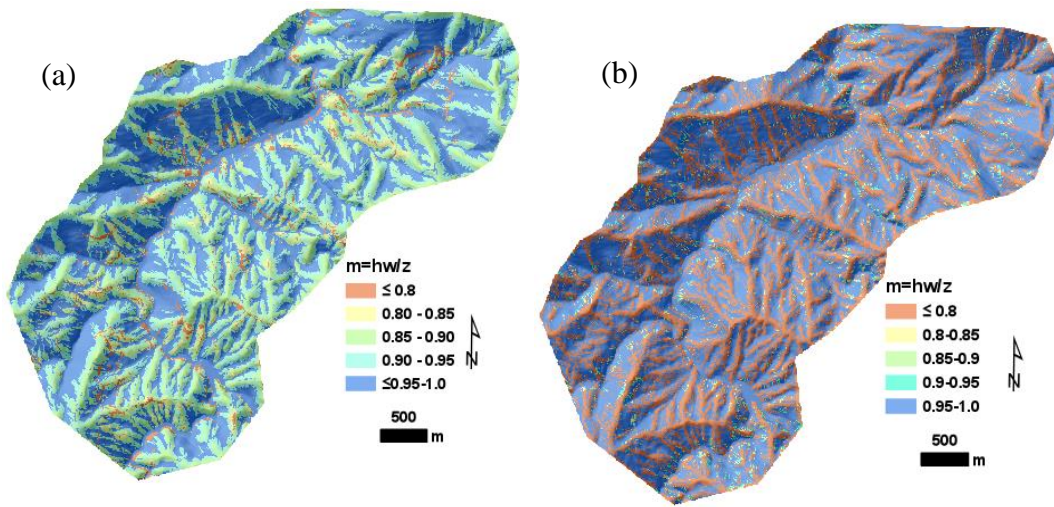
Figure 4.20. Comparison of water table height (m=hw/z) computed by TRIGRS and FSLAM. (a) FSLAM (b) TRIGRS

Considering the different failure types, the highest TPR in all hydrological conditions was observed in Type 2 failures, which is logical because these slopes are natural hillslopes that; analyzing these failures with an infinite slope equation is expected to give lower FS. As discussed earlier, Type 3 (cut slopes) and Type 4 (small failures) are not compatible with these models. As expected, TPR is less than other types; however, these failures were also recognized by the models with close accuracy with Type 1.
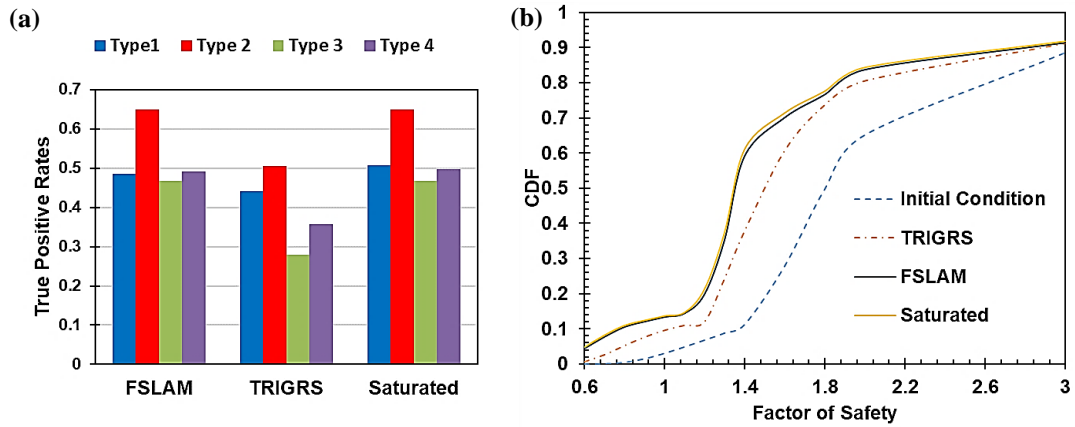
Figure 4.21. (a) True Positive Rates in different types of failures and different initial conditions. Type1: hillslope-infinite, Type2: hillslope-not-infinite, Type3: cutslopes, Type4: smaller (<10 m) slopes. (b) Cumulative distribution of factors of safety in different hydrological scenarios.

4.4   Comparison of infinite slope and SCOOPS3D solutions

SCOOP3D analysis was performed in a small part of the study area to compare with the infinite-slope solution (Figure 4.19a). A small portion of the study area is selected because of the high computational time of the SCOOPS3D. First of all, DEM is resampled to 1 m resolution for SCOOPS3D analysis since it affects the model's performance. To get a reasonable accuracy from SCOOPS3D, at least 200 cells are recommended by Reid et al. (2015) to be included in the failure surface. As stated before, the reliable resolution for available DEM data is 10 m. Therefore smallest landslides area considered in performance analysis is more than 100 m^2. Therefore, considering both the smallest landslide area and computation time, 1 m resolution is selected.

One meter resolution is employed in FSLAM and TRIGRS to be consistent in the comparison. However, since lateral flow accumulation is affected by DEM resolution, the initial water table computed for the whole study area resampled to 1

m resolution. In other words, initial conditions were kept the same with the entire study area. The pore pressure conditions in SCOOPS3D were created by considering water table depth respective to pore pressures on the failure planes in TRIGRS (Figure 4.22b) and FSLAM (Figure 4.22d) and saturated condition (Figure 4.22f). Unsaturated soil strength is ignored in SCOOPS3D for practical purposes. Because of the computational capacity limit of the used computers, SCOOPS3D analysis was conducted on 18 smaller areas. In all areas, a larger search lattice is used than DEM. Afterwards, smaller areas are merged by considering the lowest calculated factor of safety.

Comparison of factor safety maps derived from infinite slope assumption (TRIGRS and FSLAM) and SCOOP3D is shown in figure Figure 4.22.
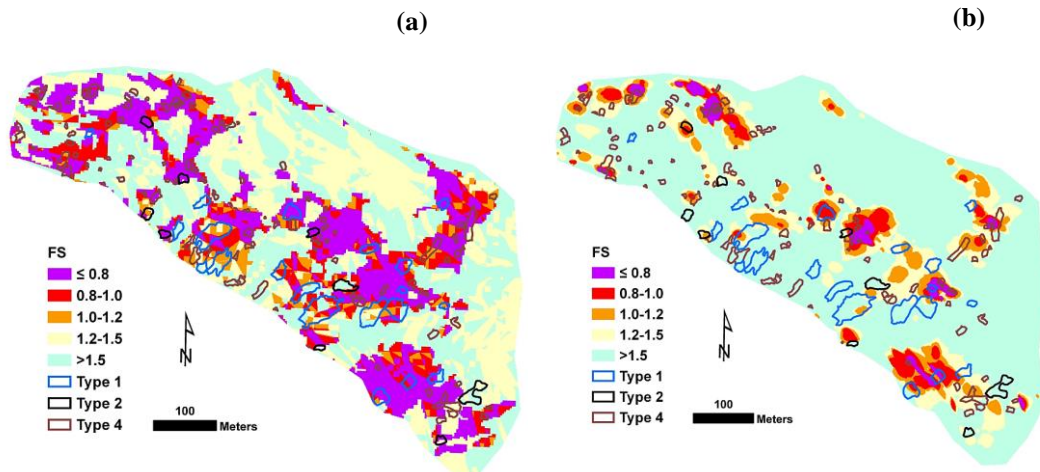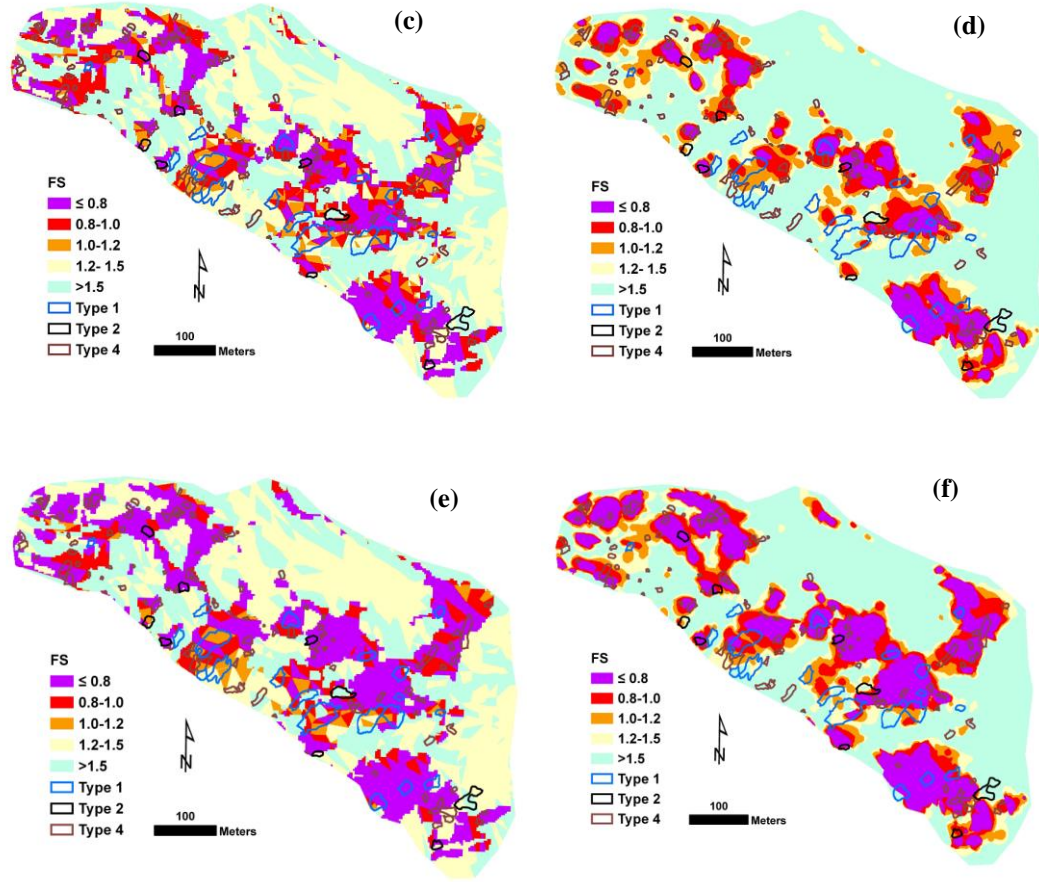
Figure 4.22. Comparison of infinite slope and SCOOPS3D factor of safety maps. **(a), (c),** and **(e)** are infinite slope, **(b), (d), (f)** are SCOOPS3D solutions. The hydrological conditions are TRIGRS, FSLAM, and saturated conditions in (a-b), (c-d), and (e-f), respectively.

Similar to the whole area difference between the infinite slope solution of FSLAM, TRIGRS, and differences for saturated conditions are not dramatic. However, SCOOP3D solution with water table depth derived by TRIGRS significantly underestimated the unstable areas. This difference might result from the fact that stable cells due to lower water table height on failure surface increase the stability of whole failure surface in SCOOPS3D, but in TRIGRS, the cells are independent of each other. This result indicates that FSLAM better represents the actual pore pressure state.

Although the TPR of the SCOOPS3D is lower than infinite slope solutions, FPR also lower. Since the model parameters are calibrated using infinite slope models, cut-off dependent comparison metrics (TPR, Accuracy, etc.) might be misleading. Therefore, TPR/FPR ratio, which is also employed in literature (Chae et al., 2015; Oguz et al., 2021), is also adopted to compare the overall performance of the infinite slope SCOOPS3D solution. TPR/FPR ratio of 3D solution of FSLAM and TRIGRS is greater than 1D (infinite slope) solution, whereas, in the saturated condition, they are almost the same (Table 4.7). These results are consistent with studies performed by (He et al., 2021; Tran et al., 2018).

Table 4.7 Comparison of global performance of infinite slope and SCOOPS3D solution.

	TRIGRS		FSLAM		Saturated	
	1D	3D	1D	3D	1D	3D
TPR	0.465	0.116	0.494	0.367	0.550	0.520
FPR	0.295	0.064	0.312	0.212	0.343	0.327
TPR/FPR	1.58	1.82	1.58	1.74	1.60	1.59

Considering failure classes, the performance of the 1D solution is less in type 2 failures which is inverse of the global trend. In contrast, the 3D solution of scenarios FSLAM and saturated conditions better results in "type 2" failures, which is a significant result because it indicates that the morphology of landslides affects the performance of stability assumptions. The physical explanation of these results is that the rotational failure assumption of SCOOPS3D become unconservative in wide and long failures compared with their depth. Because in these failures, the actual failure surface is planar instead of circular. The SCOOPS3D draws an inner tangent sphere to the failure surface since the depth is limited. One other possibility is these

large failures might be deeper than the soil depth used in the analysis. The shallower failures than 1.5 m (Type1*) were also examined to eliminate this possibility. In this case, also SCOOPS3D has a higher TPR in Type 2 than Type 1 (Figure 4.23). In both stability assumptions, smaller landlsides (Type 4) are better predicted than others, indicating that small landslides are collected in unstable areas.
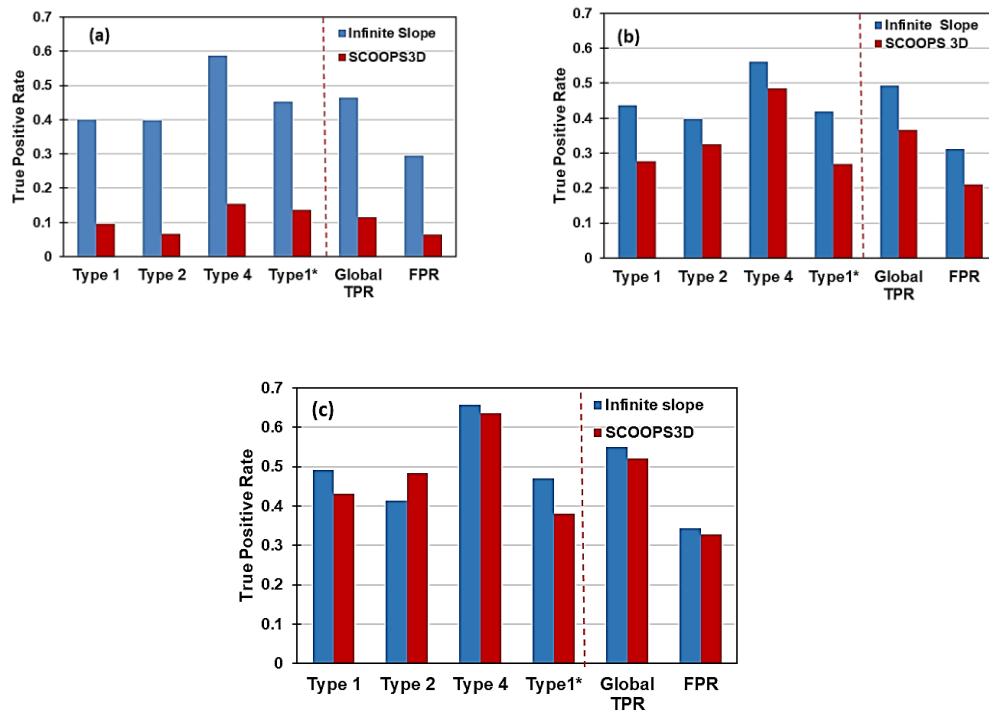
Figure 4.23. Comparison of infinite slope and SCOOPS3D solutions regarding different types of failures **(a)** TRIGRS **(b)** FSLAM **(c)** Saturated condition

CHAPTER 5

CONCLUSIONS AND RECOMMENDATIONS FOR FUTURE STUDIES

5.1 Conclusion

This study investigated landslide episodes in multiple aspects between September 27 to September 29, 2017, in Kaptanpaşa, Rize. The first aspect is obtaining morphometric features of these failures and discussing the importance of these features. The second part is physically-based modeling of this landslide event with different hydrological and stability assumptions considering the aspects discussed former part. Therefore, the results are presented below in two parts.

5.1.1 Landslide inventory

- This study discusses a suitable depth measurement method on three different methods. It is shown that using scarp height as landslide depth overestimates the depth of slip surface. A depth calculation method proposed in the literature (Washington Protocol, OWP) was modified to estimate the actual depth correctly. The depths derived by original protocol (OWP), modified protocol (MWP), and cross-section method (X-section) are 2.08 m, 0.99 m, and 1.05 m. As it can be seen, the depths derived by X-section and MWP methods are close to each other.

- The mean value of depth, length, and width of the landslides are calculated as 1.05 m, 14.3 m, and 8.5 m, respectively.

- The observed failures are classified according to their morphology and the slope types. This discrimination is essential for the validity of the assumptions in physically-based models. Most physically-based models are based on the infinite slope assumption and are suitable for natural slopes. In

89

this study, the failures are classified according to their compatibility with the infinite slope assumption.

- It is concluded that 45.0 % of the failures on hillslopes, whereas 24.2 % of failures on other slopes are suitable for modeling with infinite slope assumption. These results also justify that differentiating different slope types is vital for adequate performance assessment of the physically-based models.

- Statistical distribution of failure depth is adequately represented by Weibull distribution.

- This study discusses the overall relation between DEM cell size in the physically-based models and landslide sizes. In the landslide episode, most failures are smaller than grid sizes, which is one weakness of this study.

- Two methods are used to calculate the volume of the landslides. Prismatic assumption gave 1.23 times higher volume than half ellipsoid method. It is believed that the half ellipsoid method is more compatible with the shape of failure surfaces observed in the field.

- Landslides' size-frequency distribution is evaluated, the first study that reports these features in Rize province.

5.1.2 Physically-based modeling of landslides

- In this study, 2 different hydrological and mechanical models are compared to predict these landslides considering different failure types in terms of morphology and slope types that failure occurred.

- Strong influences of stability parameters on the resulting safety factor are stressed in the sensitivity analysis, and a simple two-stage calibration method is proposed. The calibration of models like TRIGRS is time-consuming and needs high computational power. The proposed calibration approach is expected to be functional for the areas hydraulic behavior does not dramatically change.

- Thousands of different combinations of stability parameters and antecedent recharge (to create an initial water table) combinations are examined. It is observed that incorporation of lateral flow into the model improves the model performance, but initially unstable areas also increase. Therefore, as antecedent recharge, 0.1% of hydraulic conductivity in the lateral direction is adequate to create initial conditions considering models performances and initially unstable areas.

- Comparing the hydrological model, FSLAM ended up with the best results in terms of AUC. But the results show that the pore pressure state is close to saturation during landslides.

- Since the FSLAM model is more flexible than TRIGRS, it resulted in better performance. Additionally, the curve number approach also contributed to the performance of FSLAM. However, since any constraint did not limit calibration parameter n*, whether calibrated n* is valid for future events should be tested. The model parameters are calibrated considering infinite slope models because it is not practical to perform it with SCOOPS3D.

- Only type 1 failures are employed during the calibration since they are compatible with the model's assumption and available resolution. The final True positive rate of TRIGRS, FSLAM, and saturated hydrostatic conditions are 0.45, 0.49, and 0.51.

- In the whole area, the infinite slope model gave the best performance for predicting type 2 failures. It is reasonable because the infinite slope assumption is conservative for these failures. Type 3 and type 4 failures were predicted with close TPR to type 1 except for TRIGRS. Type 4 failures are small failures compared with DEM resolution. Their high TPR indicates that these failures are located in unstable ares. In the study area, there are small landslides that are very close to each other. The model seems to give a conservative result in these parts. Using a DEM of higher resolution, susceptibility zonation might be more accurate in these parts.

- In all cases, SCOOPS3D yielded less unstable areas. The difference between infinite-slope and SCOOPS3D solutions is more in pore pressure conditions calculated by TRIGRS. But in all states except for the saturated case, TPR/FPR of SCOOPS3D is higher than the infinite slope solution; they are equal when soil is saturated. This index is similar to the LR class index, and the results are compatible with other studies in the literature.

- Within the smaller area selected for comparison, infinite-slope and SCOOPS3D solutions have an inverse trend indicating that landslide morphology affects the performance of stability assumption. SCOOPS3D is less successful in calculating the unstable areas of wide and long failures. This study is the first attempt to consider landslide morphology in comparing the SCOOPS3D and infinite-slope models.

5.2   Recommendation for future studies

- In this study, landslides' depths under forest cover could not be calculated in most failure spots. A LIDAR is needed to investigate landslide depth in the forest.

- The effect of land cover on size distribution can be explored in the future.

- With higher resolution DEM these failures can be modeled better. The influence of cell size might be examined.

- The forest areas are evaluated as stable in all cases. But it is known that there are failures. This error arose from the poor classification of LULC. Root cohesion provided by trees changes according to trunk density and the kind of the trees. The change in forest cover can be studied with additional data.

- Stratification of soil, change of soil thickness, seasonal change of soil behavior in the region might be explored with further site investigation to assess susceptibility more accurately.

- If the factors affecting the landslide morphology (topography, soil thickness, etc.) are evaluated, the variation of the stability through the landscape can be calculated more accurate.

REFERENCES

Akgun, A., Dag, S., & Bulut, F. (2008). Landslide susceptibility mapping for a landslide-prone area (Findikli, NE of Turkey) by likelihood-frequency ratio and weighted linear combination models. *Environmental Geology*, *54*(6), 1127–1143. https://doi.org/10.1007/s00254-007-0882-8

Alan, I., Balcı, V., Keskin, H., Altun, I., Böke, N., Demirbag, H., Arman, S., Elibol, H., Soyakil, M., Kop, A., & Hanilçi, N. (2019). Bulletin of the Mineral Research and Exploration Notes To the Authors. *Bulletin of the Mineral Research and Exploration*, *158*, 1–29. https://doi.org/10.19076/mta.19369

Alvioli, M., Milillo, M., Rossi, M., Palazzi, E., Hardenberg, J. V., Brunetti, M. T., & Peruccacci, S. (2018). Implications of climate change on landslide hazard in Central Italy. *Science of the Total Environment*, *630*, 1528–1543. https://doi.org/10.1016/j.scitotenv.2018.02.315

Alvioli, M., & Baum, R. L. (2016). Parallelization of the TRIGRS model for rainfall-induced landslides using the message passing interface. *Environmental Modelling and Software*, *81*, 122–135. https://doi.org/10.1016/j.envsoft.2016.04.002

Alvioli, Massimilano, Guzzetti, F., & Rossi, M. (2014). Geomorphology Scaling properties of rainfall induced landslides predicted by a physically based model. *Geomorphology*, *213*, 38–47. https://doi.org/10.1016/j.geomorph.2013.12.039

An, H., Viet, T. T., Lee, G., Kim, Y., Kim, M., Noh, S., & Noh, J. (2016). Development of time-variant landslide-prediction software considering three-dimensional subsurface unsaturated flow. *Environmental Modelling and Software*, *85*, 172–183. https://doi.org/10.1016/j.envsoft.2016.08.009

Ardizzone, F., Cardinali, M., Carrara, A., Guzzetti, F., & Reichenbach, P. (2002). Impact of mapping errors on the reliability of landslide hazard maps. *Natural Hazards and Earth System Sciences*, *2*(1–2), 3–14. https://doi.org/10.5194/nhess-2-3-2002

Bathurst, J. C., Bavolo, I. C., & Cisneros, F. (2010). Modeling the effect of forest cover on shallow landslides at river basin scale. *Ecological Engineering*, *36*, 317–327.

Baum, R. L., Coe, J. A., Godt, J. W., Harp, E. L., Reid, M. E., Savage, W. Z., Schulz, W. H., Brien, D. L., Chleborad, A. F., McKenna, J. P., & Michael, J. A. (2005). Regional landslide-hazard assessment for Seattle, Washington, USA. *Landslides*, *2*(4), 266–279. https://doi.org/10.1007/s10346-005-0023-y

Baum, R. L., Galloway, D. L., & Harp, E. L. (2008). Landslide and Land Subsidence Hazards to Pipelines. In *USCS, Open-File Report 2008-1164* (Issue 1164). internal-pdf://69.19.121.70/OF08-1164_508.pdf

Baum, R. L., Godt, J. W., & Savage, W. Z. (2010). Estimating the timing and location of shallow rainfall-induced landslides using a model for transient, unsaturated infiltration. *Journal of Geophysical Research: Earth Surface*, *115*(3). https://doi.org/10.1029/2009JF001321

Baum, R. L., Savage, W. Z., & Godt, J. W. (2008). TRIGRS — A Fortran Program for Transient Rainfall Infiltration and Grid-Based Regional Slope-Stability Analysis, Version 2.0. *U.S. Geological Survey Open-File Report*, *2008–1159*, 75.

Baum, R. L., Savage, W. Z., & Goth, J. W. (2002). *TRIGRS-A Fortran Program For Transient Rainfall Infiltration and Grid Based Regional Slope-Stability Analysis*.

Bellugi, D. G., Milledge, D. G., Cuffey, K. M., Dietrich, W. E., & Larsen, L. G. (2021). Controls on the size distributions of shallow landslides. *Proceedings of the National Academy of Sciences of the United States of America*, *118*(9). https://doi.org/10.1073/pnas.2021855118

Bordoni, M., Bittelli, M., Valentino, R., Vivaldi, V., & Meisina, C. (2021). Observations on soil-atmosphere interactions after long-term monitoring at two sample sites subjected to shallow landslides. *Bulletin of Engineering Geology and the Environment*, *80*(10), 7467–7491. https://doi.org/10.1007/s10064-021-02334-y

Bordoni, M., Meisina, C., Valentino, R., Lu, N., Bittelli, M., & Chersich, S. (2015). Hydrological factors affecting rainfall-induced shallow landslides: From the field monitoring to a simplified slope stability analysis. *Engineering Geology*, *193*, 19–37. https://doi.org/10.1016/j.enggeo.2015.04.006

Brien, D. L., & Reid, M. E. (2007). Modeling 3-D Slope Stability of Coastal Bluffs , Using 3-D Ground-Water Flow , Southwestern Seattle , Washington. *Scientific Investigations Report 2007-5092*, 61. http://pubs.usgs.gov/sir/5092

Burns, W. J., & Mickelson, K. A. (2016). Protocol for deep landslide susceptibility mapping. *DOGAMI Special Paper 48*, 63.

Burton, A., Arkell, T. J., & Bathurst, J. C. (1998). Field variability of landslide model parameters. *Environmental Geology*, *35*(2–3), 100–114. https://doi.org/10.1007/s002540050297

Cascini, L., Cuomo, S., & Guida, D. (2008). Typical source areas of May 1998 flow-like mass movements in the Campania region, Southern Italy. *Engineering Geology*, *96*(3–4), 107–125. https://doi.org/10.1016/j.enggeo.2007.10.003

Cascini, L., Cuomo, S., & Sala, M. Della. (2011). Spatial and temporal occurrence of rainfall-induced shallow landslides of flow type : A case of Sarno-Quindici , Italy. *Geomorphology*, *126*(1–2), 148–158. https://doi.org/10.1016/j.geomorph.2010.10.038

Catani, F., Segoni, S., & Falorni, G. (2010). An empirical geomorphology-based approach to the spatial prediction of soil thickness at catchment scale. *Water Resources Research*, *46*(5), 1–15. https://doi.org/10.1029/2008WR007450

Chae, B. G., Lee, J. H., Park, H. J., & Choi, J. (2015). A method for predicting the factor of safety of an infinite slope based on the depth ratio of the wetting front induced by rainfall infiltration. *Natural Hazards and Earth System Sciences*, *15*(8), 1835–1849. https://doi.org/10.5194/nhess-15-1835-2015

Chiba, Tatsuro; Kaneta, Shin-ichi; Suzuki, Y. (2008). Red relief image map: New visualization method for three dimensional data. *The International Archives of the Photogrammetry, Remote Sensing and Spatial Information Sciences*, *XXXVII*(B2), 1071–1076.

Çiçek, İ. (2015). *Türkiye'de günlük yağış şiddetleri ve sıklıkları*. Http://Tucaum.Ankara.Edu.Tr/Wp-Content/Uploads/Sites/280/2015/08/Tucaum8_2.Pdf.

Claessens, L., Heuvelink, G. B. M., Schoorl, J. M., & Veldkamp, A. (2005). DEM resolution effects on shallow landslide hazard and soil redistribution modelling. *Earth Surface Processes and Landforms*, *30*(4), 461–477. https://doi.org/10.1002/esp.1155

Comert, R., Avdan, U., Gorum, T., & Nefeslioglu, H. A. (2019). Mapping of shallow landslides with object-based image analysis from unmanned aerial vehicle data. *Engineering Geology*, *260*(February), 105264. https://doi.org/10.1016/j.enggeo.2019.105264

Corominas, J., van Westen, C., Frattini, P., Cascini, L., Malet, J. P., Fotopoulou, S., Catani, F., Van Den Eeckhaut, M., Mavrouli, O., Agliardi, F., Pitilakis, K., Winter, M. G., Pastor, M., Ferlisi, S., Tofani, V., Hervás, J., & Smith, J. T. (2014). Recommendations for the quantitative analysis of landslide risk. *Bulletin of Engineering Geology and the Environment*, *73*(2), 209–263. https://doi.org/10.1007/s10064-013-0538-8

Cruden, D. M., & Varnes, D. J. (1996). Landslide Types and Processes. *Special Report - National Academy of Science, Transportation Research Board*, *247*, 36–75.

Dağ, S., Akgün, A., Kaya, A., Alemdağ, S., & Bostancı, H. T. (2020). Medium scale earthflow susceptibility modelling by remote sensing and geographical information systems based multivariate statistics approach: an example from Northeastern Turkey. *Environmental Earth Sciences*, *79*(19), 1–21. https://doi.org/10.1007/s12665-020-09217-7

Dennis, T. G., Lutgens, F. K., & Tarbuck, E. J. (2011). *Earth Science*. Pearson Higher Ed.

Depina, I., Ahmet, E., & Thakur, V. (2020). Novel Bayesian framework for calibration of spatially distributed physical- based landslide prediction models . *Computers and Geotechnics*, *125*(April).

Dietrich, W. E., McKean, J., Bellugi, D., & Perron, T. (2007). The prediction of shallow landslide location and size using a multidimensional landslide analysis in a digital terrain model. *International Conference on Debris-Flow Hazards Mitigation: Mechanics, Prediction, and Assessment, Proceedings*, 319–329.

Fell, R., Corominas, J., Bonnard, C., Cascini, L., Leroi, E., & Savage, W. Z. (2008). Guidelines for landslide susceptibility, hazard and risk zoning for land use planning. *Engineering Geology*, *102*(3–4), 85–98. https://doi.org/10.1016/j.enggeo.2008.03.022

Filiz, M., Avcı, H., & Usta, P. (2011). Heyelanların Yerleşim Yerlerine Etkilerinin İncelenmesi (Rize-Gündoğdu Örneği). *E-J. New World Sci. Acad. Eng. Sci*, *6*(4), 1200–1211.

Frattini, P., Crosta, G. B., Fusi, N., & Dal Negro, P. (2004). Shallow landslides in pyroclastic soils: A distributed modelling approach for hazard assessment. *Engineering Geology*, *73*(3–4), 277–295. https://doi.org/10.1016/j.enggeo.2004.01.009

Frattini, P., Crosta, G., & Carrara, A. (2010). Techniques for evaluating the performance of landslide susceptibility models. *Engineering Geology*, *111*(1–4), 62–72. https://doi.org/10.1016/j.enggeo.2009.12.004

Fuchs, M., Torizin, J., & Kühn, F. (2014). The effect of DEM resolution on the computation of the factor of safety using an infinite slope model. In *Geomorphology* (Vol. 224, pp. 16–26). https://doi.org/10.1016/j.geomorph.2014.07.015

Gardner, W. . (1958). Some steady-state solutions of the unsaturated moisture flow equation with application to evaporation from a water table. *Soil Science*, *85*(4), 228–232.

Gedik, A., Ercan, T., Korkmaz, S., & Karatas, S. (1992). Rize-Fındıklı-Çamlıhemşin arasında (Doğu Karadeniz) yer alan magmatik kayaçların petrolojisi ve Doğu Pontridlerdeki bölgesel yayılımları. *Türkiye Jeoloji Kurumu Bülteni*, *C 35*, 15–38.

Gens, A., N., H. J., & Cavounidisf, S. (1988). *Three-dimensional analysis of slides in cohesive soils*. *1*, 1–23.

Gioia, E., Speranza, G., Ferretti, M., Godt, J. W., Baum, R. L., & Marincioni, F. (2016). Application of a process-based shallow landslide hazard model over a broad area in Central Italy. *Landslides*, *13*(5), 1197–1214. https://doi.org/10.1007/s10346-015-0670-6

Godt, J. W., Baum, R. L., Savage, W. Z., Salciarini, D., Schulz, W. H., & Harp, E. L. (2008). Transient deterministic shallow landslide modeling: Requirements for susceptibility and hazard assessments in a GIS framework. *Engineering Geology*, *102*(3–4), 214–226. https://doi.org/10.1016/j.enggeo.2008.03.019

Gorum, T. (2019). Landslide recognition and mapping in a mixed forest environment from airborne LiDAR data. *Engineering Geology*, *258*(February), 105155. https://doi.org/10.1016/j.enggeo.2019.105155

Görüm, T., & Fidan, S. (2021). Spatiotemporal variations of fatal landslides in Turkey. *Landslides*, *18*(5), 1691–1705. https://doi.org/10.1007/s10346-020-01580-7

Grelle, G., Soriano, M., Revellino, P., Guerriero, L., Anderson, M. G., Diambra, A., Fiorillo, F., Esposito, L., Diodato, N., & Guadagno, F. M. (2014). Space-time prediction of rainfall-induced shallow landslides through a combined probabilistic/deterministic approach, optimized for initial water table conditions. *Bulletin of Engineering Geology and the Environment*, *73*(3), 877–890. https://doi.org/10.1007/s10064-013-0546-8

Griffiths, D. V., & Marquez, R. M. (2007). Three-dimensional slope stability analysis by elasto-plastic finite elements. *Geotechnique*, *57*(6), 537–546. https://doi.org/10.1680/geot.2007.57.6.537

Griffiths, D. V, Huang, J., & Giorgia, F. (2011). *Numerical and analytical observations on long and infinite slopes*. *April 2010*, 569–585. https://doi.org/10.1002/nag

Guo, Z., Torra, O., Hürlimann, M., Abancó, C., & Medina, V. (2022). FSLAM: A QGIS plugin for fast regional susceptibility assessment of rainfall-induced landslides. *Environmental Modelling & Software*, *150*(February), 105354. https://doi.org/10.1016/j.envsoft.2022.105354

Guzzetti, F., Ardizzone, F., Cardinali, M., Rossi, M., & Valigi, D. (2009). Landslide volumes and landslide mobilization rates in Umbria, central Italy. *Earth and Planetary Science Letters*, *279*(3–4), 222–229. https://doi.org/10.1016/j.epsl.2009.01.005

Guzzetti, F., Mondini, A. C., Cardinali, M., Fiorucci, F., Santangelo, M., & Chang, K. T. (2012). Landslide inventory maps: New tools for an old problem. *Earth-Science Reviews*, *112*(1–2), 42–66. https://doi.org/10.1016/j.earscirev.2012.02.001

Haneberg, W. C. (2004). A rational probabilistic method for spatially distributed landslide hazard assessment. *Environmental and Engineering Geoscience*, *10*(1), 27–43. https://doi.org/10.2113/10.1.27

He, J., Qiu, H., Qu, F., Hu, S., Yang, D., Shen, Y., Zhang, Y., Sun, H., & Cao, M. (2021). Prediction of spatiotemporal stability and rainfall threshold of shallow landslides using the TRIGRS and Scoops3D models. *Catena*, *197*(October 2020), 104999. https://doi.org/10.1016/j.catena.2020.104999

Hong, Y., Adler, R. F., & Huffman, G. (2007). An experimental global prediction system for Rainfall-Triggered landslides using satellite remote sensing and geospatial datasets. *IEEE Transactions on Geoscience and Remote Sensing*, *45*(6), 1671–1680. https://doi.org/10.1109/TGRS.2006.888436

Hovland, J. H. (1977). Three Dimensional Slope Stability Analysis Method. *Journal of the Geotechnical Engineering Division*, *103*(9), 971–986.

Hungr, O., Evans, S. G., Bovis, M. J., & N., H. J. (2001). A Review of the Classification of Landslides of The Flow Type. *Environmental and Engineering Geoscience*, *7*(3), 221–238.

Hungr, O., Leroueil, S., & Picarelli, L. (2014). The Varnes classification of landslide types, an update. *Landslides*, *11*(2), 167–194. https://doi.org/10.1007/s10346-013-0436-y

Hürlimann, M., Guo, Z., Puig-Polo, C., & Medina, V. (2022). Impacts of future climate and land cover changes on landslide susceptibility: regional scale modelling in the Val d'Aran region (Pyrenees, Spain). *Landslides*, *19*(1), 99–118. https://doi.org/10.1007/s10346-021-01775-6

Hutchinson, J.N. (1988). General Report: morphological and geotechnical parameters of landslides in relation to geology and hydrogeology. In C. Bonnard (Ed.), *Fifth International Symposium on Landslides* (pp. 3–36). Balkema, A.A.

Hutchinson, John N. (1994). Some aspect of the morphological and geotechnical parameters of landslides, with examples drawn from italy and elsewhere. *Geologica Romana*, *30*, 1–15.

Iverson, R. M. (2000). Landslide triggering by rain infiltration. *Water Resources Research*, *36*(7), 1897–1910. https://doi.org/10.1029/2000WR900090

Keles, F., & Nefeslioglu, H. A. (2021). Infinite slope stability model and steady-state hydrology-based shallow landslide susceptibility evaluations: The Guneysu catchment area (Rize, Turkey). *Catena*, *200*(April 2020), 105161. https://doi.org/10.1016/j.catena.2021.105161

Kim, D., Im, S., Lee, C., & Woo, C. (2013). Modeling the contribution of trees to shallow landslide development in a steep, forested watershed. *Ecological Engineering*, *61*, 658–668. https://doi.org/10.1016/j.ecoleng.2013.05.003

Lanni, C., Borga, M., Rigon, R., & Tarolli, P. (2012). Modelling shallow landslide susceptibility by means of a subsurface flow path connectivity index and estimates of soil depth spatial distribution. *Hydrology and Earth System Sciences*, *16*(11), 3959–3971. https://doi.org/10.5194/hess-16-3959-2012

Larsen, I. J., Montgomery, D. R., & Korup, O. (2010). Landslide erosion controlled by hillslope material. *Nature Geoscience*, *3*(4), 247–251. https://doi.org/10.1038/ngeo776

Lee, K. T., & Ho, J. Y. (2009). Prediction of landslide occurrence based on slope-instability analysis and hydrological model simulation. *Journal of Hydrology*, *375*(3–4), 489–497. https://doi.org/10.1016/j.jhydrol.2009.06.053

Li, X., Lizárraga, J. J., & Buscarnera, G. (2021). Regional-scale simulation of flowslide triggering in stratified deposits. *Engineering Geology*, *292*(November 2020). https://doi.org/10.1016/j.enggeo.2021.106248

Liao, Z., Hong, Y., Kirschbaum, D., Adler, R. F., Gourley, J. J., & Wooten, R. (2011). Evaluation of TRIGRS (transient rainfall infiltration and grid-based regional slope-stability analysis)'s predictive skill for hurricane-triggered landslides: A case study in Macon County, North Carolina. *Natural Hazards*, *58*(1), 325–339. https://doi.org/10.1007/s11069-010-9670-y

Liu, C. N., & Wu, C. C. (2008). Mapping susceptibility of rainfall-triggered shallow landslides using a probabilistic approach. *Environmental Geology*, *55*(4), 907–915. https://doi.org/10.1007/s00254-007-1042-x

Lizárraga, J. J., & Buscarnera, G. (2019). Spatially distributed modeling of rainfall-induced landslides in shallow layered slopes. *Landslides*, *16*, 253–263. https://doi.org/10.1007/s10346-018-1088-8

Lizárraga, J. J., Frattini, P., Crosta, G. B., & Buscarnera, G. (2017). Regional-scale modelling of shallow landslides with different initiation mechanisms: Sliding versus liquefaction. *Engineering Geology*, *228*(June), 346–356. https://doi.org/10.1016/j.enggeo.2017.08.023

Lu, N., & Godt, J. W. (2011). Hillslope hydrology and stability. In *Hillslope Hydrology and Stability*. https://doi.org/10.1017/CBO9781139108164

Luo, J., Zhang, L., Yang, H., Wei, X., Liu, D., & Xu, J. (2021). Probabilistic model calibration of spatial variability for a physically-based landslide susceptibility model. *Georisk*, *0*(0), 1–18. https://doi.org/10.1080/17499518.2021.1988986

Ma, C. (2018). *Comparing and Evaluating Two Physically-based models: Openlisem and SCOOPS3D, For Landslide Volume Prediction* (Issue February). University of Twente.

Malamud, B. D., Turcotte, D. L., Guzzetti, F., & Reichenbach, P. (2004). Landslide inventories and their statistical properties. *Earth Surface Processes and Landforms*, *29*(6), 687–711. https://doi.org/10.1002/esp.1064

Marin, R. J., & Mattos, Á. J. (2020). Physically-based landslide susceptibility analysis using Monte Carlo simulation in a tropical mountain basin. *Georisk*, *14*(3), 192–205. https://doi.org/10.1080/17499518.2019.1633582

Medina, V., Hürlimann, M., Guo, Z., Lloret, A., & Vaunat, J. (2021). Fast physically-based model for rainfall-induced landslide susceptibility assessment at regional scale. *Catena*, *201*(June 2020). https://doi.org/10.1016/j.catena.2021.105213

Mergili, M., Marchesini, I., Rossi, M., Guzzetti, F., & Fellin, W. (2014). Spatially distributed three-dimensional slope stability modelling in a raster GIS. *Geomorphology*, *206*, 178–195. https://doi.org/10.1016/j.geomorph.2013.10.008

Milledge, D. G., Griffiths, D. V., Lane, S. N., & Warburton, J. (2012). Limits on the validity of infinite length assumptions for modelling shallow landslides. *Earth Surface Processes and Landforms*, *37*(11), 1158–1166. https://doi.org/10.1002/esp.3235

Montgomery, D. R., & Dietrich, W. E. (1994). A physically based model for the topographic control on shallow landsliding. *Water Resources Research*, *30*(4), 1153–1171. https://doi.org/10.1029/93WR02979

Montrasio, L., & Valentino, R. (2008). A model for triggering mechanisms of shallow landslides. *Natural Hazards and Earth System Science*, *8*(5), 1149–1159. https://doi.org/10.5194/nhess-8-1149-2008

Moos, C., Bebi, P., Graf, F., Mattli, J., Rickli, C., & Schwarz, M. (2016). *How does forest structure affect root reinforcement and susceptibility to shallow landslides ? 960*(January), 951–960. https://doi.org/10.1002/esp.3887

Napolitano, E., Fusco, F., Baum, R. L., Godt, J. W., & De Vita, P. (2016). Effect of antecedent-hydrological conditions on rainfall triggering of debris flows in ash-fall pyroclastic mantled slopes of Campania (southern Italy). *Landslides*, *13*(5), 967–983. https://doi.org/10.1007/s10346-015-0647-5

Nefeslioglu, H. A., Gokceoglu, C., Sonmez, H., & Gorum, T. (2011). Medium-scale hazard mapping for shallow landslide initiation: The Buyukkoy catchment area (Cayeli, Rize, Turkey). *Landslides*, *8*(4), 459–483. https://doi.org/10.1007/s10346-011-0267-7

Obuchowski, N. A., & Bullen, J. A. (2018). Receiver operating characteristic (ROC) curves: Review of methods with applications in diagnostic medicine. *Physics in Medicine and Biology*, *63*(7). https://doi.org/10.1088/1361-6560/aab4b1

Oguz, E. A., Depina, I., & Thakur, V. (2021). Effects of soil heterogeneity on susceptibility of shallow landslides. *Landslides*, *July 2021*, 67–83. https://doi.org/10.1007/s10346-021-01738-x

Oorthuis, R., Vaunat, J., Hürlimann, M., Lloret, A., Moya, J., Puig-Polo, C., & Fraccica, A. (2021). Slope orientation and vegetation effects on soil thermo-hydraulic behavior. An experimental study. *Sustainability (Switzerland)*, *13*(1), 1–13. https://doi.org/10.3390/su13010014

Pack, R. T., Tarboton, D. G., & N., G. C. (1998). The SINMAP Approach to Terrain Stability Mapping. *8th Congress of the International Association of Engineering Geology*, 8.

Palazzolo, N., Peres, D. J., Bordoni, M., Meisina, C., Creaco, E., & Cancelliere, A. (2021). Improving spatial landslide prediction with 3d slope stability analysis and genetic algorithm optimization: Application to the oltrepò pavese. *Water (Switzerland)*, *13*(6). https://doi.org/10.3390/w13060801

Park, D. W., Nikhil, N. V., & Lee, S. R. (2013). Landslide and debris flow susceptibility zonation using TRIGRS for the 2011 Seoul landslide event. *Natural Hazards and Earth System Sciences*, *13*(11), 2833–2849. https://doi.org/10.5194/nhess-13-2833-2013

Polat, P., & Sunkar, M. (2017). Rize'nin iklim özellikleri ve rize çevresinde uzun dönem sicaklik ve yağiş verilerinin trend analizleri. *Dergipark*, *27*, 1–23.

Rahardjo, H., Li, X. W., Toll, D. G., & Leong, E. C. (2001). The effect of antecedent rainfall on slope stability. *Geotechnical and Geological Engineering*, *19*(3–4), 371–399. https://doi.org/10.1023/A:1013129725263

Raia, S., Alvioli, M., Rossi, M., Baum, R. L., Godt, J. W., & Guzzetti, F. (2014). Improving predictive power of physically based rainfall-induced shallow landslide models: A probabilistic approach. *Geoscientific Model Development*, *7*(2), 495–514. https://doi.org/10.5194/gmd-7-495-2014

Reid, M. E., Christian, S. B., & Brien, D. L. (2000). Gravitational stability of three-dimensional stratovolcano edifices. *Journal of Geophysical Research E: Planets*, *105*(B3), 6043–6056.

Reid, M. E., Christian, S. B., Brien, D. L., & Henderson, S. . (2015). Scoops3D — Software to Analyze Three-Dimensional Slope Stability Throughout a Digital Landscape. *U.S. Geological Survey Techniques and Methods, Book 14*, 218.

Reis, S., Bayrak, T., Yalçın, A., Atasoy, M., Nişancı, R., & Ekercin, S. (2008). Rize Bölgesinde Yağış Heyelan İlişkisi. *Jeodezi, Jeoinformasyon ve Arazi Yönetimi Dergisi*, *2*(99), 5–9.

Salciarini, D., Godt, J. W., Savage, W. Z., Baum, R. L., & Conversini, P. (2008). Modeling landslide recurrence in Seattle, Washington, USA. *Engineering Geology*, *102*(3–4), 227–237. https://doi.org/10.1016/j.enggeo.2008.03.013

Salciarini, D., Godt, J. W., Savage, W. Z., Conversini, P., Baum, R. L., & Michael, J. A. (2006). Modeling regional initiation of rainfall-induced shallow landslides in the eastern Umbria Region of central Italy. *Landslides*, *3*(3), 181–194. https://doi.org/10.1007/s10346-006-0037-0

Salciarini, D., Jonathan, W. G., William, Z. S., Baum, R. L., & Pietro, C. (2007). Modelling the rainfall-induced development of shallow landslides in eastern Umbria, central Italy, using the TRIGRS (Transient Rainfall Infiltration and Grid-based Slope-stability) Examining Unsaturated Zone Processes and Model Complexity to Quantify Pote. *Conference: 1st North American Landslide Conference, At Vail, Colorado (USA), June*. https://www.researchgate.net/publication/258113220

Sarma, P. C., Dey, A., & Krishna, M. A. (2020). Influence of digital elevation models on the simulation of rainfall-induced landslides in hillslopes of Guawati, India. *Engineering Geology*, *268*(February), 1–13. https://doi.org/10.1016/j.enggeo.2020.105523

Saulnier, G. M., Beven, K., & Obled, C. (1997). Including spatially variable effective soil depths in TOPMODEL. *Journal of Hydrology*, *202*(1–4), 158–172. https://doi.org/10.1016/S0022-1694(97)00059-0

Schilirò, L., Montrasio, L., & Scarascia Mugnozza, G. (2016). Prediction of shallow landslide occurrence: Validation of a physically-based approach through a real case study. *Science of the Total Environment*, *569–570*, 134–144. https://doi.org/10.1016/j.scitotenv.2016.06.124

Segoni, S., Rossi, G., & Catani, F. (2012). Improving basin scale shallow landslide modelling using reliable soil thickness maps. *Natural Hazards*, *61*(1), 85–101. https://doi.org/10.1007/s11069-011-9770-3

Shao, W., Bogaard, T. A., Bakker, M., & Greco, R. (2015). Quantification of the influence of preferential flow on slope stability using a numerical modelling approach. *Hydrology and Earth System Sciences*, *19*(5), 2197–2212. https://doi.org/10.5194/hess-19-2197-2015

Simoni, S., Zinotti, F., Bertoldi, G., & Riccardo, R. (2008). Modeling of probability of occurence of landslides and channelized debris flows using GEOtop-FS. *Hydrological Processes*, *22*, 532–545. https://doi.org/10.1002/hyp

Sitarenios, P., Casini, F., Askarinejad, A., & Springman, S. (2021). Hydro-mechanical analysis of a surficial landslide triggered by artificial rainfall: The Ruedlingen field experiment. *Geotechnique*, *71*(2), 96–109. https://doi.org/10.1680/jgeot.18.P.188

Skempton, A. W., & Hutchinson, J. N. . (1969). Stability of Natural Slopes and Embankmen Foundations. *International Conference of Soil Mechanics and Foundation Engineering*, 291–340. https://doi.org/10.1007/978-3-319-73568-9_174

Slaughter, S. L., Burns, W. J., Mickelson, K. A., Jacobacci, K. E., Biel, A., & Contreras, T. A. (2017). *Protocol for Landslide Inventory Mapping From Lidar Data in Washington State*. *April*, 1–27. http://www.dnr.wa.gov/Publications/ger_b82_landslide_inventory_mapping_protocol.zip

Song, Z., Li, X., Lizárraga, J. J., Zhao, L., & Buscarnera, G. (2020). Spatially distributed landslide triggering analyses accounting for coupled infiltration and volume change. *Landlisdes*, *17*, 2811–2824. https://doi.org/10.1007/s10346-020-01451-1

Sorbino, G., Sica, C., & Cascini, L. (2010). Susceptibility analysis of shallow landslides source areas using physically based models. *Natural Hazards*, *53*(2), 313–332. https://doi.org/10.1007/s11069-009-9431-y

Srivastava, R., & Yeh, T. (1991). Analytical Solution for One-Dimensional, Transient Infiltration Toward the Water Table in Homogeneous and Layered Soils. *Water Resources Research*, *27*(5), 753–762. https://doi.org/https://doi.org/10.1029/90WR02772

Stark, C. P., & Hovius, N. (2001). The characterization of landslide size distributions. *Geophysical Research Letters*, *28*(6), 1091–1094.

Tarolli, P., & Tarboton, D. G. (2006). A new method for determination of most likely landslide initiation points and the evaluation of digital terrain model scale in terrain stability mapping. *Hydrology and Earth System Sciences*, *10*(5), 663–677. https://doi.org/10.5194/hess-10-663-2006

Tesfa, T. K., Tarboton, D. G., Chandler, D. G., & McNamara, J. P. (2009). Modeling soil depth from topographic and land cover attributes. *Water Resources Research*, *45*(10), 1–16. https://doi.org/10.1029/2008WR007474

Tiwari, R. C., Bhandary, N. P., & Yatabe, R. (2014). Spectral element analysis to evaluate the stability of long and steep slopes. *Acta Geotechnica*, *9*(5), 753–770. https://doi.org/10.1007/s11440-013-0292-x

Tran, T. V., Alvioli, M., Lee, G., & An, H. U. (2018). Three-dimensional, time-dependent modeling of rainfall-induced landslides over a digital landscape: a case study. *Landslides*, *15*(6), 1071–1084. https://doi.org/10.1007/s10346-017-0931-7

Tsai, T.-L., & Chiang, S.-J. (2013). Modeling of layered infinite slope failure triggered by rainfall. *Environmental Erath Science*, *68*, 1429–1434. https://doi.org/10.1007/s12665-012-1840-7

TSMS. (2021). *Resmi Istatistikler*. https://www.mgm.gov.tr/veridegerlendirme/il-ve-ilceler-istatistik.aspx?k=H&m=RIZE

Tuysuz, O., Genc, S. ., Tarı, U., & Erturac, M. . (2008). Geological, geographical and manmade factors controlling landslide potential of Rize province, Northern Turkey. *33rd Geological Congress*.

USDA. (1986). Urban Hydrology for Small Watersheds. In *Soil Conservation* (Issue Technical Release 55 (TR-55)). http://scholar.google.com/scholar?hl=en&btnG=Search&q=intitle:Urban+Hydrology+for+Small+watersheds#1

Uyeturk, C. E., Huvaj, N., Bayraktaroglu, H., & Huseyinpasaoglu, M. (2020). Geotechnical characteristics of residual soils in rainfall-triggered landslides in Rize, Turkey. *Engineering Geology*, *264*(June 2019), 105318. https://doi.org/10.1016/j.enggeo.2019.105318

Uyetürk, E. C. (2019). *Geotechnical Characterization of Soils Prone to Rainfall-Induced Landslides In Rize (Northern Turkey) (Masters' thesis, Middle East Technical University).*

Varnes, D. J. (1958). Landslide types and processes. *Special Report - National Academy of Science, Highway Research Board*, *28*, 20–47.

Varnes, D. J. (1978). Slope Movement Types and Processes. *Special Report - National Academy of Science, Transportation Research Board*, *176*, 11–33.

Vieira, B. C., Fernandes, N. F., Augusto Filho, O., Martins, T. D., & Montgomery, D. R. (2018). Assessing shallow landslide hazards using the TRIGRS and SHALSTAB models, Serra do Mar, Brazil. *Environmental Earth Sciences*, *77*(6), 1–15. https://doi.org/10.1007/s12665-018-7436-0

Vieira, B. C., Fernandes, N. F., & Filho, O. A. (2010). Shallow landslide prediction in the Serra do Mar, São Paulo, Brazil. *Natural Hazards and Earth System Science*, *10*(9), 1829–1837. https://doi.org/10.5194/nhess-10-1829-2010

Viet, T. T., Lee, G., Thu, T. M., & An, H. U. (2017). *Effect of Digital Elevation Model Resolution on Shallow Landslide Modeling Using TRIGRS*. *18*(2), 1–12. https://doi.org/10.1061/(ASCE)NH.1527-6996.0000233

Wei, W. B., Cheng, Y. M., & Li, L. (2009). Three-dimensional slope failure analysis by the strength reduction and limit equilibrium methods. *Computers and Geotechnics*, *36*(1–2), 70–80. https://doi.org/10.1016/j.compgeo.2008.03.003

Wu, W., & Sidle, R. C. (1995). A distributed slope stability model for steep forested basin. *Water Resources*, *31*(8), 2097–2110.

Yalcin, A. (2008). GIS-based landslide susceptibility mapping using analytical hierarchy process and bivariate statistics in Ardesen (Turkey): Comparisons of results and confirmations. *Catena*, *72*(1), 1–12. https://doi.org/10.1016/j.catena.2007.01.003

Yalcin, A., & Bulut, F. (2007). Landslide susceptibility mapping using GIS and digital photogrammetric techniques: A case study from Ardesen (NE-Turkey). *Natural Hazards*, *41*(1), 201–226. https://doi.org/10.1007/s11069-006-9030-0

Zhang, K., Cao, P., Liu, Z. Y., Hu, H. H., & Gong, D. P. (2011). Simulation analysis on three-dimensional slope failure under different conditions. *Transactions of Nonferrous Metals Society of China (English Edition)*, *21*(11), 2490–2502. https://doi.org/10.1016/S1003-6326(11)61041-8

Zieher, T., Perzl, F., Rössel, M., Rutzinger, M., Meißl, G., Markart, G., & Geitner, C. (2016). A multi-annual landslide inventory for the assessment of shallow landslide susceptibility - Two test cases in Vorarlberg, Austria. *Geomorphology*, *259*, 40–54. https://doi.org/10.1016/j.geomorph.2016.02.008

Zieher, T., Rutzinger, M., Schneider-Muntau, B., Perzl, F., Leidinger, D., Formayer, H., & Geitner, C. (2017). Sensitivity analysis and calibration of a dynamic physically based slope stability model. *Natural Hazards and Earth System Sciences*, *17*(6), 971–992. https://doi.org/10.5194/nhess-17-971-2017

Zinck, A. J., Lopez, J., Metternicht, G., Shrestha, D. P., & Selem, L. (2001). Mapping and modelling mass movements and gullies in mountainous areas using remote sensing and GIS techniques. *ITC Journal*, *3*(1), 43–53.

Zizioli, D., Meisina, C., Valentino, R., & Montrasio, L. (2013). Comparison between different approaches to modeling shallow landslide susceptibility: A case history in Oltrepo Pavese, Northern Italy. *Natural Hazards and Earth System Sciences*, *13*(3), 559–573. https://doi.org/10.5194/nhess-13-559-2013